Thermodynamic Study of Acylglycerols Solidification for Predicting Cold Flow Properties of Biodiesel

Latifa SENIORITA

This page is intentionally left blank.

Contents

List of Figures

List of Tables

List of Abbreviations

ASTM : American Society for Testing and Materials
B10 : Fossil diesel and biodiesel blend fuel with biodiesel content of 10 vol.%
CF : Compound formation
CFPP : Cold filter plugging point
CP : Cloud point
DAG18:1 : Monoacid 1,3-diacylglycerol of fatty acid with 18 carbon chain length and 1 unsaturated double bond. In this case, 1,3-diolein.
DSC : Differential scanning calorimetry
FAME : Fatty acid methyl ester
FMT : Final melting temperature
FTIR : Fourier transform infra-red spectrometry
IR : Infra-red (light spectrum)
JIS : Japanese Industrial Standards
LTFT : Low temperature filter test
MAG18:1 : 1-monoacylglycerol of fatty acid with 18 carbon chain length and 1 unsaturated double bond. In this case, 1-monoolein.
NRTL : Non-Random, Two Liquid activity coefficient model
NSS : Non-solid-solution
PP : Pour point
SLE : Solid-liquid equilibrium
SS : Solid-solution
TAG18:1 : Monoacid triacylglycerol of fatty acid with 18 carbon chain length and 1 unsaturated double bond. In this case, triolein.
UNIFAC : Universal quasi chemical functional-group activity coefficient model
UNIQUAC : Universal quasi chemical activity coefficient model
XRD : X-ray diffraction analysis

List of Symbols

ΔC : Difference in carbon chain length of monoacylglycerols

$C_{p,i}$: Heat capacity of component i at a constant pressure p

f_i : Fugacity of component i in the mixture

$\Delta H_i{}^{SL}$: Difference between the enthalpies of component i at solid and liquid states at the triple point (enthalpy of fusion)

H_i : Enthalpy of component i

$\Delta H_{m,i}$: Enthalpy of fusion of pure component i

L (superscript) : Liquid phase

R : Ideal gas constant

S (superscript) : Solid phase

T : Temperature

$T_{m,i}$: Melting point of pure component i

T_{SLE} : Solid-liquid equilibrium temperature

x_i : Mole fraction of component i in the liquid phase

z_i : Mole fraction of component i in the solid phase

γ_i : Activity coefficient of component i in the mixture

Compound formation model nomenclatures

Δh^{ref} : Reaction enthalpy for molecular compound formation at a reference condition

K_a : Reaction equilibrium constant

$K_a{}^{ref}$: Reaction equilibrium constant evaluated at a reference condition

T_{CF} : Liquidus temperature in molecular compound formation

T^{ref} : Reference temperature

v_A, v_B : Stoichiometric ratios of components A and B, respectively, in molecular compound formation

Modified UNIFAC (Dortmund) method nomenclatures

a_{nm}, b_{nm}, c_{nm} : UNIFAC group interaction parameters between groups n and m

F_i : UNIFAC surface area property of component i

q_i : Relative van der Waals surface area of component i

Q_k : Relative van der Waals surface area of group k

r_i : Relative van der Waals volume of component i

R_k : Relative van der Waals volume of group k

V_i , V'_i : UNIFAC auxiliary volume properties of component i

v_k : Number of group k in the mixture

${v_k}^{(i)}$: Number of group k in the component i

X_m : Mole fraction of group m in liquid phase

${\gamma_i}^C, {\gamma_i}^R$: UNIFAC combinatorial and residual activity coefficient of component i

Γ_k : Group activity coefficient of group k in the mixture

${\Gamma_k}^{(i)}$: Group activity coefficient of group k in the pure component i

ψ_{nm} : UNIFAC group interaction parameter between groups n and m

θ_m : Surface fraction of group m in the liquid phase

Chapter 1 Introduction

1.1 Global status of biodiesel utilization

Biodiesel and bioethanol derived from biomass resources are currently the most commercialized renewable automotive fuels in the world. These biofuels are expected to play an important role in reducing CO_2 emissions from the transportation sector, which accounted for 37% of global energy consumption in 2019 (REN21, 2020). While fossil fuels, such as gasoline and diesel fuel, still dominated the transportation sector, renewable automotive fuels shared 1.0% of total final energy consumption in 2019 (REN21, 2020). As shown in Fig. 1-1, the production of biofuels, such as bioethanol, biodiesel, and hydrogenated vegetable oils, is steadily increasing year by year and is expected to grow by about 24% from 2019 to 2024 (IEA, 2019).

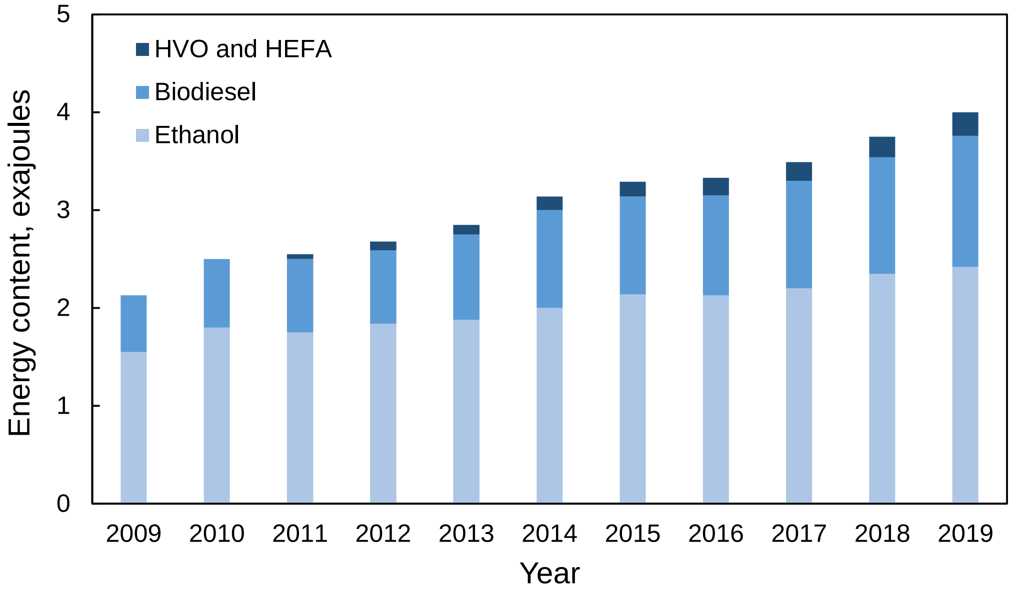

Fig. 1-1. Annual production of biofuels in the world: hydrogenated vegetable oil (HVO) and hydrogenated esters and fatty acid (HEFA), biodiesel (fatty acid methyl esters), and bioethanol (REN21, 2020).

In recent years, biodiesel accounted for about one-third of all automotive biofuels. Biodiesel is produced from plant oils, such as palm oil, soybean oil, and rapeseed oil, by transesterification with methanol or ethanol; therefore, biodiesel consists of fatty acid methyl esters (FAMEs) or fatty acid ethyl esters (FAAE). While FAME is globally commercialized, FAAE is still in the research and development stage, mainly in Latin American countries. Compared to fossil diesel, biodiesel offers various advantages: low emissions, no carcinogenic substances, non-toxic, biodegradable, high flash point, and low sulfur content (Hoekman et al., 2012). On the other hand, biodiesel has some drawbacks, as it is prone to oxidation, has poor cold flow properties, and slightly lower calorific value than fossil diesel.

Biodiesel is commonly used as an alternative to fossil diesel, and its blending ratio in fossil diesel depends on national policies; in 2017, biodiesel blends ranged from 2% (B2) to 20% (B20) around the world (REN21, 2017); in 2019, the blending ratios were updated to higher levels in many countries (REN21, 2020), but due to the drawbacks mentioned above, there are concerns about problems associated with increased blending levels. Currently, Indonesia has the highest blending level of B30, which is almost three times higher than the highest blending levels in other countries (Rahmanulloh & McDonald, 2020).

Due to the rise in mandatory blending levels, biodiesel production increased by 13% from 2018 to 2019, reaching a record level of 47.4 billion liters (REN21, 2020). Indonesia was the main contributor to this increase, nearly doubling its production capacity from 2018 to 2019, followed by Brazil with an 11% increase (REN21, 2020). With the widespread adoption of mandatory blending of biodiesel with fossil diesel, and some countries having increased blending levels in the past year, production growth is expected to be 34% over the 5 years starting in 2019 (IEA, 2019). In the coming years, to support more ambitious levels of blending, the development of cleaner and more efficient fuel production (Mahlia et al., 2020), finding solutions to mitigate the impact of biodiesel’s drawbacks (Sia et al., 2020), and assessing the economic impact and sustainability (Živković et al., 2017; Correa et al., 2019) are the focus of attention.

1.2 Fossil diesel and biodiesel

1.2.1 Chemical structure and composition

Fossil diesel is a mixture of hydrocarbons produced by distilling crude oil and then hydrodesulfurizing. The number of carbon atoms in the hydrocarbons in fossil diesel is distributed in C8 to C30, typically concentrated in C10 to C18. The chemical components of fossil diesel are classified as alkanes (saturated hydrocarbons), alkenes and alkynes (unsaturated hydrocarbons), and aromatics (hydrocarbons with aromatic rings), and some structural examples are shown in Fig. 1-2. Since each chemical group has various carbon numbers, chain lengths, and branched and cyclic structures, fossil diesel may consist of hundreds of hydrocarbons. The chemical composition of fossil diesel varies greatly depending on the origin of the crude oil.

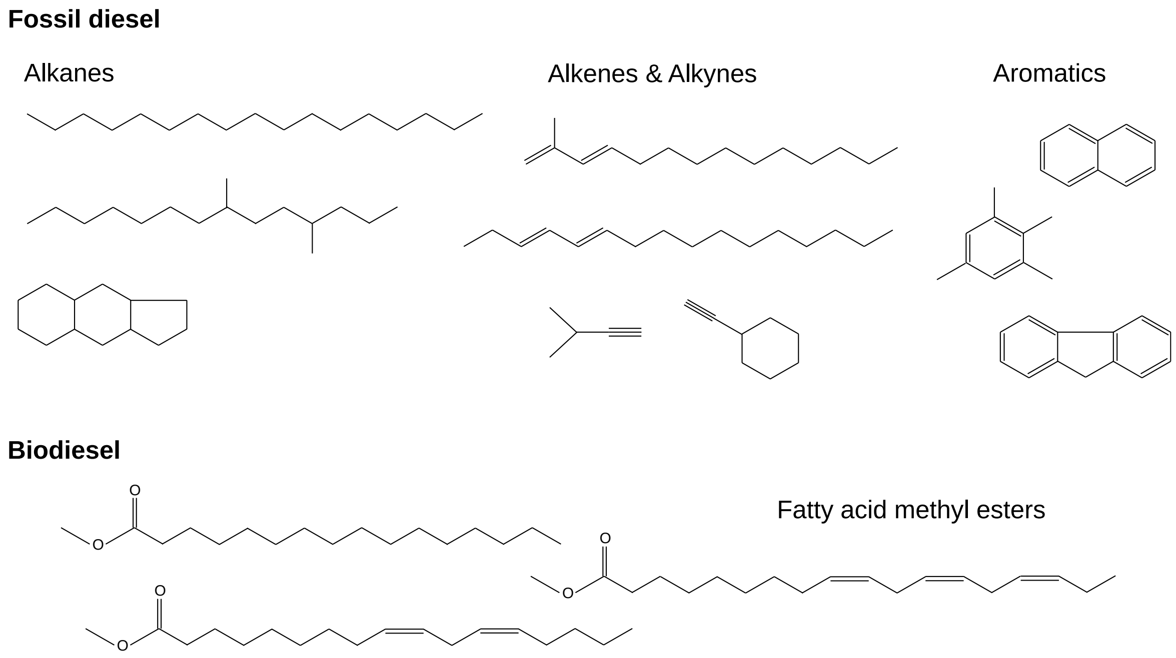

Fig. 1-2. Typical chemical groups found in fossil diesel and biodiesel fuels

On the other hand, biodiesel is a mixture of FAMEs produced by transesterification of triacylglycerol, the main component of plant oils, with methanol. Alkaline-catalyzed transesterification is widely used in the commercial production of biodiesel because the reaction proceeds quickly even under atmospheric pressure at about 60 °C with a slight excess amount of methanol, which reduces production costs. In this reaction, as shown in Fig. 1-3, one molecule of triacylglycerol is converted into diacylglycerol, monoacylglycerol, and finally, free glycerol; at each step, one molecule of FAME is produced (three molecules in total). The resulting reaction mixture is washed with water to remove catalyst, excess methanol, and by-product glycerol for purification.

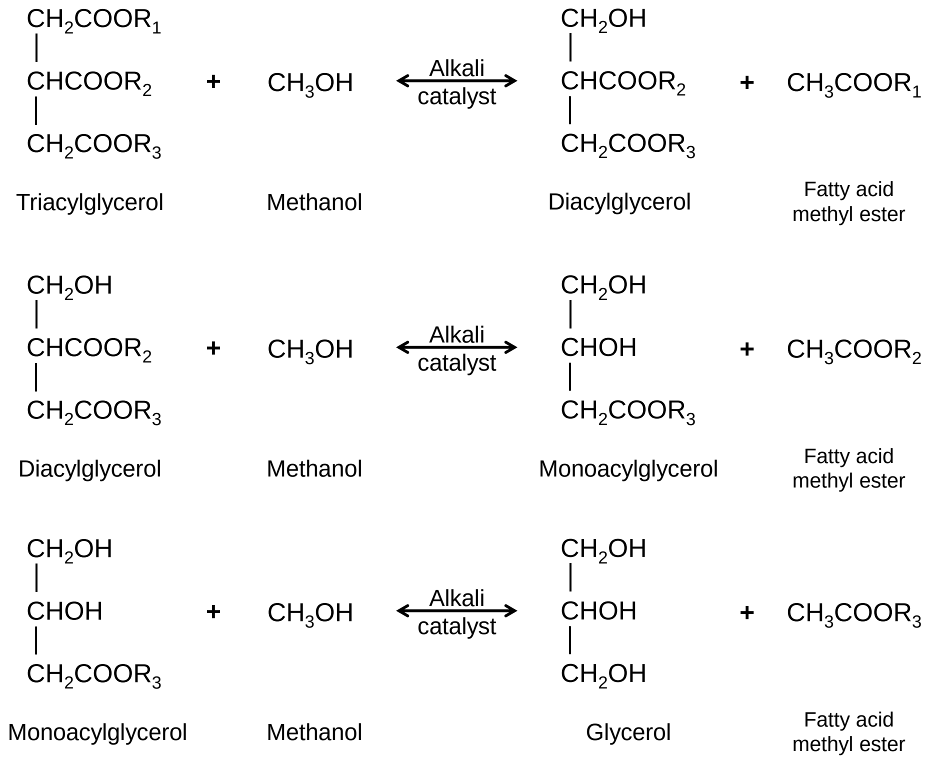

Fig. 1-3. Three-step transesterification of triacylglycerol in plant oils to produce biodiesel. R_1, R_2, and R_3 refer to alkyl chains of fatty acids.

As shown in Table 1-1, the chemical composition of biodiesel depends on the kind of plant oils used as a raw material because the fatty acid composition of plant oil is different by the kind of species. Fatty acids are abbreviated using two colon-separated numbers to show the numbers of carbon atoms and double bonds. For example, oleic acid has 18 carbons and one double bond and is expressed as C18:1. As shown in Table 1-1, palmitic (C16:0), oleic (C18:1), linoleic (C18:2), and linolenic (C18:3) acids are common in most plant oils. However, coconut oil is quite different from other plant oils because it is composed of short fatty acids, including lauric acid (C12:0).

1.2.2 Physical properties

Table 1-2 compares the physical properties of common fossil diesel and biodiesel from various feedstocks. Biodiesel fuels usually have slightly higher densities and viscosities and much higher flash points than fossil diesel. The high flash points of biodiesels are due to the relatively high boiling points of FAMEs, making them safer

Table 1-1. Fatty acid composition (wt.%) of various plant oils (Hoekman et al., 2012)

Fatty acid		Feedstock				
		Corn	Coconut	Palm	Rapeseed	Soy
Caprylic	C8:0	-	8.5	-	-	-
Capric	C10:0	-	6.1	-	-	-
Lauric	C12:0	-	47.9	-	-	-
Myristic	C14:0	-	18.5	-	-	-
Palmitic	C16:0	11.9	8.4	39.8	3.4	12.1
Palmitoleic	C16:1	-	-	0.2	-	0.3
Stearic	C18:0	2.0	1.7	5.3	1.1	3.5
Oleic	C18:1	24.9	5.7	41.9	63.3	23.4
Linoleic	C18:2	33.7	1.4	11.5	22.0	54.2
Linolenic	C18:3	-	-	0.2	8.1	6.5
Arachidic	C20:0	-	-	-	-	-
Others	-	27.6	2.0	1.2	2.1	0.1

Table 1-2. Physical properties and cold flow properties of biodiesel and fossil diesel (Canakci & Sanli, 2008; Alptekin & Canakci, 2009; Karmakar et al., 2010).

	Fossil diesel	Biodiesel			
		Corn ME	Palm ME	Rapeseed ME	Soy ME
Viscosity (mm^2/s)	2.0 ~ 4.5	4.18	5.70	4.83	4.08
Density (g/cm^3)	0.82 ~ 0.86	0.884	0.876	0.882	0.884
Cetane number	51.0	60.9	62.0	52.9	50.9
Flash point (ºC)	55	192	164	155	131
Cloud point (ºC)	-18.0	-2.8	13.0	-4.0	-0.5
Pour point (ºC)	-25.0	-1.0	-	-10.8	-10.8

against fire than fossil diesel. The physical properties of biodiesel are related to the properties of FAMEs and therefore strongly depend on the fatty acid composition of the feedstock. In general, viscosity, density, cetane number, cloud point, and pour point increase with the carbon chain length of FAME, but decrease with the degree of unsaturation of FAME. For example, biodiesel from palm oil is rich in saturated fatty acids such as palmitic acid (C16:0), as shown in Table 1-1, and has a lower degree of unsaturation, resulting in higher viscosity, cetane number, and cloud point than other biodiesel fuels.

1.2.3 Behavior at low temperatures

Cold flow properties, which indicate the flowability of liquid fuels at low temperatures, are essential for operating automobiles, especially in cold climates. Some of the most used and known cold flow properties are the cloud point and pour point, as described in detail later.

Although the physical properties of fossil diesel and biodiesel are relatively close, their cold flow properties are different. The cloud point and pour point of fossil diesel in Table 1-2 are -18.0 °C and -25.0 °C, respectively, indicating that the formation of problematic solid precipitates begins at -18 °C. This precipitation is attributed to high molecular weight alkanes of C18 or more, which have relatively high melting points among fossil diesel components (Dunn, 2009). On the other hand, the cloud points of biodiesel range from -4.0 to 13.0 °C in Table 1-2, which are much higher than that of fossil diesel, indicating that precipitation occurs even at higher temperatures. As a result, the cold flow properties may worsen when biodiesel is blended with fossil diesel, even if the blending ratio is less than 5 % (Moser, 2014).

The cold flow properties of biodiesel with few impurities depend mainly on the contents of saturated FAMEs, which have higher melting points than unsaturated ones (Moser, 2014; Imahara et al., 2006; Dunn, 2008). Improvements in the cold flow properties of biodiesel include the use of less saturated plant oils and the addition of cold flow improvers (Sierra-Cantor & Guerrero-Fajardo, 2017).

In addition to saturated FAMEs, minor components can also affect cold flow properties if their contents exceed certain limits. Methanol, water, soap, free glycerol, and acylglycerols (mono-, di-, and triacylglycerols) are minor components in the production process. Of these, methanol, water, soap, and free glycerol are mostly removed by washing with water to comply with biodiesel standards (Committee for Standardization Automotive Fuels, 2008). In addition, if the feedstock plant oil contains steryl glucosides, they may become impurities in biodiesel. Steryl glucosides have very high melting points and may affect cold flow properties (Tang et al., 2008), but these are not general impurities and rare in biodiesel.

On the other hand, acylglycerols are common impurities in biodiesel because they are reaction intermediates and cannot be removed by water rinsing. Because acylglycerols usually have high melting points than FAMEs, their effect on cold flow properties cannot be ignored. In fact, solid precipitates from soybean methyl esters consisted mainly of saturated monoacylglycerols and a small amount of diacylglycerols (Yu et al., 1998). Monoacylglycerols showed a critical influence on the filter blocking tendency (Chupka et al., 2012) and also caused significant changes in cold flow properties with increasing their contents (Dunn, 2012). These findings indicate that acylglycerols play an essential role in the solidification behavior of biodiesel.

1.3 Acylglycerols

Acylglycerols are ester compounds in which fatty acids are ester-bonded to any or all three hydroxyl groups of glycerol. Acylglycerols are called mono-, di-, and triacylglycerols, according to the number of fatty acids bound. The chemical structures of acylglycerols are shown in Fig. 1-4, showing examples that bond to palmitic acids.

Monoacylglycerols (MAGs) have a single fatty acid bound to the glycerol backbone and are named, for example, 1-monopalmitoylglycerol (1-monopalmitin), indicating the binding position and type of fatty acid. Diacylglycerols (DAGs) and triacylglycerols (TAGs) have two and three fatty acids, respectively, and different types of fatty acids are possible to be bound. For example, 1-palmitoyl-3-oleoylglycerol is often abbreviated as P(OH)O because palmitin (P), hydroxyl group (OH), and olein (O) are bound to glycerol in this order. Similarly, 1,3-dipalmitoyl-2-oleoylglycerol, an example of triacylglycerols (TAGs), is abbreviated as POP. Since this study covers only acylglycerols of one type of fatty acid (monoacid), acylglycerols were abbreviated based on the one fatty acid bound. For example, 1,3-dipalmitoylglycerol and tristearoylglycerol were abbreviated as DAG16:0 and TAG18:0, respectively.

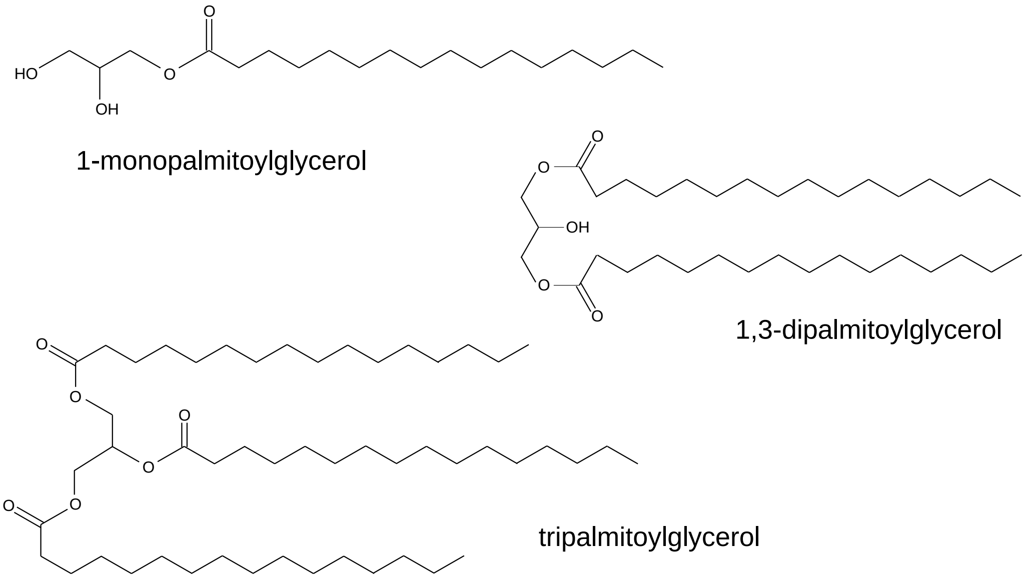

Fig. 1-4. Chemical structures of mono-, di-, and triacylglycerols

As described previously in Fig. 1-3, acylglycerols are the raw material (TAGs) and intermediate products (DAGs, MAGs) of transesterification in the biodiesel production process. Since transesterification is an equilibrium reaction, it is difficult to convert these acylglycerols to FAMEs completely, and they commonly remain in biodiesel as impurities. Since acylglycerols are suspected to be the main cause of solidification, their contents are strictly controlled. The European standard (EN 14214) limits the contents of MAGs, DAGs, and TAGs in biodiesel to less than 0.8, 0.2, and 0.2 wt.%, respectively (Committee for Standardization Automotive Fuels, 2012). Most countries, including Japan, have developed similar specification standards similar to EN 14214 (Hoekman et al., 2012), but some countries have more stringent restrictions. Brazil specifies MAGs, DAGs, and TAGs contents to be 0.7, 0.2, and 0.2 wt.% respectively (Ministry of Agriculture Livestock and Food Supply of Brazil, 2015), while Indonesia restricts MAGs content to less than 0.55 wt.% (Humas EBTKE, 2019).

The melting points of saturated acylglycerols are shown in Table 1-3, compared with saturated FAMEs. The melting points of methyl palmitate and methyl stearate are 28.5 °C and 37.7 °C, respectively, much higher than unsaturated FAMEs such as methyl oleate (-20 °C) and are prone to solidification. On the other hand, acylglycerols have multiple polymorphs with different melting points, but all acylglycerols (MAGs, DAGs,

Table 1-3. Melting points of FAME and acylglycerols

(a) Fatty acid methyl ester (FAME) (Knothe & Dunn, 2009)

FAME	Molecular weight	Melting point (°C)
Methyl palmitate (16:0)	270.4	28.5
Methyl stearate (18:0)	298.5	37.7

(b) Monoacylglycerol (MAG) (Maruyama et al., 1971)

MAG	Molecular weight	Melting point (°C) of each crystal form		
		α	β′	β
1-monopalmitin (16:0)	330.5	66.0	73.0	77.0
1-monostearin (18:0)	358.6	74.0	78.5	80.0

(c) Diacylglycerol (DAG) (Shannon et al., 1992)

DAG	Molecular weight	Melting point (°C) of each crystal form	
		β_2	β_1
1,3-dipalmitin (16:0)	568.9	70.0	72.0
1,3-distearin (18:0)	625.0	77.0	78.0

(d) Triacylglycerol (TAG) (Kellens et al., 1990; Lutton, 1955)

TAG	Molecular weight	Melting point (°C) of each crystal form		
		α	β′	β
Tripalmitin (16:0)	807.3	45.0	52.0-56.0	65.0
Tristearin (18:0)	891.45	54.2	64.0	72.9

and TAGs) have higher melting points than FAMEs, regardless of crystal types. In a review of the Lipid Handbook, Foubert et al. (2007) described various polymorphisms of acylglycerols.

MAG has three crystal forms called α, β′, and β-types, which can be distinguished by X-ray diffraction and various spectroscopic methods. The α-type crystal is a metastable structure formed by cooling a melt of MAG rapidly and irreversibly transitions to the more stable β′-type and further to the most stable β-type crystals after certain transition times. The melting points increase with increasing the stability of crystal in the order of α, β′, and β-types (Table 1-3, b). Although the molecular weight of MAG is only slightly larger than that of the corresponding FAME, the melting point is quite different; for example, 77 °C for β-type monopalmitin and 28.5 °C for methyl palmitate. This difference is due to two hydroxyl groups of MAG, which can form intermolecular hydrogen bonds.

Similarly, TAG has three apparent crystalline forms, α, β′, and β-types, but unlike MAG, often there are additional submodifications with only slightly different x-ray diffraction patterns; for example, β'_1, β'_2 for β′-type, and β_1, β_2 for β-type (Foubert et al., 2007). Although the melting points of α, β′, and β-type crystals are distinctly different, the difference between submodifications are generally small (Foubert et al., 2007). TAG has no hydroxyl group but has high melting points comparable to MAG (Table 1-3, d). This is because TAG has three fatty acids bound to it, and the molecular weight is about three times larger than FAME.

In the case of DAG, β_1 and β_2-type crystals, which correspond to submodifications of β, are generally found (Foubert et al., 2007). As shown in Table 1-3 d, the melting points of both forms are only slightly different (about 2-3 degrees). The melting points of DAG are also comparable to MAG and TAG, probably due to its intermediate properties between MAG and TAG, i.e., one hydroxyl group and medium molecular weight between MAG and TAG.

Studies on the effect of acylglycerols and their polymorphism nature on the solidification behavior of biodiesel are scarce. Chupka et al. (2011) found that α-type MAG precipitated first from biodiesel as it is cooled, but transitioned to β′ or β-type crystal upon slow heating. Sugami et al. (2017) found that the cloud points of mixtures of FAME and MAG coincided with the liquidus temperatures of α-type MAG. However, under ultrasonic treatment, the cloud points corresponding to β′-type MAG were measured instead of α-type, indicating direct crystallization of MAG as β′ form in FAME. The liquidus temperature is a term in physical chemistry and is defined as the temperature given to a mixture above which it becomes completely liquid. Yoshidomi et al. (2017) clarified that once MAG precipitates in FAME, it does not dissolve unless heated to the liquidus temperature of β-type MAG, suggesting the fast melt-mediated crystal transition.

These reports suggest that when MAGs are present in biodiesel, the conventional cold flow properties, such as the cloud point, are useless in indicating the risk of precipitation. This is due to the complex behavior of MAGs, where their crystalline forms change with the surrounding situation. Therefore, the effect of acylglycerols, including their polymorphic phenomena, needs to be carefully observed to develop predictions models of cold flow properties of biodiesel. It will also be necessary to develop new indicators to assess the risk of precipitation properly.

1.4 Cold flow properties

1.4.1 Measurement method

Table 1-4 summarizes the procedures for measuring cold flow properties based on the American Society of Testing and Materials (ASTM).

The cloud point (CP) is defined as the temperature at which the first solid appears in a liquid fuel upon cooling. For the CP measurement, the sample in a sealed glass vial is emerged in a temperature-controlled bath and cooled at the specified rate without agitation until the solid starts to deposit in the liquid sample. The temperature at which the haziness appears is recorded as the CP. If the sample is further cooled well below the CP, the solids will grow to be unable to flow anymore, and this temperature is recorded as the pour point (PP). However, the PP is expressed as an integer value multiple of 1, 2, or 3 by rounding up the measured value.

The CP and PP measurements are easy to perform in the laboratory, but manual measurements can result in some experimental uncertainties. For better reliability, the use of an automatic analyzer equipped with an optical sensor is recommended (Dunn, 2015). However, Coutinho and Daridon (2005) argued that the current CP measurement method does not represent the starting point of the solid formation because it cannot be detected until the solid grows to some extent. The cold filter plugging point (CFPP) is widely accepted as a more practical approach than the CP and PP because it directly represents the risk of clogging fuel filters. In the CFPP measurement, the fuel sample is cooled to a certain temperature and then passed through a wire mesh filter using a vacuum pump. The test is repeated while gradually lowering the fuel temperature. The CFPP is determined as the temperature at which the fuel fails to pass the filter within 60 s. The

Table 1-4. ASTM test methods for diesel and biodiesel cold flow properties (Dunn, 2015)

Property	Test method	Description
Cloud point (CP)	D 2500	Cool a 45 mL sample at a regulated rate; inspect at 1 °C interval; the CP is the temperature at which haziness is visually observed.
CP (Linear cooling rate)	D 5772	Cool a 20 mL sample at a specified rate; crystals are detected by an optical light barrier.
CP (Constant cooling rate)	D 5773	Cool a 150 µL sample at 1.5 °C/min; crystals are detected by light scattering.
Pour point (PP)	D 97	Cool a 45 mL sample at a regulated rate; test at 1, 2, or 3 °C interval; inspect by tilting the test tube. The PP is the lowest temperature at which fluidity is visually confirmed in at least a part of the sample.
PP (Pressure pulsing method)	D 5949	Cool a 150 µL sample at 1.5 °C/min; test at 1, 2, or 3 °C interval; pulse the top surface of the sample with pressurized N_2 gas; surface movement is detected by light scattering.
PP (Tilt method)	D 5950	Cool a 45 mL sample at a stepped rate; test at 1 or 3 °C interval; motion in the tilted test tube is monitored by an optical sensor.
Cold filter plugging point (CFPP)	D 6371	Cool a 45 mL sample at regulated rate; test at 1 °C interval; pass the 20 mL sample through a 45 µm wire mesh filter with a 2 kPa vacuum; the CFPP is the temperature at which the sample fails to flow within 60 s; filterability is monitored visually or by an optical sensor.
Low-tempearture flow test (LTFT)	D 4539	Cool a 200 mL sample at 1 °C/h; test at 1 °C interval; pass the 180 mL sample through a 17 µm wire mesh filter with a 20 kPa vacuum; the LTFT is the lowest temperature at which the sample fails to flow within 60 s; filterability is monitored visually or by an optical sensor.

low-temperature filterability test (LTFT) is a similar method to the CFPP but with a very slow cooling rate and a different filter size to match the actual situation of fuel use in North America.

The above-mentioned properties are measured at a constant cooling rate without stirring. While these are practical, it is questionable whether the properties could help prevent problems during the use of biodiesel. For example, according to the definition, the CP means the temperature at which solidification begins, but some researchers reported that the solidification of biodiesel occurred even at temperatures above the CP (Yu et al., 1998; Tang et al., 2008). High melting point components such as MAGs were confirmed to initiate the precipitation (Tang et al., 2008), but the CP and CFPP were insensitive to low MAG contents (Dunn, 2015). The conventional cold flow properties may not be reliable due to the possible temperature gradients in the sample and supercooling effect (Dunn, 2012). Actually, Lopes et al. collected and compared CPs of binary FAME mixtures from different studies, but the CP values were not consistent (Lopes et al., 2008).

Another method to determine the cold flow properties is differential scanning calorimetry (DSC). Since the DSC requires only a small amount of sample (in the order of mg), it is less affected by heat transfer and provides highly reproducible results. Due to its sensitivity in detecting the heat of melting and solidification, DSC is often used to precisely analyze the information of solid-liquid transition. The use of DSC for determining the CP of fossil fuels has been demonstrated previously, and the results were highly correlated with those obtained by the standardized CP measurement methods (Heino, 1987). For biodiesel, a linear function has been developed to determine the CP from the melting temperature measured by DSC (Dunn, 1999; Ramalho et al., 2012). However, it should be noted that the intensity of the exothermic and endothermic peaks will be very weak if the concentration of the component that relates to the solid-liquid transition is low (Dunn, 2015; Yoshidomi et al., 2017). In such cases, the visual observation helps determine the initial crystallization and the complete melting temperatures (Yoshidomi et al., 2017).

1.4.2 Correlation with the solid-liquid phase diagram

The apparent behavior of cold flow properties results from the physical interaction between the chemical components in the fuel at the molecular level. When the fuel temperature decreases, the solubility of the solutes (precipitated components) in the solvent (fuel) decreases, causing the solidification of certain components. The cold flow properties are closely related to the solid-liquid phase transition of the fuel because they have been developed as parameters for assessing problems related to solid precipitation.

Fig. 1-5 shows the relationship between the solid-liquid phase transition and cold flow properties. A fuel is completely liquid at the temperature T_0, which is higher than the liquidus curve (dashed line). When the fuel temperature decreases and crosses the liquidus line, nucleation and precipitation begin, forming the solid phase. With further cooling, the proportion of the solid phase increases, and when the temperature reaches the solidus curve (dotted line), the fuel becomes all solid.

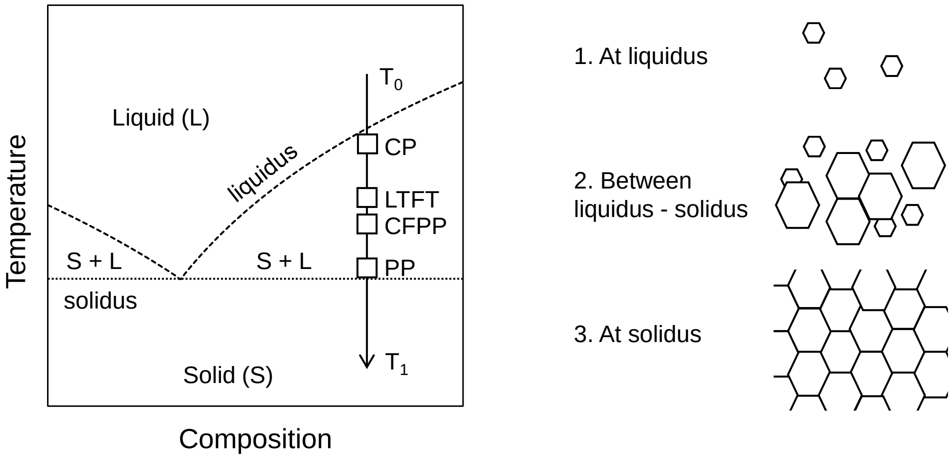

Fig. 1-5. Correlation of the cold flow properties to the solid-liquid phase diagram (left) and solidification progress (right).

The CP is defined as the temperature where the first solid particle is visually observed in the fuel; therefore, it is closely related to the liquidus. At this point, the crystals are extremely small, but scattered lights can be observed by irradiating a laser beam to the fuel. The crystals continue to grow to cloudy waxes. In general, the experimentally determined CP is slightly lower than the liquidus temperature because the crystals need to glow to certain sizes to be detectable by an optical sensor, and there is a supercooling effect due to the measurement upon cooling.

The process of nucleation and crystal growth continues as the fuel is exposed to lower temperatures. At temperatures between the liquidus and solidus lines, the nuclei grow and agglomerate to be visible as solid waxes. When a fuel containing enough solid waxes passes through a filter, the waxes eventually clog the filter. Thus, the cold flow properties, such as the LTFT and CFPP, should correspond to the temperature between the liquidus and solidus lines. As the crystallization process further continues, the agglomerated solid would be enough to stop the fuel flow, and this temperature corresponds to the PP. In general, the PP is slightly higher than the solidus because even if a small fraction of liquid remains inside the solid, it may lose its fluidity.

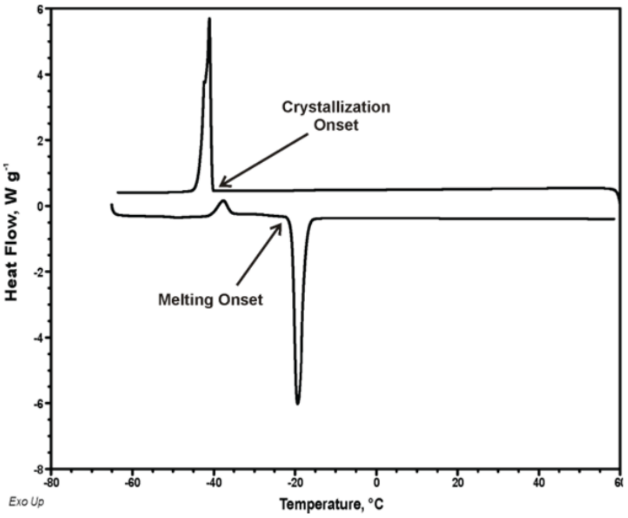

Fig. 1-6. DSC curves of cooling and heating methyl oleate (Dunn, 2012).

Although it is generally challenging to determine the true liquidus temperature of a mixture, DSC analysis can measure an approximation, which is sometimes referred to as the experimental liquidus temperature. Fig. 1-6 above shows an example of DSC curves for pure methyl oleate (FAME18:1) upon heating and cooling. In DSC analysis, the melting point and freezing point can be determined from the onset temperatures of the heating curve (bottom) and cooling curve (top), respectively. However, the measured freezing point of pure FAME is below the melting point due to the supercooling effect (Dunn, 2012), suggesting that the liquidus line should be measured during the heating process to eliminate the effect of supercooling. Mixtures generally have broader melting peaks than pure substances (de Matos et al., 2016; Chabane et al., 2018). In such cases, it is recommended to determine the liquidus temperature based on the peak temperature instead of the onset temperature of the melting peak (Hohne et al., 2003).

1.5 Prediction of biodiesel cold flow properties

One way to improve the cold flow properties of biodiesel is to mix various esters until the desired properties are achieved. Investigations for this aim typically include changes in chemical composition and testing of the resulting properties. Given the combination of hundreds of chemicals, the lengthy experimental process, and costly procedures, the prediction model of the cold flow properties is helpful to eliminate unnecessary trials. It will be useful for the research, manufacture, handling, and storage of biodiesel. The prediction model for biodiesel cold flow properties can be classified into empirical and theoretical methods.

1.5.1 Empirical model

Empirical models are usually developed by correlating a target physical property with the chemical composition of the fuel by linear regression. The contents of saturated or unsaturated esters in biodiesel were commonly used as model variables since they directly affect the cold flow properties. The empirical models are highly dependent on the type of biodiesel and selected variables used to build the model.

Early studies of biodiesel and blend fuels provided some empirical prediction models representing the cold flow properties as linear functions of biodiesel composition, as demonstrated by various research groups (Moser, 2014, 2008; Park et al., 2008; Ramos et al., 2009; Sarin et al., 2009, 2010; Echim et al., 2012; Serrano et al., 2014; Yuan et al., 2017). Most of these studies were conducted to clarify the effect of selected parameters on the cold flow properties. A general expression of such models can be described as Equation (1-1).

$$CFP = c_0 + c_1 x_1 + c_2 x_2 + \cdots + c_n x_n \tag{1-1}$$

where CFP is a target cold flow property, such as the CP. The x_i is the mass fraction of component *i* in biodiesel, and c_i is the coefficient for component *i* determined by linear regression on the experimental data. However, some studies used carbon number, molecular weight, or degree of unsaturation for the variable x_i instead of the mass fraction (Mostafaei, 2018; Razavi et al., 2019).

Table 1-5 summarizes some empirical prediction models for the cold flow properties of biodiesel based on linear regression. In these models, the contents of specific fatty acid methyl esters are chosen as variables. Park et al. (2008) and Sarin et al. (2009, 2010) blended biodiesel from various plant oils, such as rapeseed, soybean, and jatropha, measured the cold flow properties of the blended fuels, and then studied the correlation with the chemical compositions. As a result, they found that the CP and PP (Sarin et al., 2009) and the CFPP (Park et al., 2008; Sarin et al., 2010) could be estimated only from the total content of unsaturated FAMEs. On the other hand, Moser (2008) suggested that the CFPP correlates with the total content of saturated FAMEs and their species. Based on this result, Ramos et al. (2009) introduced the long-chained saturated factor (LCSF) as a weighting parameter to predict the CFPP. Dunn (2018, 2020) proposed a modified empirical correlation (MODEC) model that requires only the content of methyl palmitate to predict the CP and CFPP. However, the deviation was found in coconut biodiesel because the solidification was mainly due to the higher chained esters, such as methyl arachidate (Dunn, 2018).

Recently, prediction models based on the latest applied mathematical algorithms, such as artificial neural networks (Al-Shanableh et al., 2016), ANFIS (Mostafaei, 2018), and support vector machine (Razavi et al., 2019) have also been proposed. Predictions by these modern computational algorithms were generally superior to early prediction models by linear regression. Such algorithms were also applied to correlate FTIR and NIR spectra with the cold flow properties (Baptista et al., 2008; Balabin & Safieva, 2011; Palou et al., 2017; Cunha et al., 2017, 2020). However, the algorithms contain probabilistic elements and complex computation procedures, resulting in long processing times (Balabin & Safieva, 2011).

The empirical model by linear regression is practical because it is simple and easy to calculate. However, it is doubtful that it can be reliably applied to all types of biodiesel. This is because the empirical prediction model is strongly dependent on the type of biodiesel used for linear regression and will have some deviations when applied to

Table 1-5. Empirical models for predicting biodiesel cold flow properties

Author	Biodiesel (FAME)	Prediction model equation
Park, et al. (2008)	Palm, rapeseed, and soybean oils.	$CFPP = -0.4880X + 36.0548\ (0 < X \leq 88)$ $CFPP = -2.7043X + 232.0036\ (88 < X < 100)$ where X is the sum of unsaturated fatty esters (wt.%)
Sarin (2009) and Sarin (2010)	Palm, jatropha, and pongamia oils.	$CP = 0.526(PAME) - 4.992\ (0 < PAME < 45)$ $CP = -0.576(X) + 48.255\ (0 < X \leq 84)$ $PP = 0.571(PAME) - 12.240\ (0 < PAME < 45)$ $PP = -0.626(X) + 45.594\ (0 < X \leq 84)$ $CFPP = 0.511(PAME) - 7.823\ (0 < PAME < 45)$ $CFPP = -0.561(X) + 43.967\ (0 < PAME \leq 84)$ where $PAME$ is the content of methyl palmitate (wt.%) and X is the sum of unsaturated FAME (wt.%).
Ramos, et al. (2009)	Palm, olive, peanut, rapeseed, soybean, sunflower and almond oils.	$CFPP = 3.1417\big(LCSF(B)\big) - 16.477$ $LCSF(B) = 0.1(C16) + 0.5(C18) + 1(C20) + 1.5(C22) + 2(C24)$ where C16, C18, C20, C22, and C24 are the content (wt.%) of methyl palmitate, stearate, arachidate, behenate, and lignocerate, respectively.
Dunn (2018) and Dunn (2020)	Yellow grease, coconut, palm, and soybean oils.	Modified empirical (MODEC) model: $CP = 1/[(-1.02 \times 10^{-4}) \ln y_{C16} - 3.44 \times 10^{-3}] - 273.15$ $CFPP = [(-1.31 \times 10^{-4}) \ln y_{C16} + 3.42 \times 10^{-3}] - 273.15$ where y_{C16} is the content of methyl palmitate (wt.%).

biodiesel with different fatty acid compositions. To improve the empirical model, it would be necessary to collect many data from biodiesel samples produced from a wide variety of feedstocks.

1.5.2 Thermodynamic model

The liquidus temperature can be calculated based on the thermodynamic theory of solid-liquid equilibrium. When a given mixture is in solid-liquid equilibrium at a given temperature and pressure, for all component *i*, the fugacities of component *i* in the liquid phase ($F_i{}^L$) and solid phase ($F_i{}^S$) are equal as follows:

$$F_i{}^L = F_i{}^S \tag{1-2}$$

Hereafter, the superscript letters L and S indicate the liquid and solid phases, respectively. The fugacity can be expressed by either the equation of state or the activity coefficient method, but the latter is often preferred for solid-liquid systems. The expression of F_i by the activity coefficient is described as follows:

$$x_i f_i{}^L \gamma_i{}^L = z_i f_i{}^S \gamma_i{}^S \tag{1-3}$$

where x_i and z_i are mole fractions of component *i* in liquid and solid phases, respectively. The f_i refers to the fugacity of pure component i and γ_i is the activity coefficient of component *i* in the mixture. Generally, the fugacity-ratio ($f_i{}^L/f_i{}^S$) of solid and liquid phases of pure component *i* can be expressed by Equation (1.4) (Prausnitz et al., 1999).

$$\ln\frac{f_i{}^L}{f_i{}^S} = \ln\frac{x_i\gamma_i{}^L}{z_i\gamma_i{}^S} = \frac{\Delta H_{m,i}}{RT_{m,i}}\left[1-\frac{T_{m,i}}{T}\right] - \frac{\Delta c_p}{\mathrm{R}}\left[1-\frac{T_{m,i}}{T}\right] + \frac{\Delta c_p}{\mathrm{R}}\ln\frac{T}{T_{m,i}} \tag{1-4}$$

where $T_{m,i}$ and $\Delta H_{m,i}$ are melting point and enthalpy of fusion of component i. The Δc_p is the difference between the pure component heat capacities of liquid and solid phases. The term *T* refers to the equilibrium temperature. Enthalpy change due to solid-solid transitions may also be included in Equation (1-4) if polymorphism persists (Pereira et al., 2020). In most cases, Equation (1-4) can be simplified into Equation (1-5) without significant consequences since the effects of the heat capacity difference and solid-solid transition are small.

$$\ln\frac{\gamma_i{}^L x_i}{\gamma_i{}^S z_i} = \frac{\Delta H_{m,i}}{RT_{m,i}}\left[1-\frac{T_{m,i}}{T}\right] \tag{1-5}$$

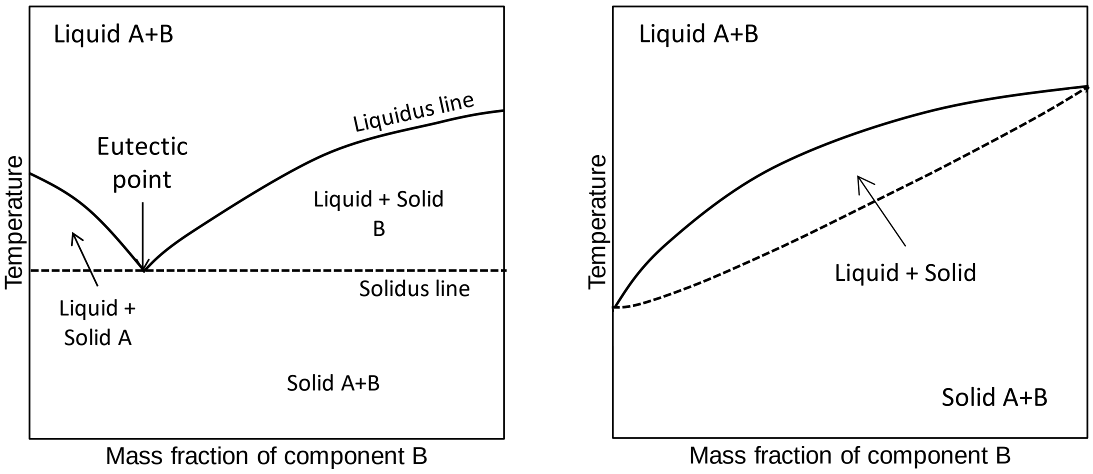

a) Eutectic system (completely immiscible)

b) Ideal solid solution

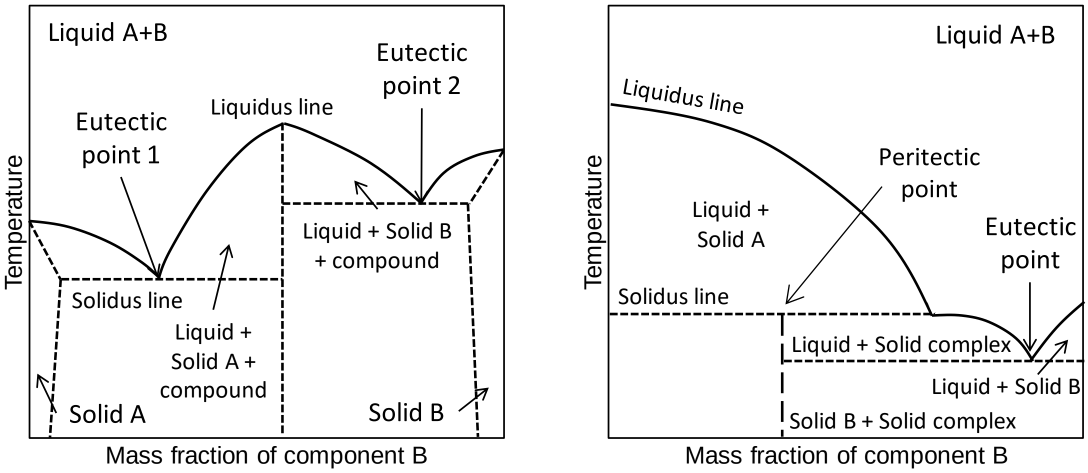

c) Compound formation

d) Peritectic system (solid complex/compound)

Fig. 1-7. Solid-liquid phase behaviors of lipid systems.

(1) Typical solid-liquid phase diagram of lipid systems

In general, there are several types of phase diagrams in binary mixtures of lipid systems, and some typical examples are introduced in Fig. 1-7.

Among these systems, the eutectic system (a) is the most commonly found in triacylglycerols mixtures (Timms, 1984), while the continuous solid solution system (b) is formed by fatty acids mixtures (Inoue et al., 2004). Some mixtures of triacylglycerols involve the formation of compounds, resulting in the phase diagram shown in (c)

(Engström, 1992). Other studies mentioned that fatty acid and fatty ester mixtures formed a peritectic system, in which compound-like species (complexes) were also formed, resulting in a typical phase diagram as illustrated in (d) (de Matos et al., 2015; Robustillo et al., 2014).

For the eutectic and continuous solid solution systems, simple prediction models can be developed by using Equation (1-5). The eutectic system assumes that one solid phase consists of only one component, i.e., different components are immiscible in one solid phase and thus z_i = 1 and ${\gamma_i}^S = 1$. For a binary mixture (component i = 1 and 2), Equation (1-5) could be written as Equations (1-6) and (1-7).

$$\ln {\gamma_1}^L x_1 = \frac{\Delta H_{m,1}}{RT_{m,1}}\left[1 - \frac{T_{m,1}}{T}\right] \tag{1-6}$$

$$\ln {\gamma_2}^L x_2 = \frac{\Delta H_{m,2}}{RT_{m,2}}\left[1 - \frac{T_{m,2}}{T}\right] \tag{1-7}$$

Thus, one equation is given for each component. In general, x_1 and x_2 are the mole fraction of components 1 and 2 in the liquid phase. However, at the liquidus temperature, the amount of solid phase is infinitesimal so that the mixture can be considered entirely in the liquid phase. Therefore, T values obtained by substituting the composition of the mixture into x_1 and x_2 in Equations (1-6) and (1-7) give the liquidus temperatures for components 1 and 2, respectively, and the higher one is the liquidus temperature of the mixture, at which the corresponding component solidifies. As shown in Fig. 1-8, Equations (1-6) and (1-7) give two individual liquidus curves for components 1 and 2, and these associate into a V-shaped liquidus curve. Such a trend is common in eutectic mixtures, in which the intersection between two curves gives the minimum value known as the eutectic point.

On the other hand, the continuous solid solution system assumes that components 1 and 2 can form one solid phase as a solid solution at any ratio. In this case, Equation (1-8) is derived from the Equation (1-5) and $z_1 + z_2 = 1$.

$$\frac{{\gamma_1}^L x_1}{\exp\left[\frac{\Delta H_{m,1}}{RT_{m,1}}\left(1-\frac{T_{m,1}}{T}\right)\right]} + \frac{{\gamma_2}^L x_2}{\exp\left[\frac{\Delta H_{m,2}}{RT_{m,2}}\left(1-\frac{T_{m,2}}{T}\right)\right]} = 1 \tag{1-8}$$

Note that the solid phase activity coefficient is set to unity, assuming that the solid phase is an ideal solution. Solving Equation (1-8) gives a monotonically increasing liquidus curve, as shown in Figure 1-7 (b).

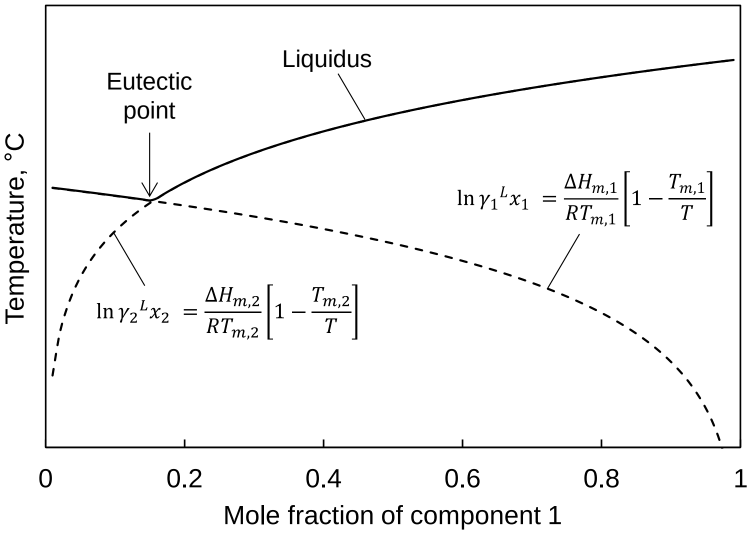

Fig. 1-8. Prediction of liquidus curve by assuming solidification of a pure component.

For the compound formation (Fig. 1-7 (c)) and peritectic systems (Fig. 1-7 (d)), additional information is necessary to model such complicated behaviors. For these systems that make solid complexes due to strong physical interactions (Prausnitz et al., 1999), the mixture can be assumed in reaction equilibrium. This model requires experimental data to assign the reaction equilibrium constant (K_a); it cannot be determined only from pure-component's data (Prausnitz et al., 1999). The detailed calculation procedure for this approach has been demonstrated in the literature (Slaughter & Doherty, 1995).

(2) Application of thermodynamic models for biodiesel system

The approach with Equations (1-5) was performed by various research groups for predicting the CP and liquidus temperature of biodiesel and biodiesel-fossil diesel blends (Imahara et al., 2006; Dunn, 2008). Introducing empirical parameters into the thermodynamic model can help improve the model for predicting cold flow properties other than the CP because the CP was linearly correlated with the PP, CFPP, and LTFT (R. O. Dunn & Bagby, 1995).

The earliest study of the thermodynamic model was carried out by Imahara et al. (2006) for predicting the CP of model biodiesel fuels made of pure FAMEs. The mixtures of FAMEs were well explained by the eutectic model of Equations (1-6) and (1-7) assuming an ideal solution ($\gamma_i^L = \gamma_i^S = 1$), and the calculated liquidus temperatures were in good agreement with the experimentally determined CPs for binary and multi-component mixtures of FAMEs. Based on this result, they argued that the CP could be predicted from the content of saturated FAME in the fuel.

On the other hand, Dunn (2008) showed that the CPs of binary mixtures of FAMEs differed by 4-5 °C from the calculated results by assuming an ideal solution and eutectic system. Dunn compared the calculations in Equations (1-4) and (1-5) and concluded that this deviation was not due to ignoring the effect of heat capacity difference. Probably this deviation is the effect of supercooling. Therefore, Dunn proposed semi-empirical prediction models for CP and CFPP as follows (Robert O. Dunn, 2018, 2020), considering that the CP and CFPP had linear correlations with the liquidus temperature:

$$CP = 0.82(T_{SLE}) - 5.0 \tag{1.9}$$

$$CFPP = 0.99(T_{SLE}) - 8.7 \tag{1.10}$$

where T_{SLE} is the liquidus temperature calculated by using Equation (1.5). The predicted values correlated well with the experimental values for CFPP ($R^2 = 0.977$), although the accuracy was lower for CP ($R^2 = 0.893$).

Although the above studies did not consider the effect of minor components, Yoshidomi et al. (2017) studied prediction for biodiesel containing MAG. Fig. 1-9 shows comparisons of experimental liquidus and predicted curves assuming ideal and non-ideal solutions in various MAG/FAME mixtures. The MAG/FAME mixtures were found to be non-ideal solutions, in which MAG has a high tendency to precipitate. The modified UNIFAC (Dortmund) model (Gmehling et al., 1993) was useful in estimating the activity coefficient in the liquid phase. This accurate prediction also contributed to the discussion of the effect of MAG polymorphism. However, when more than one type of MAGs were present in the mixture, the model did not adequately predict the liquidus temperature of the mixture. This may be due to the formation of solid solutions or complexes between MAGs.

The thermodynamic prediction model for simple mixtures representing biodiesel-fossil diesel blends was also investigated. Binary mixtures consisting of FAAE and *n*-alkane (C14-C18), and FAME and heavy alkanes (> C21) behaved slightly as non-ideal solutions (Chabane et al., 2018; Benziane et al., 2013). The deviation from the ideal solution was found to be more pronounced with longer carbon chains of *n*-alkane.

Similarly, binary mixtures of FAME and aromatics were found to behave as non-ideal solutions (Benziane et al., 2013). These studies claimed that the calculated liquidus curves by the non-ideal models such as UNIQUAC fitted well with the experimental liquidus temperature. However, the effect of acylglycerols in fossil diesel components has not been discussed yet.

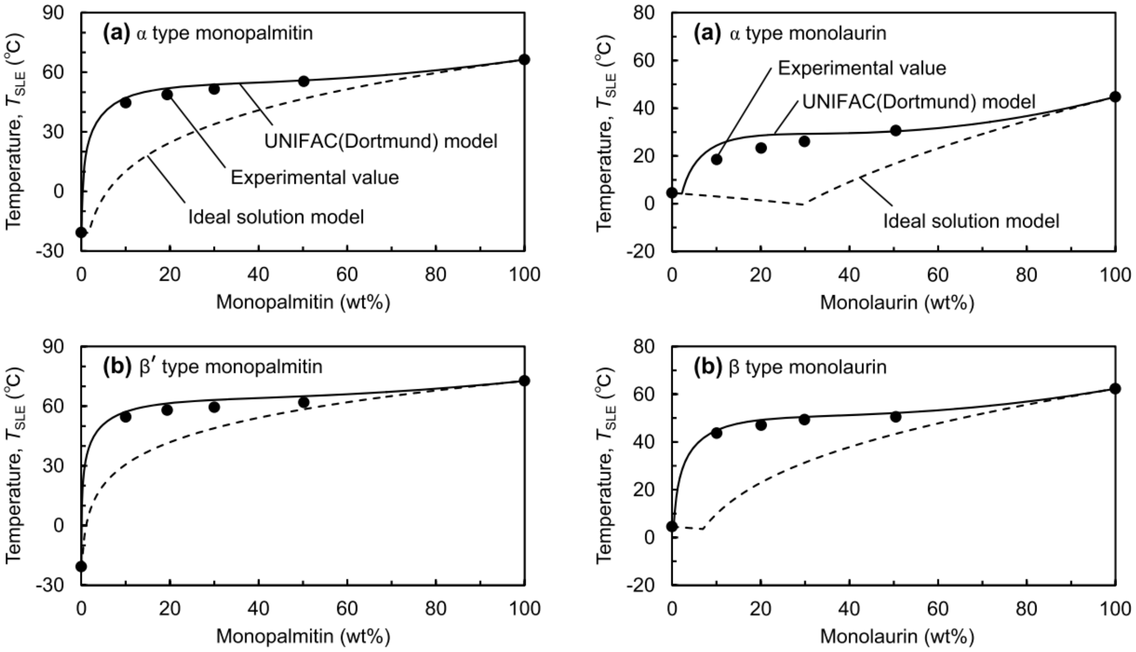

Fig. 1-9. Comparison between the experimental and predicted liquidus temperatures of binary MAG/FAME mixtures (Yoshidomi et al., 2017)

1.6 The objective of this study

Predicting the cold flow properties of biodiesel can be of great help in the research, production, handling, and storage of biodiesel. For more accurate prediction of all types of biodiesel, the thermodynamic models are preferred because prediction can be made only from the chemical composition of the fuel. As discussed in the previous section, minor components such as acylglycerols were found to influence the cold flow properties of biodiesel. Therefore, developing the prediction model without considering its impact is not relevant to the real world. Although the solidification behavior of acylglycerols in biodiesel is not fully elucidated, the interactions between acylglycerols during solidification are still unclear and seemed to be complex.

This study aimed to elucidate the solidification behavior of acylglycerols and their effect on the cold flow properties of biodiesel. The first step in this study was to elucidate the solidification behavior of acylglycerols in FAME, as described in Chapter 2. The interactions between MAGs in solidification will be clarified in Chapter 3, discussing the complicated solidification tendency of MAGs. In Chapter 4, the solidification behavior of binary mixtures of other combinations of acylglycerols (DAG/DAG, TAG/TAG, DAG/MAG, TAG/MAG, DAG/TAG) was clarified, and the effect of each acylglycerol will be summarized. In Chapter 5, a prediction method for actual biodiesel mixtures was proposed and evaluated. The performance and limitations of the model were discussed. Since biodiesel is commonly blended with fossil diesel fuel, the solidification behavior of FAME and MAG in alkanes and aromatic components was also described in Chapter 6.

At the end of this dissertation, critical remarks and prospects are summarized in Chapter 7. This study will serve as a fundamental study for developing thermodynamic prediction models for real biodiesel and blend fuels.

Chapter 2 Solidification Behavior of Acylglycerols in Fatty Acid Methyl Esters

2.1 Introduction

Predicting the values of cold flow properties based on thermodynamic models needs to consider the interactions between chemical components in biodiesel, such as FAME and acylglycerols. Some of these component interactions have been studied in our research group. Mixtures of only FAMEs are typical eutectic systems, and the experimentally determined cloud points for such mixtures are in good agreement with the predicted liquidus temperatures, assuming ideal liquid solutions (Imahara et al., 2006). The liquidus temperature is defined as the temperature above which the mixture becomes completely liquid, while the solidus is the temperature below which the mixture becomes fully solid. The liquidus is a more important predictor of cold flow properties than the solidus because a solid phase can form below the liquidus temperature and even a small amount of solid phase can be problematic.

In contrast, binary mixtures of a FAME and a MAG did not behave as ideal liquid solutions (Yoshidomi et al., 2017). Deviations from ideality are attributed to the two hydroxyl groups in each MAG molecule, which promote solidification. When only one type of MAG is combined with a FAME, the liquidus temperature can be successfully predicted, assuming that a solid phase is formed by a single component (Yoshidomi et al., 2017). However, this assumption is invalid if two or more types of MAG are incorporated in the mixture.

Nevertheless, the behaviors of DAG and TAG components in actual biodiesel mixtures have not yet been clarified. DAG and TAG were expected to exhibit different solidification behaviors from MAG due to their different polarity, molecular weight, and thermodynamic properties. When formulating thermodynamic predictions concerning these mixtures, it is of interest to determine the manner in which these acylglycerols solidify when combined with FAMEs and whether they can form mixed crystals with FAMEs (that is, solid solutions). Phase equilibrium data are necessary to confirm such behaviors, but this information is scarce in the existing literature. Consequently, the present work had the goal of elucidating the thermodynamic behaviors in binary DAG/FAME and TAG/FAME mixtures during solidification, using differential scanning calorimetry (DSC). Two thermodynamic models called the non-solid-solution and solid-solution models, explained in the experimental section, were used to calculate the liquidus temperatures of these binary mixtures and the results were compared with experimental data. This research was also extended to multicomponent mixtures that represent actual biodiesel containing acylglycerols.

The non-ideality of components in the mixture is expressed by activity coefficients, which can be estimated by several models. Simple models with a small number of binary interaction parameters, such as Margules and van Laar equations, have been reported to work very well for simple binary mixtures, such as argon/oxygen and benzene/isooctane (Prausnitz et al., 1999). Wilson equation (Wilson, 1964) is based on local composition theory and has two adjustable interaction parameters for binary mixtures. The Wilson model worked better for miscible mixtures, including mixtures of polar solute in a non-polar solvent, but having trouble predicting immiscibility (Prausnitz et al., 1999). Non-random, two-liquid (NRTL) equation (Renon & Prausnitz, 1968) was derived from the Wilson Equation, introducing two adjustable parameters and a non-randomness constant that can be determined arbitrarily. The NRTL model was found to be useful for mixtures with highly different polarity, which causes partial or total immiscibility. Later, the universal quasi component activity coefficient (UNIQUAC) (Abrams & Prausnitz, 1975) model was developed, based on the local composition concept that considers the effect of entropy and molecular interaction. The UNIQUAC model worked well for many applications, including partial or complete immiscibility systems, though only two parameters. However, the models mentioned above require the parameters determined from the experimental phase equilibrium data.

The UNIQUAC model was extended to the UNIQUAC functional group activity coefficient (UNIFAC) (Fredenslund et al., 1975). The UNIFAC model adapts the concept of UNIQUAC and uses the information of functional groups of molecules in the mixture. In this model, the interaction parameters of some representative functional groups have been determined beforehand from many experimental data and published as a database so that the activity coefficient can be calculated for any chemical substance from the information of the functional groups.

This study calculated the activity coefficient using a modified version of the UNIFAC, called the UNIFAC (Dortmund) method (Gmehling et al., 1993), since the model can express the effect of temperature very well.

2.2 Experimental procedures

2.2.1 Materials and analytical methods

High purity samples of FAME, MAG, DAG and TAG were purchased and used as received without purification. The manufacturers and purities of the samples are summarized in Table 2-1. Binary DAG/FAME and TAG/FAME mixtures as well as multicomponent mixtures of FAMEs with MAGs, DAGs and TAGs were prepared in various combinations and ratios.

DSC analysis (DSC-60A, Shimadzu Corp., Kyoto, Japan) was performed to evaluate the mixtures' liquidus temperatures. In preparation for each analysis, the mixture was placed in an open aluminum pan under a nitrogen flow (50 mL/min), heated until fully melted, and then cooled until the first exothermic peak appeared. The sample was then reheated, during which time the DSC profile was recorded. To test the significance of the measurement method to the obtained pure component and mixtures heating properties, sample mass was varied from 1-10 mg, while the heating rate was varied from 1-10 °C/min. The temperature at the top of the highest endothermic peak was defined as the liquidus temperature, since this temperature gives a good approximation of the mixture's liquidus (Höhne et al., 2003). The peak area of the corresponding peak was determined as the liquidus enthalpy.

For each pure sample, the melting point and enthalpy of fusion were estimated from the onset temperature and the area of the endothermic peak, respectively. Each experiment (including the experiment with the mixtures) was conducted three times and the mean values of temperature and enthalpy are reported herein. To indicate the experimental uncertainty, the maximum and minimum deviations from the mean are also shown. In these trials, indium and zinc were used for temperature calibration purposes for the instrument, and α-alumina was used as an inert reference material to record the difference in heat flow to the sample and reference material.

Table 2-1. Pure components used in this study.

Name	Abbrev.	Manufacturer	Purity, % (GC)
Methyl laurate	FAME12:0	Sigma-Aldrich Japan, Tokyo, Japan	99.5
Methyl stearate	FAME18:0	Nacalai Tesque Inc., Kyoto, Japan	99.5
Methyl oleate	FAME18:1	Sigma-Aldrich Japan, Tokyo, Japan	99.0
1-Monolaurin	MAG12:0	Nu-Chek Prep, Inc., MI, USA	99.0
1-Monopalmitin	MAG16:0	Olbracht Serdary Research Laboratories (OSRL), Toronto, Canada	99.0
1-Monostearin	MAG18:0	Nu-Chek Prep, Inc., MI, USA	99.0
1-Monoolein	MAG18:1		99.0
1,3-Dilaurin	DAG12:0		99.0
1,3-Dipalmitin	DAG16:0		99.0
1,3-Distearin	DAG18:0	OSRL, Toronto, Canada	99.0
1,3-Diolein	DAG18:1	Larodan Fine Chemicals AB, Solna, Sweden	99.0
Trilaurin	DAG12:0	Tokyo Chemical Industries, Tokyo, Japan	98.0
Tripalmitin	TAG16:0	OSRL, Toronto, Canada	99.0
Tristearin	TAG18:0		99.0

*The purities are supplier-guaranteed values.

2.2.2 Thermodynamic models

The liquidus temperature (T) was calculated based on thermodynamic models and the theory of solid-liquid equilibrium as previously described in section 1.5.2, as follows.

$$\ln\frac{\gamma_i{}^L x_i}{\gamma_i{}^S z_i} = \frac{\Delta H_{m,i}}{RT_{m,i}}\left[1-\frac{T_{m,i}}{T}\right] \qquad (2\text{-}1)$$

In this work, the solid phase was assumed to be ideal, meaning that $\gamma_i{}^S$ had a value of 1. Meanwhile, the liquid phase was assumed as non-ideal and determined by the modified UNIFAC (Dortmund).

(1) Calculation of liquid phase activity coefficient

The UNIFAC (Dortmund) (Gmehling et al., 1993) calculates activity coefficient

(γ_i) as the sum of combinatorial activity coefficient (γ_i^C) and residual activity coefficient (γ_i^R) as follows.

$$\ln \gamma_i = \ln \gamma_i^C + \ln \gamma_i^R \tag{2-2}$$

The combinatorial activity coefficient estimates the effect of molecular size and volume difference of the interacting species *i*. This term was expressed empirically by Equation (2-3).

$$\ln \gamma_i^C = 1 - V'_i + \ln V'_i - 5q_i\left(1 - \frac{V_i}{F_i} + \ln \frac{V_i}{F_i}\right) \tag{2-3}$$

The auxiliary properties of component *i*, volume fraction (V_i), area fraction (F_i), and modified volume property (V'_i), are calculated by the following Equations (2-4) to (2-8).

$$V'_i = \frac{r_i^{3/4}}{\sum_j x_j r_j^{3/4}} \tag{2-4}$$

$$V_i = \frac{r_i}{\sum_j x_j q_j} \tag{2-5}$$

$$r_i = \sum v_k^{(i)} R_k \tag{2-6}$$

$$F_i = \frac{q_i}{\sum_j x_j q_j} \tag{2-7}$$

$$q_i = \sum v_k^{(i)} Q_k \tag{2-8}$$

where r_i and R_k are the relative van der Waals volume of component *i* and subgroup *k*, respectively. The terms q_i and Q_k are the relative van der Waals surface area of component *i* and subgroup *k*. The values of these parameters were obtained from the literature (Gmehling et al., 1993).

The residual activity coefficient is contributed by the entropy effect of each functional group that exists in the mixture, obtained by using Equation (2-9).

$$\ln \gamma_i^R = \sum_k v_k^{(i)}\left(\ln \Gamma_k - \ln \Gamma_k^{(i)}\right) \tag{2-9}$$

where $v_k^{(i)}$ is the number of functional group *k* in component *i*. The Γ_k refers to the group activity coefficient of group *k* in the mixture, while the $\Gamma_k^{(i)}$ is that in pure component *i*. These parameters were determined by Equation (2-10).

$$\ln \Gamma_k = Q_k\left(1 - \ln(\sum_m \Theta_m \Psi_{mk}) - \sum_m \frac{\Theta_m \Psi_{km}}{\sum_n \Theta_n \Psi_{nm}}\right) \tag{2-10}$$

The indexes *k*, *m*, and *n* refer to functional groups in the mixture. In Equation (2-10), the group area fraction (Θ_m) and group mole fraction (X_m) were calculated by the following expressions:

$$\Theta_m = \frac{Q_m X_m}{\sum_n Q_n X_n} \tag{2-11}$$

$$X_m = \frac{\sum_j v_m{}^{(j)} x_j}{\sum_j \sum_n v_n{}^{(j)} x_j} \tag{2-12}$$

Meanwhile, the temperature-dependent UNIFAC group interaction parameter between groups n and m (Ψ_{nm}) was calculated by Equation (2-13). Note that the value of Ψ_{nm} is not equal to that of Ψ_{mn}.

$$\Psi_{nm} = \exp\left(\frac{a_{nm} + b_{nm}T + c_{nm}T^2}{T}\right) \tag{2-13}$$

The constants a_{nm}, b_{nm}, and c_{nm} are empirically determined and available in the literature (Gmehling et al., 1993). The value of Ψ_{mn} was evaluated at the liquidus temperature T.

(2) Prediction models for liquidus temperature

Two models were applied to calculate Equation (2-1). The first of these was the non-solid-solution (NSS) model, in which the different components are considered to be immiscible in a solid phase. It is well known that a eutectic system and its solid phase consist of only a single component (i.e., z_i = 1). In the case of a binary eutectic mixture, Equation (2-1) can be rearranged to

$$\gamma_1{}^{\mathrm{L}} x_1 = \exp\left[\frac{\Delta H_{m,1}}{RT_{m,1}}\left(\frac{T - T_{m,1}}{T}\right)\right] \tag{2-14}$$

$$\gamma_2{}^{\mathrm{L}} x_2 = \exp\left[\frac{\Delta H_{m,2}}{RT_{m,2}}\left(\frac{T - T_{m,2}}{T}\right)\right]. \tag{2-15}$$

As shown in Fig. 2-1, equations (2-14) and (2-15) give a V-shaped liquidus line. The intersection of the two associated curves is termed the eutectic point.

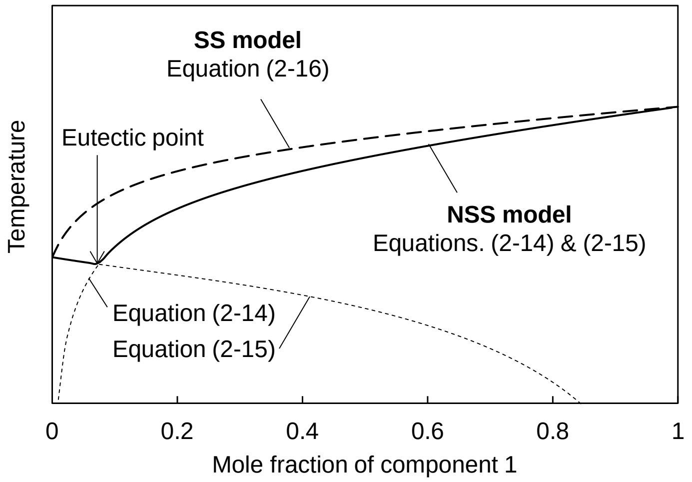

Fig. 2-1. Comparison of liquidus temperature predicted by NSS and SS models

The second model is known as the solid-solution (SS) model. This model allows multiple components to form mixed crystals made of a solid solution (i.e., $z_i \neq 1$). Because $z_1 + z_2 = 1$ for a binary mixture, Equation (2-1) can be rewritten as

$$\gamma_1{}^{\mathrm{L}} x_1 / \exp\left[\frac{\Delta H_{m,1}}{RT_{m,1}}\left(\frac{T - T_{m,1}}{T}\right)\right] + \gamma_2{}^{\mathrm{L}} x_2 / \exp\left[\frac{\Delta H_{m,2}}{RT_{m,2}}\left(\frac{T - T_{m,2}}{T}\right)\right] = 1 \qquad (2\text{-}16)$$

This equation gives a monotonically increasing liquidus curve in Fig. 2-1. In the present work, Equations (2-2) and (2-3) were solved using algorithms written in Microsoft Visual Basic for Applications in Excel (Microsoft Corp., Redmond, WA, USA). The overall algorithm of the calculation is shown in Fig. 2-2.

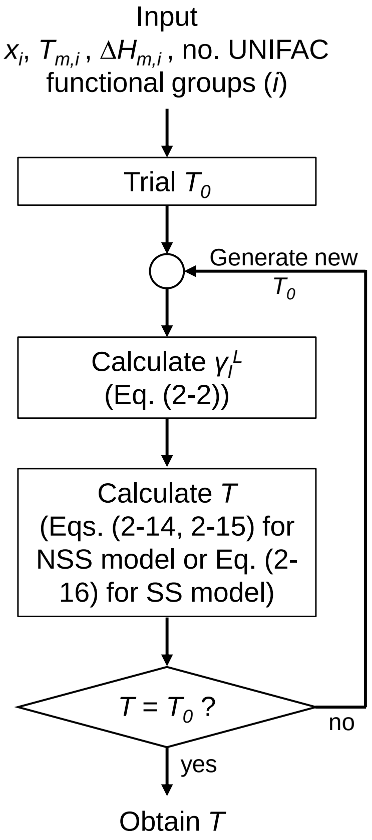

Fig. 2-2. Calculation algorithm for estimating the liquidus temperature by thermodynamic models.

2.3 Results and discussion

2.3.1 Effect of DSC measurement conditions

It was known that the results of DSC measurement are sensitive to the measurement condition, such as sample mass and heating rate. First, the effect of these variables when measuring a pure component (DAG12:0) and binary mixture (DAG12:0/FAME18:0) was investigated to select an appropriate condition for measuring the liquidus temperature of the studied mixtures. The effect of sample mass was studied by varying sample mass from 1 to 10 mg, while the measurement was conducted at 10 °C/min. The effect of the heating rate was also investigated by fixing the sample mass at 10 mg while varying the heating rate from 1 to 10 °C/min.

(1) Pure component

DSC profiles of the melt crystallized DAG12:0 are shown in Fig. 2-3. The melting point indicated in Fig. 2-3 was obtained from the onset temperature of the first endothermic peak. As expected, a larger sample mass and heating rate caused a broader peak signal, resulting in a shift of peak temperature. Analysis of the DSC profiles in Fig. 2-3 (a) showed that increasing the sample mass from 1.3 to 10.5 mg shifted the melting point of DAG12:0 by about only 1.2 degrees, suggesting the effect of sample mass was relatively insignificant.

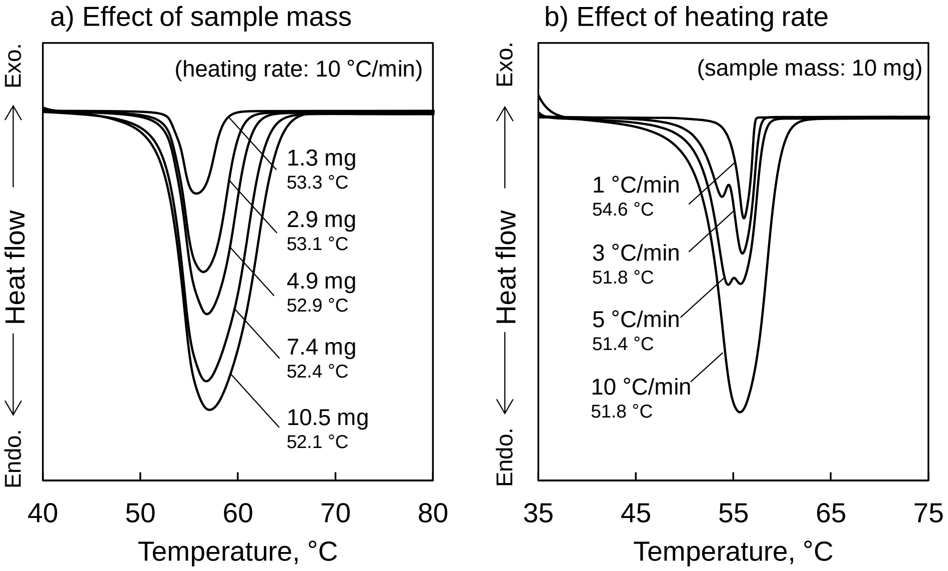

Fig. 2-3. DSC profiles of pure DAG12:0 measured with various conditions.

The heating rate, however, affected the DSC profiles significantly. The melting point of DAG12:0 heated at 10 °C/min were almost similar with that of 3 and 5 °C/min, around 51.4 to 51.8 °C. However, the melting point measured at 1 °C/min was significantly higher at 54.6 °C. The DSC profiles in Fig. 2-3 (b) also indicate that the measurement results at 3 and 5 °C/min produced an additional peak at a higher temperature close to the peak produced by heating at 1 °C/min. Since DAG has two polymorphs with slightly different melting points, the two peaks might be due to the melting of β_2 and β_1-type crystals. This suggests that slow heating enhanced the transition of DAG crystals from β_2 to β_1-type, and the transition was completed by heating at 1 °C/min.

(2) Binary mixtures

Fig. 2-4 shows the effect of sample mass and heating rate on determining the liquidus temperature when a binary mixture of DAG12:0/FAME18:0 (58.7 wt.% DAG) was analyzed by DSC.

Two clear endothermic peaks are observed in these DSC profiles; the peaks on the low and high temperature sides correspond to the solidus and liquidus temperatures, respectively. In Fig. 2-4 (a), an additional small peak is observed between the solidus and liquidus when the sample mass is small. This peak might correspond to the solid-solid transition. For mixtures, the liquidus temperature was evaluated from the peak top temperature. Increasing the sample mass from 1.4 to 9.9 mg and the heating rate from 1 to 10 °C/min increased the liquidus temperature from 49.8 to 50.7 °C and from 49.3 to 50.7 °C, respectively. However, the effects of these variables were not as severe in these ranges.

Based on these results, the heating rate of 10 °C/min and the sample mass of about 10 mg were selected; the fast heating rate was to prevent crystal transitions of acylglycerols during the measurement, and the relatively large sample mass was intended to evaluate the enthalpy of fusion accurately. These conditions followed the previous studies (Yoshidomi et al., 2017). This result indicates that the liquidus determination procedure hereafter included the effect of heat transfer, but its influence is limited.

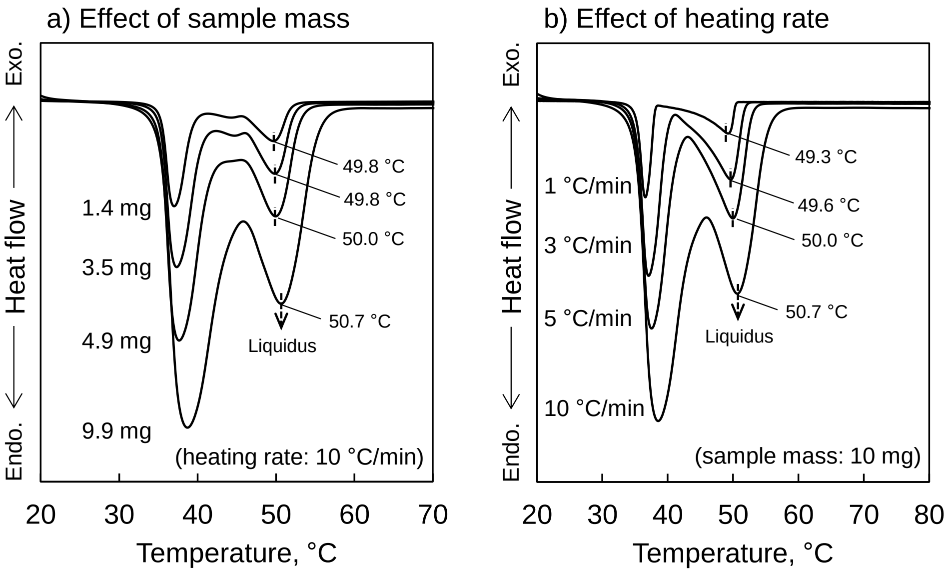

Fig. 2-4. DSC profiles of a binary mixture of DAG12:0/FAME18:0 (58.7 wt% DAG12:0) measured with various conditions.

2.3.2 Pure component properties

The thermodynamic models used in this chapter incorporated the pure component properties $T_{m,i}$ and $\Delta H_{m,i}$ and these values were determined based on DSC analyses of each component, as summarized in Table 2-2. Note that the experimental uncertainty was −0.8 to +1.3 °C for the melting points and −2.0% to +1.1% for the enthalpy values. Because the values in Table 2-2 were consistent with those previously reported (Maruyama et al., 1971; Gunstone et al., 2007), they were considered suitable for use in the subsequent calculations.

Acylglycerols can take multiple crystalline forms (that is, polymorphs) with varying thermodynamic properties (Gunstone et al., 2007). All pure MAGs have three forms, termed α, β′ and β-types, for which the melting points increase in the order of α < β′ < β. The properties of all crystalline forms of the pure acylglycerols were determined and shown in Table A1 in Appendix. However, Table 2-2 shows only the data that were used in the calculations. In the case of the saturated MAGs (12:0, 16:0, and 18:0), α-type crystal data were used because, during the present DSC analyses, the liquidus temperatures attributed to the α-type MAGs were observed in subsequent assessments of mixtures containing MAGs. This was also the case in our previous study (Yoshidomi et

Table 2-2. Properties of the pure components

Component	Number of UNIFAC functional group							Crystal type	Melting point (°C)	Enthalpy of fusion (kJ mol^{-1})
	CH_3	CH_2	CH	CH=CH	OH(p)	OH(s)	CH_2COO			
FAME12:0	2	9	-	-	-	-	1	-	4.5	36.4
FAME18:0	2	15	-	-	-	-	1	-	38.4	62.2
FAME18:1	2	13	-	1	-	-	1	-	-20.7	41.6
MAG12:0	1	11	1	-	1	1	1	α	44.8	22.4
MAG16:0	1	15	1	-	1	1	1	α	66.4	34.1
MAG18:0	1	17	1	-	1	1	1	α	74.2	39.2
MAG18:1	1	15	1	1	1	1	1	β	35.0	49.4
DAG12:0	2	20	1	-	1	-	2	β_1	57.3	79.2
DAG16:0	2	28	1	-	1	-	2	β_1	73.4	111.4
DAG18:0	2	32	1	-	1	-	2	β_1	73.9	129.9
DAG18:1	2	28	1	2	1	-	2	β_1	25.8	88.4
TAG12:0	3	29	1	-	-	-	3	β	46.3	118.4
TAG16:0	3	41	1	-	-	-	3	β	63.3	132.4
TAG18:0	3	47	1	-	-	-	3	β	73.8	181.1

al., 2017). On the other hand, in the case of the unsaturated MAG (18:1), β-type crystal data was used in the calculations because β-type MAG was observed as a result of the rapid crystal transition of this unsaturated compound from α to β-type during the DSC analysis.

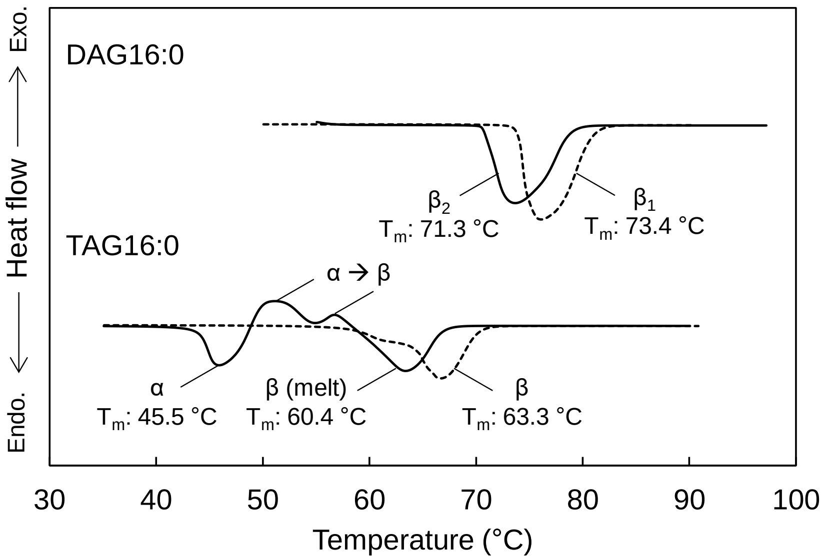

Fig. 2-5. DSC profiles obtained from pure DAG16:0 and TAG16:0 on heating at 10 °C/min (dashed and solid lines show data for as-received samples and samples after melt crystallization, respectively).

All pure DAGs can exist as either β_1 or β_2-type crystals, with the melting point of the β_1 variant being higher. The β_1-form is typically produced by crystallization from a solvent, while the β_2-form is obtained via crystallization from the melt (Shannon et al., 1992). Fig. 2-5(top) shows the DSC data for the as-received DAG16:0 sample during its initial melting (dashed line) and during remelting after rapid cooling (solid line). The positions of the endothermic peaks in these plots appear to correspond to β_1 and β_2-type crystals, respectively. In the present study of binary mixtures of DAGs and FAMEs, the precipitation of each DAG in β_1 form was expected to occur, because the FAMEs could be considered to act as solvents. On this basis, the properties of the β_1-type shown in Table 2-2 were used to predict liquidus temperatures although, because the β_1 and β_2-types have very similar properties, the form that was selected had no significant effect on the calculation results.

Although the polymorphism of TAGs is more complicated than those of MAGs and DAGs, simple monoacid TAGs containing three identical fatty acid moieties have been reported to produce either α, β′ or β-type crystals, similar to the behavior of MAGs (Gunstone et al., 2007). The β-type can be produced either directly via solvent crystallization or indirectly through a crystal transition from the α-type, with the latter showing a slightly lower melting point due to crystal imperfections (Kellens et al., 1990). The present work confirmed this behavior, as depicted in Fig. 2-5(bottom), in which the DSC data show the melting of a β-type TAG obtained from solvent crystallization (dashed line) and that of an α-type TAG produced by melt crystallization (solid line). Table 2-2 summarizes the properties of the β-type TAGs obtained from solvent crystallization that were used in the calculations, again because the FAMEs could be considered as solvents in the TAG/FAME mixtures.

2.3.3 Solidification behavior of acylglycerols in FAMEs

Fig. 2-6 presents the DSC plots obtained from binary mixtures of DAG12:0 and FAME18:0 combined in varying ratios. Two endothermic peaks can be seen in these plots and in some cases these overlap. The peaks appearing at higher temperatures were assigned to the liquidus transition while the lower temperature peaks were attributed to the solidus. The liquidus temperatures from these DSC analyses were plotted as functions of the DAG or TAG mole fraction for various binary DAG/FAME and TAG/FAME mixtures, as presented in Figs. 2-7 and 2-8, respectively. The experimental uncertainties in these temperatures were −0.50 to +0.32 °C for the DAG/FAME specimens and −0.32 to +0.24 °C for the TAG/FAME mixtures.

(1) DAG and FAME mixtures

Fig. 2-7 shows the results for the DAG/FAME mixtures, with data points for the pure FAME at the left end of each plot and pure DAG at the right end. In the case of the data in Figs. 2-7(a) and (b), for which the melting points of the DAG and FAME were quite different, the liquidus temperature is seen to have initially increased rapidly when each DAG was added to the pure FAME, after which further increases in the DAG content resulted in more gradual increases. These trends indicate that the DAGs precipitated out of the FAMEs even at very low concentrations. Similar behavior was previously observed

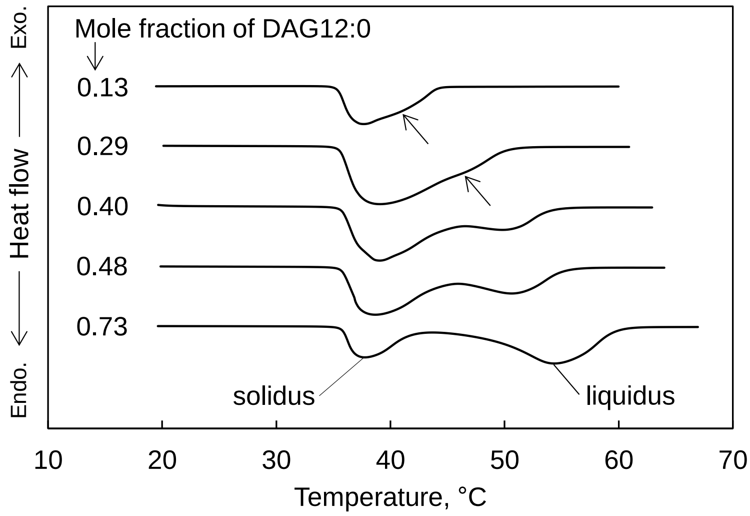

Fig. 2-6. DSC profiles obtained from binary DAG12:0/FAME18:0 mixtures on heating at 10 °C/min.

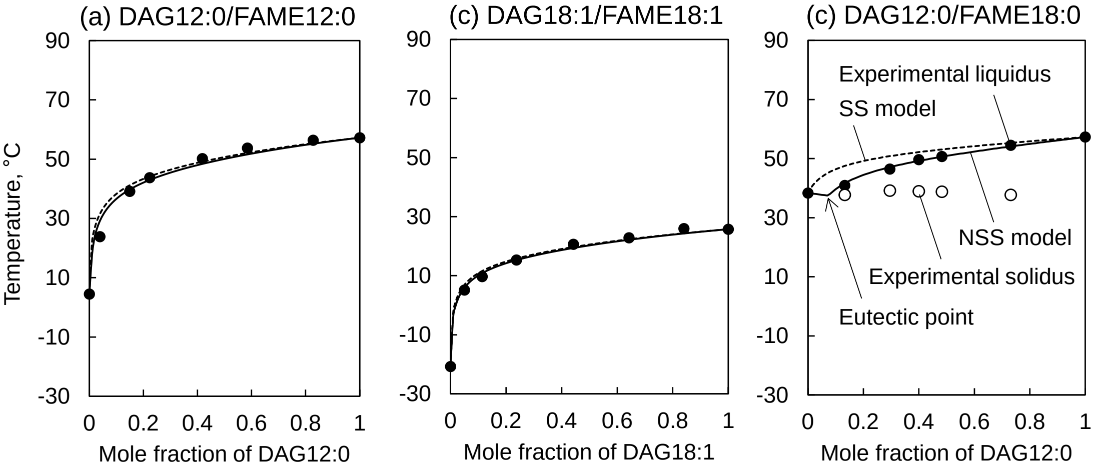

Fig. 2-7. Experimental and calculated liquidus temperatures for various binary DAG/FAME mixtures.

in trials using MAG/FAME mixtures (Yoshidomi et al., 2017). It is also worth noting that the shapes of these liquidus curves were similar regardless of whether the DAG or FAME was saturated or unsaturated.

The liquidus curves calculated using the NSS (solid line) and SS (dashed line) models were in good agreement with the experimental results. In the case of the mixtures shown in Figs. 2-7 (a) and (b), the results obtained from the NSS and SS models almost overlapped, as is common in the case of binary mixtures made with components having very different melting points. The NSS model (Equations (2-14), (2-15)) gives two liquidus curves for components 1 and 2. These two curves can be associated into a V-shaped curve, and their intersection point is called the eutectic point. However, in Figs. 2-7(a) and (b), due to the large difference in melting points between two components (DAG and FAME), the eutectic point calculated by the NSS model was too close to the pure FAME side of the plot to be observed, resembling a monotonically increasing curve, which was indistinguishable from the SS model. Thus, it was not possible to determine which model corresponded to the actual solidification behavior of these DAG/FAME mixtures, but the simple NSS model would be better for practical predictions.

For this reason, a DAG12:0/FAME18:0 mixture was also assessed, because these two components have similar melting points, with the results shown in Fig. 2-7(c). The data for this specimen does not exhibit the steep increase in liquidus temperature that was observed for the other three mixtures, but instead describe a V-shaped curve that is consistent with the NSS model (solid line). As shown in Fig. 2-6, mixtures having these two components also exhibited solidus points, and these are plotted as open circles in Fig. 2-7(c). The points were roughly constant regardless of the mixture composition, with the mean solidus temperature of 38.4 °C (corrected sample standard deviation, 0.65 °C). This value was approximately equal to the calculated eutectic temperature of 37.6 °C, with an absolute deviation below 1 °C. These results suggest that the DAG12:0/FAME18:0 mixtures exhibit a typical eutectic behavior, meaning that the DAG12:0 evidently precipitated as a pure solid phase.

The eutectic behavior was also confirmed by enthalpy analysis, as shown in Fig. 2-8. The enthalpy diagram was established by plotting the enthalpy of liquidus or solidus peak as a function of the composition. In DAG12:0/FAME18:0 (Fig. 2-8(a)), the enthalpy of solidus shows a linear increase with the increase of DAG12:0. Contrary, the enthalpy of liquidus shows a linear decrease. This behavior indicates that DAG12:0/ FAME18:0 is a typical eutectic system. Note that the liquidus enthalpy should be maximum at the eutectic point, but such behavior did not appear in Fig. 2-8 because the eutectic point was outside the measurement region (DAG12:0 < 0.13). Meanwhile, DAG12:0/FAME12:0 (Fig. 2-8 (b)) shows a similar trend for liquidus enthalpy. Since this tendency was also observed in DAG18:1/FAME18:1, it can be concluded that DAG/FAME mixtures generally develop simple eutectic systems. Thus, the NSS model predicted the liquidus curves of the DAG/FAME mixtures very well.

For all DAG/FAME mixtures, the average absolute deviation between the experimentally determined liquidus temperatures and those predicted by the NSS model was 2.0 °C. Therefore, the NSS model performed well within our expectations. The deviation tended to be slightly larger for mixtures with low mole fractions of DAG (less than 0.1). This trend may be due to the steep change in liquidus temperature in this region.

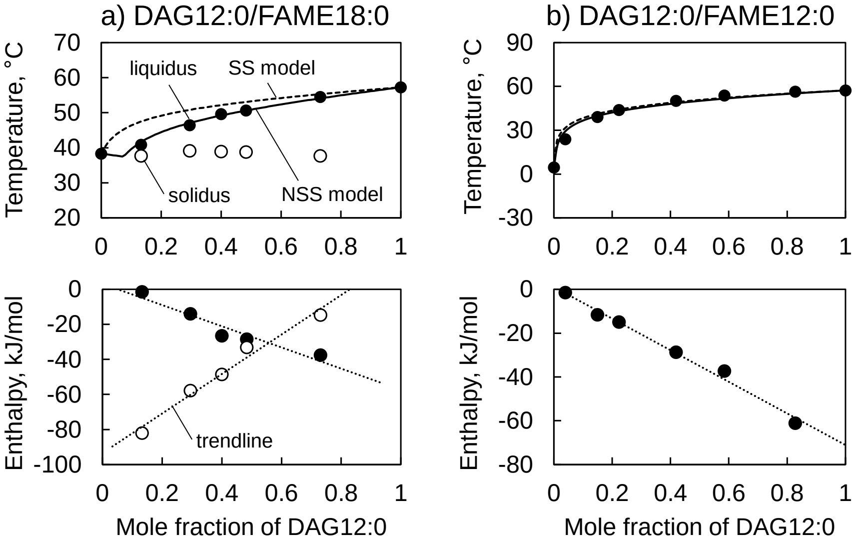

Fig. 2-8. Phase diagram (top) and enthalpy diagram (bottom) of a) DAG12:0 / FAME18:0 and b) DAG12:0/FAME12:0.

(2) TAG and FAME mixtures

Fig. 2-9 shows the results for the TAG/FAME mixtures. The trends for the mixtures in Figs. 2-9(a) and (b), for which there were large melting point differences, are similar to those for the DAG/FAME mixtures. That is, the liquidus temperatures increased steeply at low TAG concentrations but the subsequent increases were slow. In the case of Fig. 2-9(c), with a small melting point difference, the changes in the liquidus and solidus temperatures appear to show a eutectic system (as was obtained from the DAG/FAME system).

Eutectic behavior was also observed in the enthalpy diagrams, as shown in Fig. 2-10. For mixtures with large melting point differences (Fig. 2-10(a)), the liquidus enthalpy shows a linear decline, similar to the case of DAG/FAME. In TAG12:0/ FAME18:0 (Fig.

2-10(b)), which is the case with a small melting point difference, the eutectic point is clearly observed when the TAG12:0 content is around 0.25, so the liquidus enthalpy shows the maximum value while that of solidus is minimum at this composition. This is typical eutectic behavior. Therefore, the evidence suggests that the studied TAGs were also immiscible with FAMEs in a solid phase.

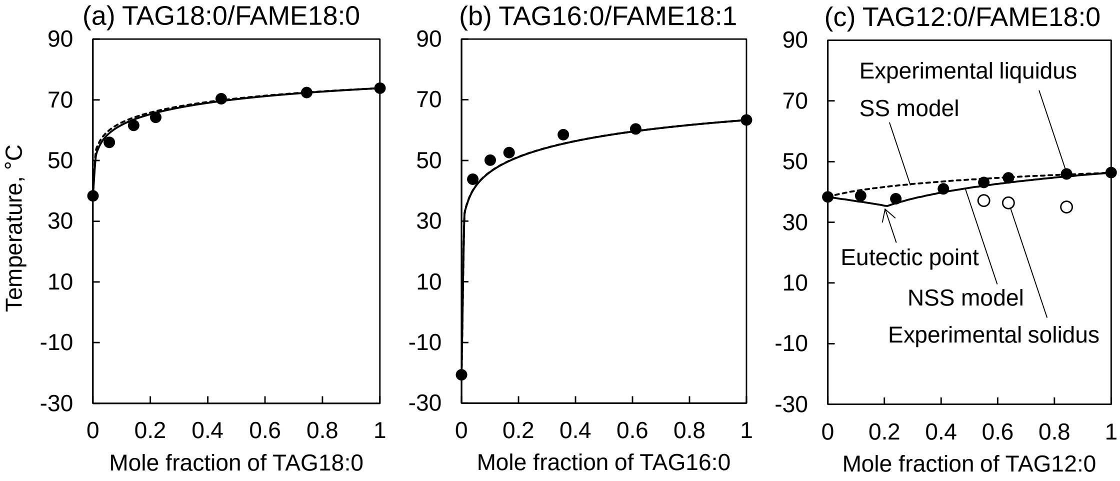

Fig. 2-9. Experimental and calculated liquidus temperatures for various binary TAG/FAME mixtures.

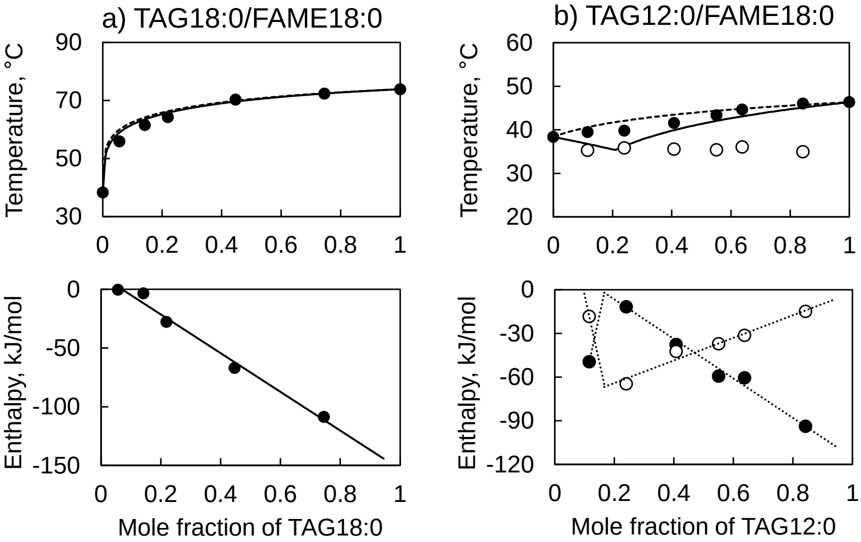

Fig. 2-10. Phase diagram (top) and enthalpy diagram of a) TAG12:0/FAME18:0 and b) TAG18:0/FAME18:0.

However, several researchers (Baker et al., 2015; Mohanan et al., 2015) have reported that certain combinations of TAGs and FAMEs can form solid compounds (that is, mixed crystals). For example, a TAG having one stearic and two oleic acid moieties was found to form solid compounds when combined with methyl stearate in a 1:1 ratio (Baker et al., 2015). Similar behavior was observed in mixtures of a TAG with palmitic and oleic acids groups and methyl palmitate (Mohanan et al., 2015). Thus, not all TAG/FAME mixtures represent simple eutectic systems. Even so, the NSS model was evidently better than the SS model in terms of predicting liquidus temperatures, because these mixtures appear to form solid compounds only in specific combinations and at certain compositional ratios. Furthermore, if the components have significantly different melting points, the NSS and SS models generate very similar results, even for non-eutectic systems. It should be noted that DAG/FAME mixtures may also form solid compounds in certain combinations and at specific ratios, although this has not yet been demonstrated.

Compared with the results obtained from the DAG/FAME mixtures, the data for the TAG/FAME specimens exhibit some deviations between the experimental data and the values calculated using the NSS model, in the range of approximately ± 4 °C. These discrepancies can possibly be attributed to the limitations of the UNIFAC (Dortmund) method in predicting systems with larger and more complex molecular structures, and the effects of the formation of solid compounds between TAGs and FAMEs.

(3) Comparison of MAG, DAG and TAG results

Fig. 2-11 compares the thermodynamic characteristics of MAG16:0, DAG16:0, and TAG16:0 in combination with FAME18:1, as well as those of a binary FAME16:0/FAME18:1 mixture. As shown in Fig. 2-11(a), as the mole fraction of FAME16:0 (acting as the solute) in FAME18:1 (acting as the solvent) was increased, the liquidus temperature slowly increased. In contrast, as the mole fractions of MAG16:0, DAG16:0 and TAG16:0 in FAME18:1 were increased, the liquidus rapidly increased. This behavior represents the major difference between the acylglycerol/FAME and FAME-only mixtures. Note that the experimental data for the FAME16:0/FAME18:1 and MAG16:0/FAME18:1 mixtures included in this figure were taken from our previous studies (Imahara et al., 2006; Yoshidomi et al., 2017).

Fig. 2-11(b) summarizes the variations in the activity coefficient, γ_i^L, for each solute in FAME18:1. The γ_i^L for FAME16:0 was unity over the entire concentration range, indicating that the FAME16:0/FAME18:1 mixtures were ideal liquid solutions based on the high affinity of the components for one another. Thus, the gradual increase observed in the liquidus with changes in composition was the result of the tendency of the FAME16:0 to dissolve in the FAME18:1. In contrast, the γ_i^L values for MAG16:0 were much larger than 1 and exceeded 10 at low mole fractions. In the NSS model (Equations (2-14) and (2-15)), a large γ_i^L has the effect of effectively increasing the mole fraction, x_i, meaning that the liquidus temperature increases rapidly with increasing x_i. This occurs because highly polar MAGs have low affinity for FAMEs so that the former are not readily soluble in the latter.

In contrast to MAG16:0, the γ_i^L values determined for TAG16:0 were slightly less than 1, indicating high affinity with the FAMEs as a result of a lack of hydroxyl groups and relatively low polarity. In this case, the rapid increase in the liquidus temperature with changes in composition is ascribed to the high enthalpy of fusion of the TAG, as can be seen from Table 2-2. Specifically, TAGs having the same fatty acid moieties as MAGs

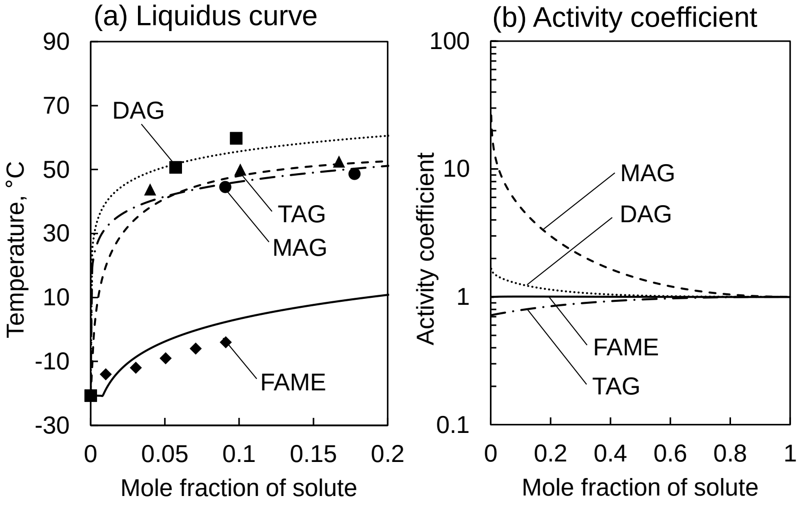

Fig. 2-11. Comparisons of (a) liquidus curves and (b) activity coefficients obtained using the UNIFAC (Dortmund) method for FAME16:0, MAG16:0, DAG16:0 and TAG16:0 (as the solutes) in FAME18:1 (as the solvent). The data for FAME16:0/FAME18:1 and MAG16:0/FAME18:1 was taken from previous studies (Imahara et al., 2006; Yoshidomi et al., 2017, respectively).

will exhibit enthalpies of fusion that are 4–5 times higher, as a consequence of the high molecular weights of the former (King & Garner, 1936). Equations (2-14) and (2-15) shows that a high value of enthalpy, $\Delta H_{m,i}$, has the effect of increasing the liquidus temperature, and therefore the rapid increase in the liquidus temperatures of the TAG/FAME mixtures can be attributed to the high molecular weights of the TAGs. The behavior of the DAGs was intermediate between those of the MAGs and TAGs. Because of their low affinity for FAMEs and moderately high molecular weights, the DAGs showed steep liquidus curves similar to those produced by the MAG and TAG samples.

Overall, the above results indicate that all acylglycerols will tend to precipitate in FAMEs, even at low concentrations. However, the impact of MAGs is likely to be the most significant because these compounds are generally present at higher concentrations in actual biodiesel as compared with DAGs and TAGs.

2.3.4 Multicomponent mixtures

Table 2-3 summarizes the experimental and calculated liquidus temperatures of multicomponent mixtures of acylglycerols and FAMEs as determined using the NSS model. These mixtures were prepared with high acylglycerol contents because the endothermic DSC peak was too small to be detected when the acylglycerol contents were too low. Although the acylglycerol proportions in these specimens were much higher than those in actual biodiesel, these higher ratios were necessary to investigate the validity of the NSS model.

For the majority of the mixtures, the differences between the measured and calculated values were less than 1 °C, indicating that the NSS model was able to accurately predict the liquidus temperatures, even for multicomponent systems. Slightly larger deviations were identified in the case of certain mixtures (such as samples 2, 8, and 10), but these variations were not considered significant. The reason for these discrepancies is not clear but, as discussed, the effect of compound formation (that is mixed crystals) between the acylglycerols and FAMEs or between the acylglycerols may have been responsible in some cases. In our previous study, the deviations of the NSS model results from experimental data tended to be larger for mixtures containing two different MAGs (Yoshidomi et al., 2017). Table 2-3 contains data for mixtures

Table 2-3. Experimental liquidus temperatures for multi-component mixtures together with values predicted using the NSS model.

Sample no.	Composition (mole %)											Liquidus temperature (°C)		
	FAME		MAG			DAG			TAGs			Experiment	Prediction	Absolute deviation
	16:0	18:1	16:0	18:0	18:1	16:0	18:0	18:1	12:0	16:0	18:0			
1	35.4	32.9	-	-	-	17.0	14.8	-	-	-	-	65.6	65.0	0.6
2	38.1	35.4	-	-	-	-	12.6	13.9	-	-	-	65.6	63.9	1.7
3	32.2	29.9	-	-	24.2	-	13.8	-	-	-	-	64.9	63.7	1.2
4	35.4	31.4	11.9	-	18.2	-	-	3.2	-	-	-	32.4	31.9	0.5
5	25.2	22.4	23.3	-	22.8	1.3	-	5.00	-	-	-	41.2	40.0	1.2
6	34.6	32.2	-	-	-	-	-	-	33.2	-	-	38.8	38.3	0.5
7	39.8	37.0	-	-	-	-	-	-	-	12.4	10.7	59.5	60.9	1.4
8	34.2	31.6	24.5	-	-	-	-	-	-	9.6	-	51.7	54.9	3.2
9	27.5	25.6	-	-	39.7	-	-	-	-	-	7.1	61.1	61.9	0.8
10	34.0	31.6	-	14.9	-	-	-	10.6	8.9	-	-	51.0	52.4	1.4
11	34.1	31.7	-	-	17.4	-	-	8.5	8.3	-	-	29.4	29.3	0.1
12	32.9	30.6	13.6	-	10.8	7.3	-	-	-	4.8	-	51.5	51.9	0.4

incorporating two different MAGs, DAGs or TAGs, although the deviations from the experimental values are not as large as in our previous study.

These multicomponent mixtures were not formulated with any specific design in mind, except for those having higher acylglycerol contents, and the NSS model worked well when assessing these essentially random compositions. However, it remains unclear how effective the simple NSS model would be when applied to a wider range of compositions.

2.4 Conclusions

DSC analyses of binary acylglycerol/FAME mixtures showed that the acylglycerols significantly raised the liquidus temperatures. Based on thermodynamic effects, MAGs tended to precipitate from mixtures with FAMEs because their hydroxyl groups produced low affinity with these compounds. In contrast, TAGs precipitated as a result of their high enthalpies of fusion, which in turn were derived from their high molecular weights. Both these effects promoted the precipitation of DAGs. The NSS model, which assumes a simple eutectic system, explained the shapes of the liquidus curves obtained for the majority of the acylglycerol/FAME mixtures. Therefore, these mixtures were evidently eutectic with some exceptions. The UNIFAC (Dortmund) method was also found to be a viable means of estimating the activity coefficients of the mixtures. The NSS model was determined to be applicable to multicomponent systems composed of acylglycerols and FAMEs and accurately predicted liquidus temperatures. However, some deviations from the experimental values were found for certain mixtures. The possibility of compound formation between different types of acylglycerols should be studied more carefully so that this model can be applied to the study of real-world biodiesel blends.

Chapter 3 Interactions between Different Monoacylglycerols during Solidification

3.1 Introduction

The presence of minor components affects the cold flow properties considerably. MAGs are intermediate compounds produced during transesterification and are typical minor components in biodiesel. The European standard restricts the total amount of MAGs to below 0.8 wt.% (Committee for Standardization Automatic Fuels, 2008). MAGs occasionally solidify even at around room temperature because their melting points are high (Tang et al., 2008; Chupka et al., 2011; Chupka et al., 2014).

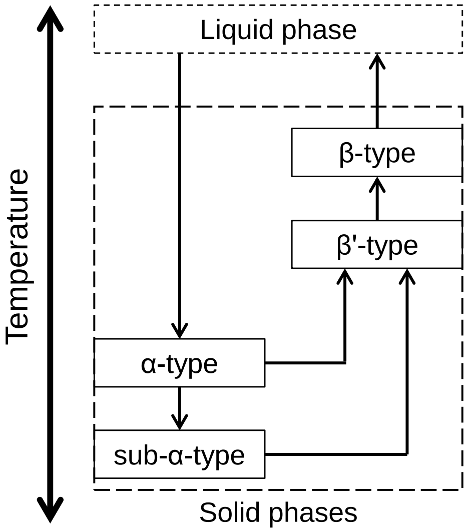

Fig. 3-1. Polymorphism of MAGs and the melting point of each crystal form

Fig. 3-1 shows the polymorphism behavior of MAGs (Maruyama et al., 1971). MAGs have various crystalline structures, called α, β′, and β types, and each has a different melting point in the following order, α < β′ < β (Fischer et al., 1920; Malkin and Shurbagy, 1936). In general, α-type crystals form first when a melt of MAG is cooled until the phase transition occurs. The α crystals are converted irreversibly to the β′ type and then to the β type after specific transition times (Maruyama et al., 1973). The potential presence of several polymorphs makes the solidification behavior of MAGs complicated. Chupka et al. studied the effects of MAGs on biodiesel cold flow properties and highlighted the importance of MAG polymorphism (Chupka et al., 2011; Chupka et al., 2014).

Our research group previously studied a thermodynamic model for calculating the solid–liquid equilibria of surrogate biodiesel fuels containing MAGs (Yoshidomi et al., 2017; Sugami et al., 2017). A binary mixture of a MAG and a FAME was found to behave as a non-ideal liquid solution because of the large difference between the chemical structures of the components, and the non-ideality is well described by a modified version of the universal quasi-chemical functional-group activity coefficients (UNIFAC) model, known as the UNIFAC (Dortmund) model (Gmehling et al., 1993). When the mixture contains only one type of MAG, the predicted values are in excellent agreement with the experimental results. However, deviations arise when the mixture includes two different MAGs (Yoshidomi et al., 2017; Sugami et al., 2017). The researchers hypothesized that this discrepancy is caused by co-crystallization (solid solution) of the different MAGs, because the previous model assumed that the solid phase consists of a single component. Lutton and Jackson (1967) and Maruyama et al. (1978) have reported the formation of such solid solutions of different MAGs under certain conditions.

This chapter aims to investigate the interactions between MAGs and develop an appropriate thermodynamic model for describing the solidification behaviors of MAGs. The model obtained was then applied to multi-component mixtures, which contained two types of MAGs in FAMEs and served as surrogate biodiesel fuels. The results of this study will help to establish a prediction model for real biodiesel, which contains several types of MAGs.

3.2 Experimental procedures

3.2.1 Materials

The MAG samples used were 1-monolaurin (MAG12:0, purity 99%, Tokyo Chemical Industry, Tokyo, Japan), 1-monopalmitin (MAG16:0, 99%, Olbracht Serdary Research Laboratories (OSRL), Toronto, Canada), and 1-monostearin (MAG18:0, 99%, OSRL). The FAME samples were methyl laurate (FAME12:0, 99%), methyl palmitate (FAME16:0, 99.5%), and methyl oleate (FAME18:1, 99%), which were all purchased from Sigma-Aldrich Japan, Tokyo. Test samples for DSC were prepared by blending these chemicals in various ratios, without purification.

3.2.2 Analytical methods

For DSC analyses, samples (about 10 mg) were placed in non-hermetic aluminum-based pans under a dry nitrogen flow (50 mL/min). Indium and zinc were used for temperature calibration and α-alumina was used as a reference material. The liquidus temperature for each sample was determined from the obtained DSC profile. Because MAGs are polymorphic, two different methods were used for examining α- and β-type crystals.

For α-type crystals, each sample was heated until fully melted and cooled until the first exothermic peak was detected; the solid phase formed at this time is thought to consist of α-type crystals (Maruyama et al., 1973; Yoshidomi et al., 2017). The sample was then reheated immediately at a heating rate of 3 °C/min and the DSC profile was recorded. This rapid heating prevents the crystal transition to the β′ or β type during analysis. For β-type crystals, each solidified sample was held in a thermostatic chamber at 50 °C for four weeks to ensure the transition to the β type, which is the most stable structure. The reported times for transition to the β type are about 0.1, 100, and 230 h at 50 °C for MAG12:0, MAG16:0, and MAG18:0, respectively (Maruyama et al., 1971); four weeks (672 h) is therefore considered to be sufficient. After removal from the chamber, the sample was exposed at room temperature for a few minutes, and then DSC was performed at a heating rate of 1 °C/min.

For each pure MAG, the melting point was estimated from the onset temperature of the endothermic peak in the DSC profile. In the case of a binary or multi-component mixture, the highest endothermic peak maximum temperature was defined as the experimental liquidus temperature, as in previous studies (Maruyama et al., 1971; Knothe and Dunn, 2009; Yoshidomi et al., 2017). Note that this is a rough estimate because the absolute liquidus temperature is generally difficult to determine, especially for multi-component systems.

3.2.3 Prediction models

Three thermodynamic models were used to calculate the liquidus temperatures. The first two models were based on the expression of solid–liquid equilibrium below.

$$\ln\frac{\gamma_i{}^L x_i}{\gamma_i{}^S z_i} = \frac{\Delta H_{m,i}}{RT_{m,i}}\left[1-\frac{T_{m,i}}{T}\right] \tag{3-1}$$

Several assumptions were applied to Equation (3-1) to develop non-solid-solution (NSS) and solid solution (SS) models. The description of these models can be found in Section 2.2.2.

The third model, called the compound formation (CF) model, was derived from the reaction equilibrium. The CF model assumes that the solidification of MAGs is similar to a chemical reaction. When v_1 moles of C_1 and v_2 moles of C_2 in a liquid phase produce a solid compound C_S, the reaction is expressed as follows:

$$v_1 C_1(\text{liquid}) + v_2 C_2(\text{liquid}) \leftrightarrow C_s(\text{solid}) \qquad (3\text{-}2)$$

The reaction equilibrium constant K_a is described by:

$$K_a = \frac{(\gamma_1{}^{\mathrm{L}} x_1)^{v_1} (\gamma_2{}^{\mathrm{L}} x_2)^{v_2}}{(z)^1} = (\gamma_1 x_1)^{v_1} (\gamma_2 x_2)^{v_2} \qquad (3\text{-}3)$$

where γ_i^{L} and x_i are the activity coefficient and mole fraction of component C_i in the liquid phase, respectively. The term z is the mole fraction of compound C_S in the solid phase, but because no other solid is present in the system, it can be assumed to be unity. However, there is another expression for the equilibrium constant K_a, which is derived from the Gibbs–Helmholtz equation (Prausnitz et al., 1999):

$$K_a = K_{\text{ref}} \times \exp \frac{\Delta H_{\text{ref}}}{R T_{\text{ref}}} \left(\frac{T - T_{\text{ref}}}{T} \right) \qquad (3\text{-}4)$$

where K_{ref} and ΔH_{ref} are the equilibrium constant and enthalpy of reaction, respectively, at an arbitrarily chosen reference temperature T_{ref}. By combining Equations (3-1) and (3-4), we can determine the liquidus temperature T. The detailed calculation procedure will be described in the following section. It should be noted that v_1 and v_2 can be used as fitting parameters in this model. The γ_i^{L} terms were estimated by using the UNIFAC (Dortmund) model. The calculations were conducted using programs coded with Microsoft Visual Basic for Applications on Excel (Microsoft Corp., Redmond, WA, USA).

3.3 Results and discussion

3.3.1 Pure component properties

All three thermodynamic models involve pure component properties: the melting point T_m and enthalpy of fusion ΔH_m. Therefore, these properties were determined by DSC for each pure MAG and all crystalline forms; the results are shown in Table 3-1. The values obtained were consistent with those previously reported (Lutton, 1971;

Maruyama et al., 1971; Yoshidomi et al., 2017); therefore, these values were used for performing calculations with equations (3), (4), and (7). The numbers of functional groups in each MAG are also shown in Table 3-1; they were used to estimate the activity coefficients γ_i^{L} with the UNIFAC (Dortmund) model.

3.3.2 Binary MAG behaviors

The liquidus temperatures of α- and β-type crystals were analyzed by DSC. Fig. 3-2 shows DSC profiles of the mixture of MAG16:0 and MAG18:0 for both α- and β-types. Upon heating, the heat flow starts to change at a certain tempearture, and the DSC profile shows an obvious valley; it indicates a phase transition from solid to liquid. Thus, the liquidus temperature was determined from the peak temperature of the valley. Furthermore, the same sample showed different liquidus temperatures after being treated by different methods; for example, the mixture with x_1 (MAG18:0) of 0.28 had a liquidus temperature of 66.5 °C (Fig. 3-2 (a)) and 70.7 °C (Fig. 3-2 (b)) for α-type and β-type, respectively, suggesting that the crystal transition from α to β-type has occurred during the treatment.

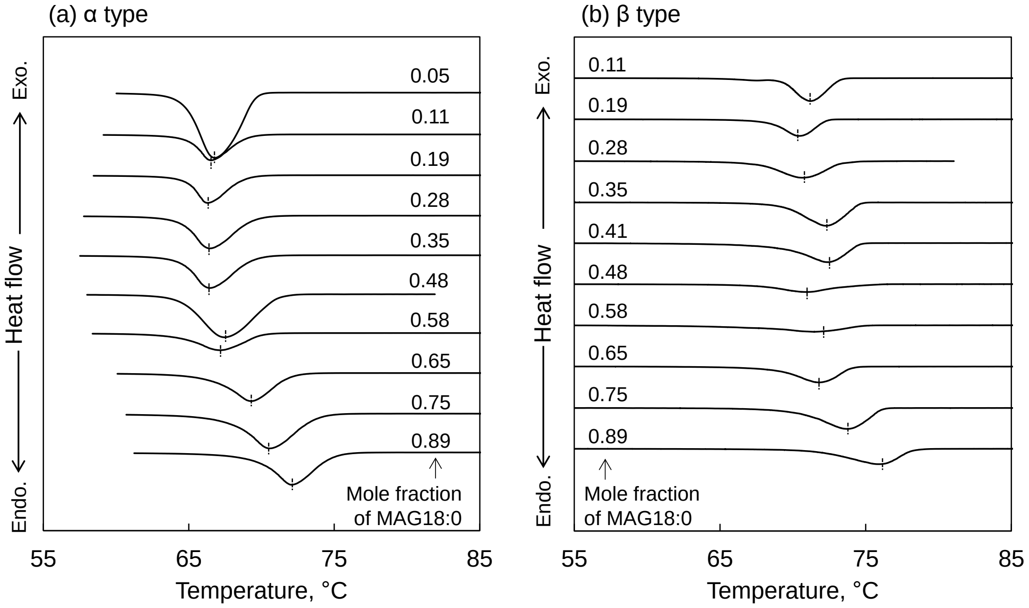

Fig. 3-2. DSC profiles of binary mixtures MAG16:0/MAG18:0 for (a) α-type and (b) β-type crystals.

Table 3-1. Thermodynamic properties of monoglycerides used for calculation

Component and type of crystal		Melting point, °C	Enthalpy of fusion, kJ/mol	Number of UNIFAC functional group					
				CH_3	CH_2	CH	OH(p)	OH(s)	CH_2COO
MAG12:0	α	44.4	22.4	1	11	1	1	1	1
(1-monolaurin)	β	62.1	47.5						
MAG16:0	α	64.9	34.4	1	15	1	1	1	1
(1-monopalmitin)	β	72.8	67.1						
MAG18:0	α	71.6	35.1	1	12	1	1	1	1
(1-monostearin)	β	78.9	75.2						

The liquidus temperatures of α- and β-type crystals are shown by solid circles in Figs. 3-3 and 3-4, respectively, for various binary mixtures of MAGs. We can obtain the liquidus curves of the binary MAGs by connecting these points. The experimental liquidus curves have complex shapes, although our research group previously reported (Yoshidomi et al., 2017) that binary mixtures of MAG and FAME give simple, smooth curves. This implies that the solidification behaviors of MAG/MAG and MAG/FAME mixtures are different. The three thermodynamic models described in the previous section were used to obtain theoretical liquidus curves and compared them with the experimental curves.

Fig. 3-3 shows that the behavior of the α-type crystals depends on the pair of MAGs. In the case of the MAG12:0/MAG18:0 mixture (Fig. 3-3 (a)), because of the difference between the carbon chain lengths ($\Delta C = 6$), the experimental liquidus temperatures are close to those obtained with the non-solid-solution model. In contrast, the MAG16:0/MAG18:0 pair (Fig. 3-3 (c); $\Delta C = 2$) conforms to the solid-solution model. These results suggest that a large difference between the carbon chain lengths leads to independent solidification of the individual MAGs, whereas similar MAGs can form a solid solution. Such a tendency was reported by Maruyama et al. for binary systems of MAGs (Maruyama et al., 1978). The behavior of the MAG12:0/MAG16:0 pair (Fig. 3-3 (b); $\Delta C = 4$) is intermediate between those indicated by the two models.

Fig. 3-4 shows that for β-type crystals, the experimental liquidus curves are close to those obtained with the non-solid-solution model for all pairs, although there are some deviations. The reason for the difference between the behaviors of the α and β crystals remains unclear, but it could arise because of differences among the crystal transition rates of the MAGs. In general, a MAG with a shorter carbon chain has a shorter transition time (Maruyama et al., 1971), therefore MAGs with shorter chains will independently change to the β form earlier than the those with longer chains and the solid solution will be disrupted during the crystal transition.

The results obtained with the two models based on the solid–liquid equilibrium do not fit the complex shapes of the liquidus curves well. The experimental curves have irregularities, with multiple upward convex lines. Therefore, the compound formation model, which is derived from the reaction equilibrium, was used. The results obtained

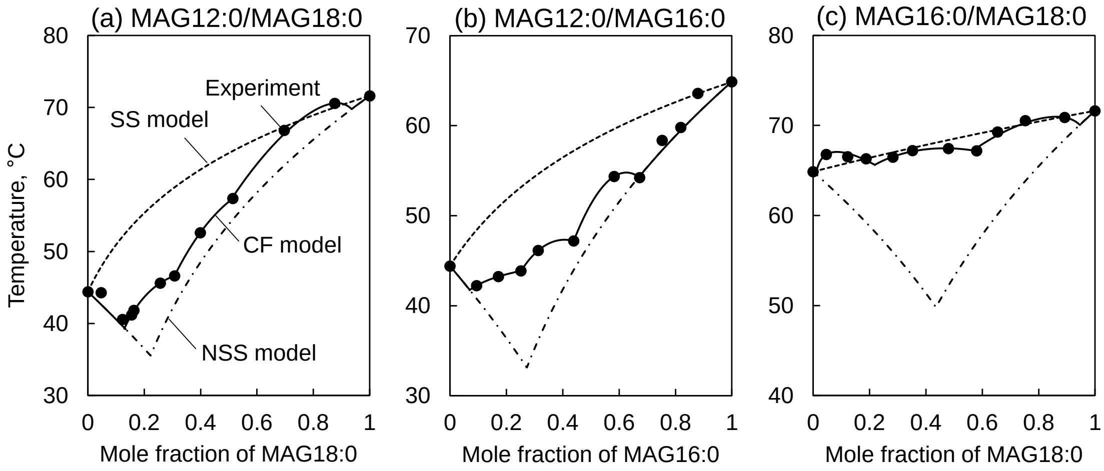

Fig. 3-3. Experimental liquidus temperatures for various binary mixtures of α-type MAGs and theoretical curves obtained by using the non-solid-solution, solid-solution, and compound formation models.

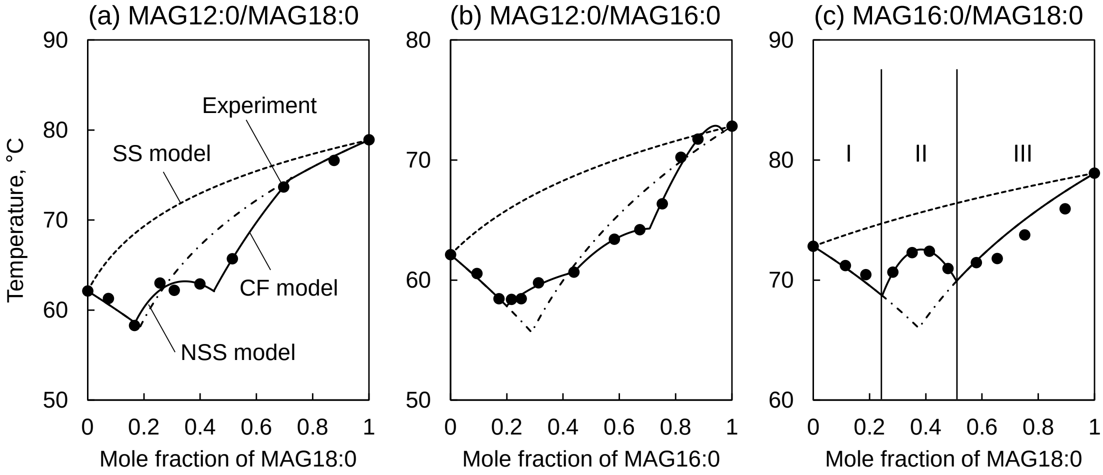

Fig. 3-4. Experimental liquidus temperatures for various binary mixtures of β-type MAGs and theoretical curves obtained by using non-solid-solution, solid-solution, and compound formation models.

with this model are shown by solid lines in Figs. 3-3 and 3-4. These results clearly fit the experimental liquidus curves well.

Fig. 3-4 (c) can be used to explain the fitting procedure as the simplest case. First, the experimental liquidus curve was divided into three regions (I, II, and III). In regions I and III, the compound formation model exactly matches the non-solid-solution model. This means that only MAG16:0 solidifies in region I ($v_1 = 1$, $v_2 = 0$) and only MAG18:0 solidifies in region III ($v_1 = 0$, $v_2 = 1$). On the basis of this assumption, the reaction equilibrium constant K_a for each region is $\gamma_1 x_1$ (region I) or $\gamma_2 x_2$ (region III), from Equation (3-3). If the melting point $T_{m,i}$ of the MAG is chosen as the reference temperature T_{ref}, the compound formation model, via Equations (3-3) and (3-4), becomes identical to Equation (2-14) or (2-15) for the non-solid-solution model, i.e., the compound formation model includes the non-solid-solution model as a special case.

The upward convex curve in region II is thought to indicate compound formation between MAG16:0 and MAG18:0. For the calculation with Equation (3-4), the highest temperature in the given region was chosen as T_{ref}. The stoichiometric numbers v_1 and v_2 were used as fitting parameters and determined by the least-squares method. The ΔH_{ref} term was estimated as the average of the fusion enthalpies weighted by the stoichiometric numbers, as follows:

$$\Delta H_{\mathrm{ref}} = \frac{v_1 \Delta H_{m,1} + v_2 \Delta H_{m,2}}{v_1 + v_2} \tag{3-8}$$

When $v_1 = 3.63$ and $v_2 = 2.25$, the calculated curve fits the experimental plots well, as shown in Fig. 3-4 (c). For all cases in Figs. 3-3 and 3-4, the number of upward convex lines was counted to divide the curves into regions, and then fitting was performed independently for each region in the same way. The obtained parameters are summarized in Table 3-2. Although it is not certain whether or not the obtained stoichiometric numbers reflect the real world, it can be said that the compound formation model can describe the complex solidification behaviors of MAGs.

Compound formation in MAG mixtures is thought to occur because of the presence of hydroxyl groups, which are involved in hydrogen bonding between MAGs. Such strong intermolecular interactions allow easy formation of associated molecules, which can be distinguished by X-ray diffraction (Etter, 1990). Such compound-forming systems have also been reported for triglyceride mixtures (Engström, 1992).

3.3.3 Multi-component mixtures

The compound formation model was applied to surrogate biodiesel fuels, namely multi-component mixtures that consisted of MAGs and FAMEs. A pair of MAGs (1:1 by weight) was added to a mixture of FAME12:0, FAME16:0, and FAME18:1 (65:24:11 by weight) at various MAG contents. The liquidus temperatures of the mixtures were determined by DSC, via two methods; the results are shown in Fig. 3-5 by open and solid circles, respectively. The samples with MAG contents higher than 2 wt.% were used because at low contents the MAG endothermic peaks in the DSC curves were too weak. Although such high MAG contents are rather far from those in real biodiesel, these experiments were performed to investigate the potential of the model.

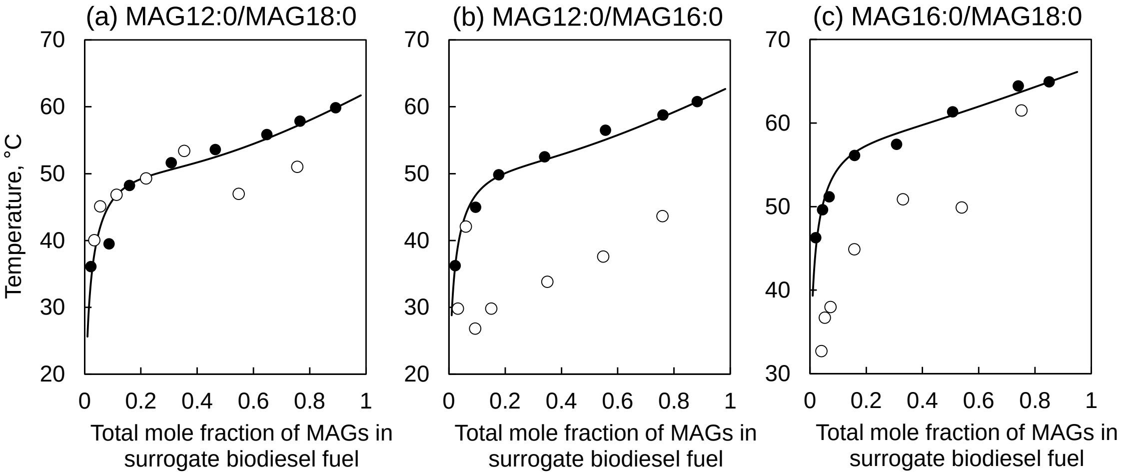

Fig. 3-5. Experimental liquidus temperatures for surrogate biodiesel fuels determined by the method used for α-type MAGs (open circles) and modified method (solid circles), along with theoretical curves obtained by using compound formation model (solid lines)

First, the liquidus temperatures were determined, as shown by open circles in Fig. 3-5, by using the method described in the subsection of analytical method for α-type MAGs, in which the sample was immediately reheated after the first exothermic peak was detected on cooling. However, sudden changes in the liquidus temperature can be observed, especially in Fig. 3-5 (a). This could be caused by the crystal transition from α to β′ or β, because the transition time tends to become shorter in the presence of a solvent. FAMEs can act as a solvent in this case; therefore, the MAGs sometimes change to the β′

or β type. Determination of the liquidus temperature for α-type MAGs in multi-component mixtures is therefore difficult.

Therefore, the DSC method was modified, and the sample was examined after transition by allowing an adequate transition time. For this purpose, the sample was cooled to −20 °C and then DSC was performed at a heating rate of 3 °C/min. The liquidus temperatures obtained by this method are shown as solid circles in Fig. 3-5. In contrast to the previous results, the liquidus temperatures give monotonous curves. This method enabled us to obtain consistent liquidus curves for β′- or β-type MAGs, although the crystal type was not specified in this study.

For calculations using the compound formation model, T_{ref} was set at the highest liquidus point among the experimental data. Although the type of crystal was not identified, the enthalpies of fusion for the β type shown in Table 3-1 were used as tentative values for the calculation. The crystal type is not critical for testing the applicability of the model. The parameters v_1 and v_2 were determined by data fitting to be 0.00 and 1.19 for (a), 0.00 and 1.27 for (b), and 0.00 and 0.87 for (c), in Fig. 3-5. The fitting results, which are represented by solid lines, show that the compound formation model works well for predicting the experimental liquidus curves. However, the values of v_1 and v_2 obtained by the model will not always reflect the actual stoichiometric numbers of the solid compounds, because these are just the results of data fittings.

The excellent matching of the compound formation model with the experimental data is not surprising because the model has fitting parameters. The compound formation model is, therefore, an empirical model. In a previous series of studies (Imahara et al., 2006; Yoshidomi et al., 2017; Sugami et al., 2017), our ultimate purpose was to establish a non-empirical formula for predicting the behaviors of any biodiesel and blends with fossil diesel. The current study shows the complexity of MAGs, even in the case of simple binary mixtures. Although the complex liquidus curves were successfully described by using the compound formation model, the parameters obtained will be useless for other cases because the parameters will change if a different chemical component is used.

If the ratio of MAGs is fixed, as in Fig. 3-5, the compound formation model can be used to predict biodiesel cold flow properties. This means that we can develop a formula for predicting the cold flow properties of biodiesels derived from a feedstock as a function of the MAG content by data fitting, as in Fig. 3-5, because the fatty acid composition is almost the same for a given type of feedstock.

3.4 Conclusions

The liquidus temperatures of binary systems of MAGs were determined by DSC to investigate their interactions. Three thermodynamic models were applied to the obtained results. The difference between the MAG carbon chain lengths (ΔC) affected the liquidus curve shape for α-type crystals. When ΔC was large (ΔC = 6), the liquidus curves were close to those obtained with the non-solid-solution model, in which different MAGs solidify independently. When ΔC was small (ΔC = 2), the liquidus curve corresponded to the solid-solution model, in which different MAGs form a continuous solid solution.

These two models based on the solid–liquid equilibrium did not exactly fit the complicated liquidus curves of binary MAGs. Only the compound formation model, which is derived from the reaction equilibrium, can describe the complicated behaviors of binary MAGs. This implies that the different MAGs form a solid compound via intermolecular hydrogen bonding. It was therefore concluded that the compound formation model is appropriate for describing the solidification behaviors of MAGs.

The suitability of the compound formation model was tested for predicting the behaviors of surrogate diesel fuels that consisted of multi-component mixtures of MAGs and FAMEs. The results show that the model represents the liquidus curves well. However, the compound formation model involves fitting parameters, which need to be determined from experimental data. The parameters will change depending on the chemical composition; therefore, obtaining general predictions that apply to all cases is difficult. This model only works for biodiesel from known feedstocks. In Chapter 5, the compound formation model will be applied to actual biodiesel fuels derived from various plant oils and for establishing a prediction formula for each feedstock.

Chapter 4 Interactions between the Same and Different Types of Acylglycerols on Solidification

4.1 Introduction

Acylglycerols (MAG, DAG, and TAG) are intermediate compounds in biodiesel production by transesterification of plant oils. Such acylglycerols, especially those bonded to saturated fatty acids, deteriorate the cold flow properties of biodiesel owing to their high melting points and ready solidification in biodiesel (Tang, De Guzman, et al., 2008; Yu et al., 1998). In addition, the polymorphs of acylglycerols also affect cold flow properties (Chupka et al., 2011; Sugami et al., 2017; Yoshidomi et al., 2017). Chupka et al. and Yoshidomi et al. reported that MAGs solidify as metastable α-form crystals in biodiesel when cooled rapidly, but transform into the β-form during slow heating or long-term storage (Chupka et al., 2011; Yoshidomi et al., 2017). Furthermore, biodiesel precipitation can occur even at temperatures above the cloud point (Paryanto et al., 2019; Sugami et al., 2017), as the MAG melting point differs depending on its crystal form. The prediction of such complex solidification behavior is essential for biodiesel use.

The effect of MAGs on biodiesel cold flow properties was investigated by using differential scanning calorimetry (DSC) in the previous study. As compound formation behavior has often been observed in binary MAG/MAG mixtures, confirming whether the same behavior occurs in binary mixtures of other combinations is of interest. TAG/TAG mixtures have been extensively studied and reported to not tend to produce molecular compounds (Timms, 1984), with some exceptions (Zhang et al., 2018). However, studies on other combinations, such as DAG/DAG, DAG/MAG, TAG/MAG, and DAG/TAG, are limited. In this chapter, DSC analysis was performed on binary mixtures of acylglycerols mixed in the above combinations to determine whether the components solidify separately or form molecular compounds. Three thermodynamic models were used for prediction and compared with the experimental results to aid this discussion.

4.2 Analytical procedures

4.2.1 Materials and experimental method

High-purity MAG, DAG, and TAG samples in Table 4-1 were purchased and used as received without purification. These acylglycerols were mixed in various combinations and ratios to prepare binary mixtures.

Table 4-1. Pure materials used in this study and their supplier-guaranteed purities.

Name	Abbreviations	Manufacturer	Purity, % (GC)
1-Monolaurin	MAG12:0	Nu-Chek Prep, Inc., Elysian, MI	99
1-Monopalmitin	MAG16:0	Olbracht Serdary Research Laboratories, Toronto, Canada	99
1-Monostearin	MAG18:0		99
1-Monoolein	MAG18:1	Nu-Chek Prep, Inc., Elysian, MI	99
1,3-Dilaurin	DAG12:0		99
1,3-Dipalmitin	DAG16:0		99
1,3-Distearin	DAG18:0		99
1,3-Diolein	DAG18:1	Larodan Fine Chemicals AB, Solna, Sweden	99
Tripalmitin	TAG16:0	Olbracht Serdary Research Laboratories, Toronto, Canada	99
Tristearin	TAG18:0		99

DSC (DSC-60, Shimadzu Corp., Kyoto, Japan) analysis was performed to evaluate liquidus and solidus temperatures (liquidus > solidus) of the binary mixtures. A mixture becomes completely liquid above the liquidus and fully solid below the solidus. The liquidus is particularly essential for cold flow properties because a slight solid phase can even form slightly below the liquidus to clog fuel filters.

For each DSC analysis, approximately 10 mg of the sample was placed in an aluminum-based crimping cell and exposed to a dry nitrogen flow (50 mL/min). The sample was heated until fully melted and then cooled rapidly (-10 °C/min) until the first exothermic peak had ended. The sample was then heated immediately (10 °C/min) and the DSC profile was recorded. This rapid heating was intended to prevent the crystal transition of acylglycerols during analysis. The liquidus temperature was determined from the peak temperature of the highest endothermic peak, while the solidus was determined from that of the lowest endothermic peak if observed. The enthalpy of liquidus and solidus peak was determined from the peak area of the corresponding peak. Overlapped peaks were separated by assuming a Gaussian function using Origin 8.4 (OriginLab Co., Northampton, MA, USA).

Each pure material was also measured in the same manner to determine thermal properties. The melting point and enthalpy of fusion were determined from the onset temperature and peak area of the endothermic peak, respectively, and used to calculate thermodynamic models.

For DSC analysis, indium and zinc were used for temperature calibration of the instrument, and α-alumina was used as the reference material during experiments. DSC analysis was conducted three times for each sample, and the mean values were reported.

4.2.2 Thermodynamic models

(1) Solid-liquid equilibrium

The theory of solid-liquid equilibrium was used to develop two thermodynamic models: NSS and SS models. The detailed description and application of the models can be found in section 2.2.2.

(2) Reaction equilibrium

The CF model was based on the reaction equilibrium upon the assumption that two kinds of acylglycerols from the molecular compound and solidify. The detailed application of this model was described in Chapter 3 for binary mixtures of MAGs.

4.3 Results and discussion

4.3.1 Pure component properties

The thermal properties of the pure materials used in this chapter were evaluated, as shown in Table 4-2, and used to calculate the thermodynamic models. Experimental uncertainties in triplicate measurements were within –0.8 to +1.3 °C of the mean melting point and –2.0% to +1.1% of the mean enthalpy of fusion. Metastable α crystal data were

Table 4-2. Thermal properties of pure materials determined by DSC (10 °C/min) and the number of UNIFAC functional groups.

Component	Crystal type	Number of UNIFAC functional groups							Melting point (°C)	Enthalpy of fusion (kJ mol^{-1})
		CH$_3$	CH$_2$	CH	CH=CH	OH(p)	OH(s)	CH$_2$COO		
MAG12:0	α	1	11	1	-	1	1	1	44.8	22.4
MAG16:0	α	1	15	1	-	1	1	1	66.4	34.1
MAG18:0	α	1	17	1	-	1	1	1	74.2	39.2
MAG18:1	β	1	15	1	1	1	1	1	35.0	49.4
DAG12:0	β$_1$	2	20	1	-	1	-	2	56.7	79.2
DAG16:0	β$_1$	2	28	1	-	1	-	2	73.4	111.4
DAG18:0	β$_1$	2	32	1	-	1	-	2	79.6	130.0
DAG18:1	β$_1$	2	28	1	2	1	-	2	25.8	88.4
TAG16:0	β	3	41	1	-	-	-	3	63.3	132.4
TAG18:0	β	3	47	1	-	-	-	3	73.8	181.1

used for MAGs because liquidus temperatures attributed to α-type MAGs were observed under the given DSC conditions. Stable β_1 and β crystal data were used for DAGs and TAGs, respectively, because these materials underwent crystal transition rapidly during DSC measurement, even at the fast-heating rate of 10 °C/min. This behavior was demonstrated in the previous chapter. As an exception, β crystal data was used for MAG18:1 owing to the fast transition of unsaturated MAG, similar to DAGs and TAGs.

4.3.2 DSC profiles of binary mixtures

The binary mixtures exhibited some typical behaviors in DSC analysis, with examples shown in Fig. 4-1. When the melting point difference between the two components was large, which was the most common case in this study, a single endothermic peak was observed, as shown in Fig. 4-1(a) (DAG18:0/DAG18:1). This peak corresponded to the liquidus temperature of the mixture, which shifted gradually to a higher temperature as the DAG18:0 fraction increased. The solidus peak was usually not observed in this case because, as mentioned in the experimental section, the mixture was reheated immediately after the first exothermic peak was passed in the cooling cycle, preventing the mixture from fully solidifying.

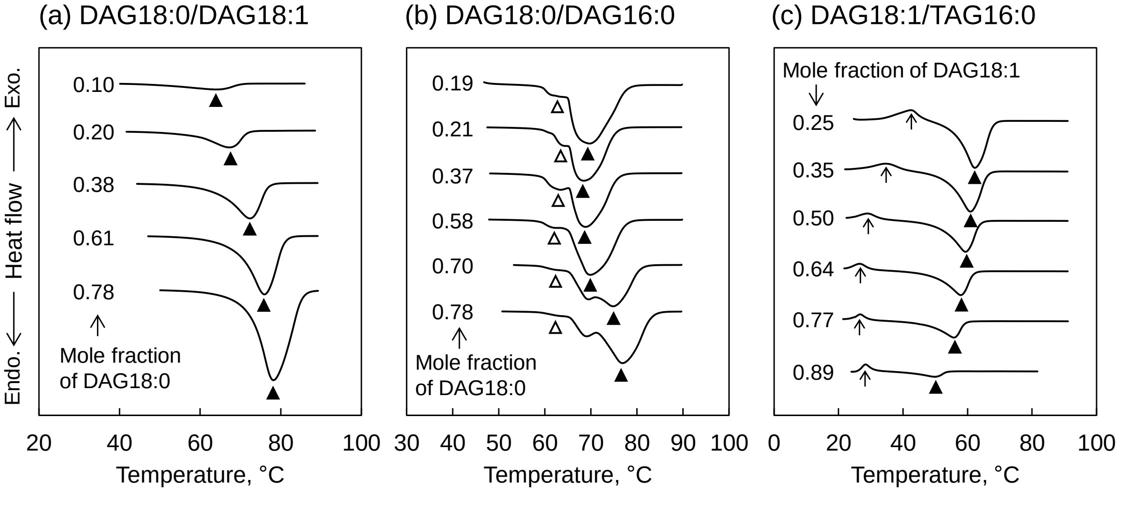

Fig. 4-1. DSC profiles at a heating rate of 10 °C/min for mixtures of (a) DAG18:0/DAG18:1, (b) DAG18:0/DAG16:0, and (c) DAG18:1/TAG16:0 at various mole fractions.

When the melting point difference was small, multiple endothermic peaks were observed, as shown in Fig. 4-1(b) (DAG18:0/DAG16:0). This might be due to the mixture fully solidifying in the cooling cycle, resulting in multiple melting processes appearing in the DSC profile. In this case, the highest (filled triangles) and lowest (open triangles) endothermic peak temperatures were assigned as the liquidus and solidus temperatures of the mixture, respectively.

When TAG was a component in the mixture and solidified during the cooling cycle, as shown in Fig. 4-1(c) (DAG18:1/TAG16:0), a small exothermic peak (indicated by arrows) was observed in addition to the liquidus endothermic peak (filled triangles). This exothermic peak might be due to the rapid melt-mediated crystal transition from α to β-type TAG upon heating (Sato & Kuroda, 1987).

4.3.3 Binary mixtures of the same type of acylglycerol

This section covers binary mixtures of the same type of acylglycerol, namely, TAG/TAG, DAG/DAG, and MAG/MAG. As TAG/TAG and MAG/MAG pairs have been studied by us and other researchers, as mentioned later, the current study focused on DAG/DAG mixtures, with the results shown in Fig. 4-2. In triplicate trials, the experimental uncertainties were within –0.6 to +0.7 °C of the mean for liquidus, and –0.5 to +0.6 °C of the mean for solidus. Enthalpy analysis was also conducted for all mixtures, and the results are shown in Fig. 4-3.

For the DAG18:0/DAG12:0 mixture, the experimentally determined liquidus increased monotonically with increasing DAG18:0 content, as shown in Fig. 4-2(a). Owing to the relatively large difference between the melting points of DAG18:0 and DAG12:0, no significant difference was observed between the NSS and SS models, such that the experimental liquidus fitted both models well. However, the measured solidus was almost constant at around 56 °C, regardless of the mole fraction, suggesting the eutectic point. The enthalpy analysis (Fig. 4-3 (a)) shows a linear trend of enthalpies of both liquidus and solidus. As this is also a typical characteristic of eutectic systems, the actual behavior of this mixture is considered to follow the NSS model more closely.

The experimental liquidus of DAG18:0/DAG16:0, as shown in Fig. 4-2(b), was closer to the NSS model than the SS model. The experimental liquidus tended to be slightly lower than the NSS model, especially at the composition near to 50:50 ratio. Since

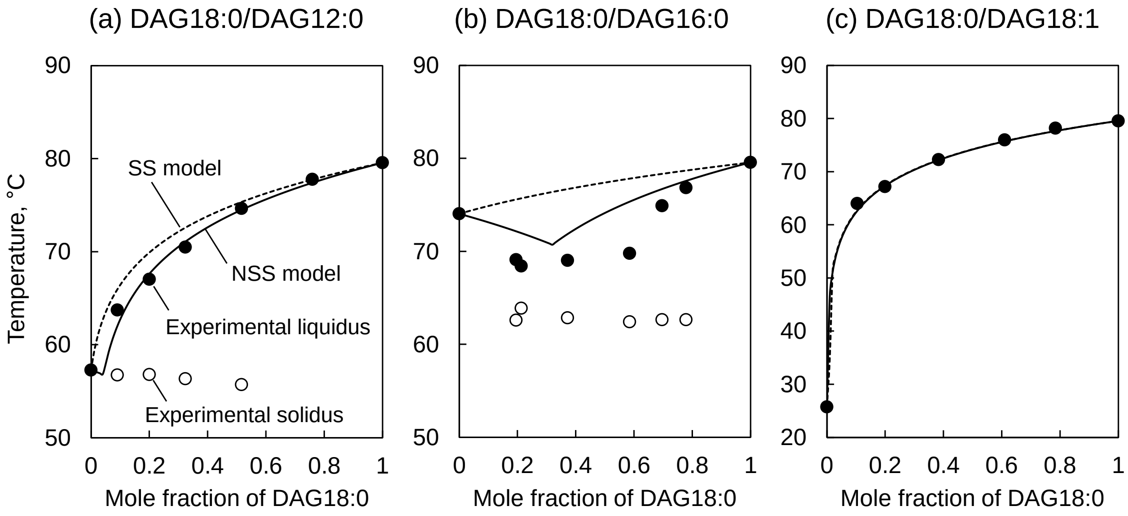

Fig. 4-2. Experimentally determined liquidus (filled circles) and solidus (open circles) temperatures of various DAG/DAG binary mixtures, and theoretical liquidus curves calculated using the NSS (solid line) and SS (dashed line) models.

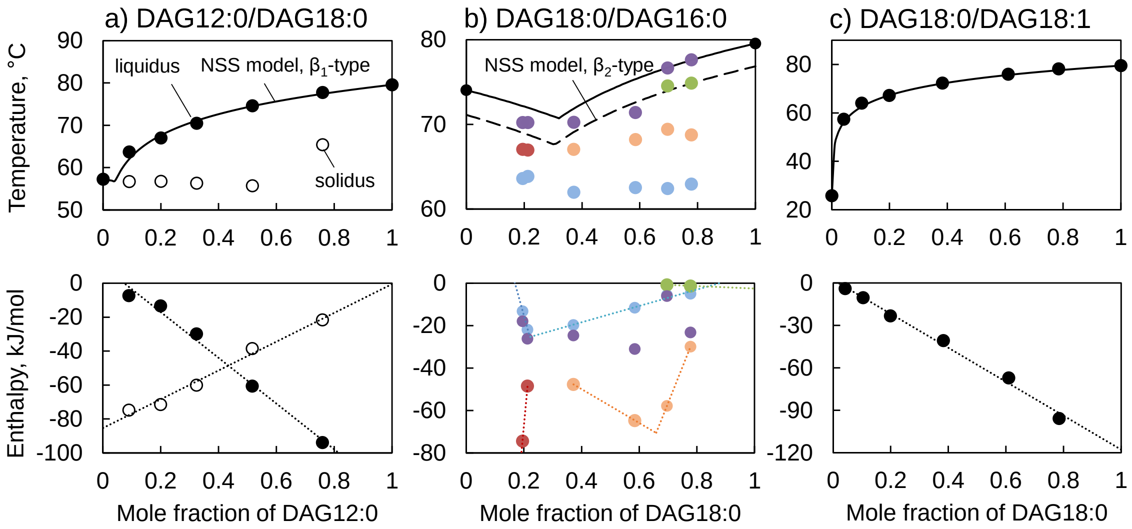

Fig. 4-3. Phase diagram (top) and enthalpy diagram (bottom) of DAG/DAG mixtures. The black and white symbols indicated experimentally determined temperature, while the colored symbols were obtained by peak separation from experimental results.

DSC profiles of this mixture (Fig. 4-1(b)) showed multiple peaks, peak separation was conducted, and the results are shown in Fig. 4-3(b). Below the liquidus temperature (purple circles), peaks at around 63 °C (blue circles) and 68 °C (red and orange circles) are found in all samples. In addition, transition temperatures around 75 °C (green circles) coincide with the predicted curve by the NSS model for β_2-type DAG. This suggests that the crystal transition from β_2 to β_1-type was incomplete, leading to several solid phase transitions. The enthalpy diagrams also suggest such solid phase transitions, as the enthalpy corresponding to each transition temperature has a typical linear trend. Therefore, the difference between the experimental liquidus and the NSS model (solid curve) is because the crystal formed at DAG18:0 ratio below 0.7 was β_2 instead of the assumed β_1. It should be noted that both forms have very close melting points (1-3 °C), so the deviation between the experimental results and predicted values was insignificant.

For the DAG18:0/DAG18:1 mixture, the experimental liquidus was in good agreement with both models, as shown in Fig. 4-2(c). As the NSS and SS models almost overlapped due to the very large melting point difference, and no solidus was observed in this case, it was difficult to determine which model was correct for the real behavior. However, the enthalpy analysis (Fig. 4-3(c)) indicates the behavior of a typical eutectic system. Therefore, DAG/DAG mixtures can generally be predicted using the NSS model. The same has also been shown for some diacid DAGs (Craven & Lencki, 2011a) and DAG16:0/DAG18:1 mixtures (Xu & Dong, 2017).

For TAG/TAG mixtures, a review by Timms concluded that eutectic behavior is most commonly observed (Timms, 1984), implying that TAG/TAG mixtures can generally be represented by the NSS model, in addition to DAG/DAG mixtures. As some exceptions, specific TAG/TAG combinations can form molecular compounds at certain compositions (Timms, 1984; Zhang et al., 2018). For example, Engström reported that 2-oleo-1,3-distearin (StOSt) and 1-oleo-2,3-distearin (OStSt) form a molecular compound with a composition of approx. 1:1 (Engström, 1992). However, such cases are special, and since the TAG content in biodiesel is generally smaller than that of MAG, the effect of TAG/TAG compound formation on biodiesel cold flow properties is considered limited.

Meanwhile, all MAG/MAG mixtures studied in the previous chapter had complex liquidus curves, represented only by the CF model, suggesting the formation of molecular compounds between different types of MAG. Compared with TAG/TAG and DAG/DAG mixtures, MAG/MAG seems to form molecular compounds readily owing to the presence of two hydroxyl groups in the MAG molecule, which form strong intermolecular hydrogen bonding with carbonyl groups of another MAG molecule (Holmgren et al., 1988).

4.3.4 Binary mixtures of different types of acylglycerol

The solid–liquid phase behaviors and enthalpy analysis results of binary DAG/MAG, TAG/MAG, and DAG/TAG mixtures are shown in Figs. 4-3 and 4-4, Figs. 4-5 and 4-6, and Figs 4-7 and 4-8, respectively. The experimental uncertainties in triplicate trials were within −0.9 to +0.8 °C (liquidus) and −0.9 to +0.7 °C (solidus) of the means in Fig. 4-3, −0.6 to +0.9 °C (liquidus) in Fig. 4-5, and −0.6 to +0.7 °C (liquidus) in Fig. 4-7.

Among the DAG/MAG mixtures, the experimental liquidus temperatures for DAG12:0/MAG12:0 (Fig. 4-3(a)), DAG18:0/MAG18:0 (Fig. 4-3(b)), and DAG18:0/MAG18:1 (Fig. 4-3(c)) were clearly on the V-shape curve, in good agreement with values calculated by the NSS model. Solidus temperatures were also observed in these mixtures, with no significant change observed with different compositions. Enthalpy analysis of solidus in DAG12:0/MAG12:0 (Fig. 4-4(a)) showed a minimum at 0.18 ratio of DAG12:0, suggesting the presence of a eutectic point. These behaviors were typical of eutectic systems.

The behavior of DAG18:0/MAG18:1, as shown in Fig. 4-3(d), was similar to that shown in Fig. 4-2(c), and the experimental liquidus values were well explained by the NSS model, despite the large difference in melting points making distinguishing between the NSS and SS models difficult. Furthermore, the enthalpy analysis for the liquidus (Fig. 4-4(b)) shows a linear tendency, suggesting the behavior of a typical eutectic system, which favors the use of the NSS model.

As shown in Fig. 4-3(e), the DAG18:1/MAG16:0 mixture was an exception. In the region where the DAG18:1 fraction was more than 0.6, the experimental liquidus deviated to a higher temperature than the NSS model. The presence of solidus at different temperatures (around 42 °C and 26 °C) suggests the possibility of two different eutectic systems in this mixture. The enthalpy analysis in Fig 4-4(c) also shows a linear tendency for each solidus temperature as commonly observed in a eutectic system. These behaviors

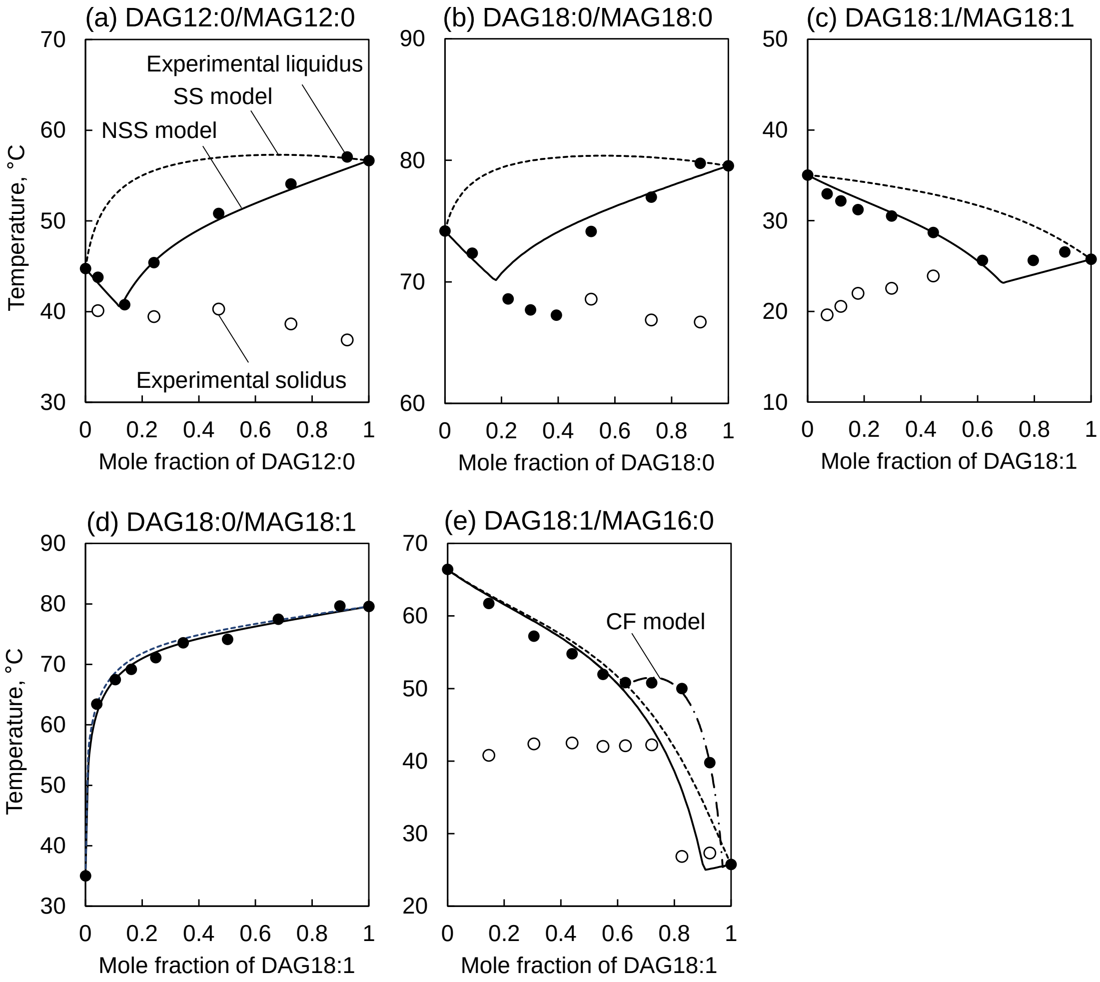

Fig. 4-4. Experimentally determined liquidus and solidus temperatures of various DAG/MAG binary mixtures, and theoretical liquidus curves calculated from thermodynamic models.

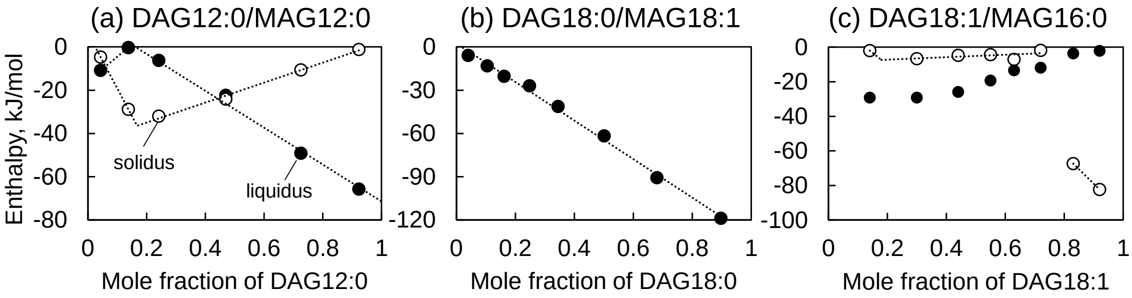

Fig. 4-5. Enthalpy diagram of a) DAG12:0/MAG12:0, b) DAG18:0/MAG18:1, and c) DAG18:1/MAG16:0 mixtures.

suggest a molecular compound formation, which can be reasonably explained by the CF model. However, even if compound formation occurs when the DAG fraction is high, its effect on the cold flow properties of actual biodiesel (generally, MAG content > DAG content) might not be significant. The NSS model seems to be sufficient for predicting the solidification behavior of biodiesel.

For the TAG/MAG mixtures, the experimental liquidus temperatures were on the V-shape curve for TAG18:0/MAG18:0 (small melting point difference; Fig. 4-6(a)), and monotonically increased for TAG18:0/MAG12:0 (Fig. 4-6(b)) and TAG16:0/MAG18:1 (large melting point differences; Fig. 4-6(c)), with no sign of compound formation. Fig. 4-6 shows a linear decrease in liquidus enthalpy of two cases with small and large melting

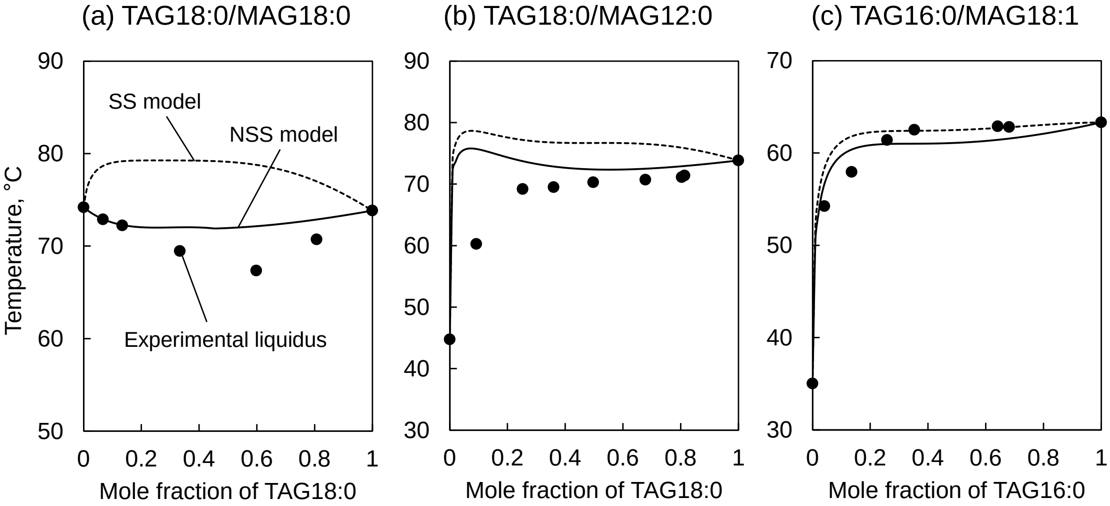

Fig. 4-6. Experimentally determined liquidus temperatures of various TAG/MAG binary mixtures, and theoretical liquidus curves calculated using the NSS and SS models.

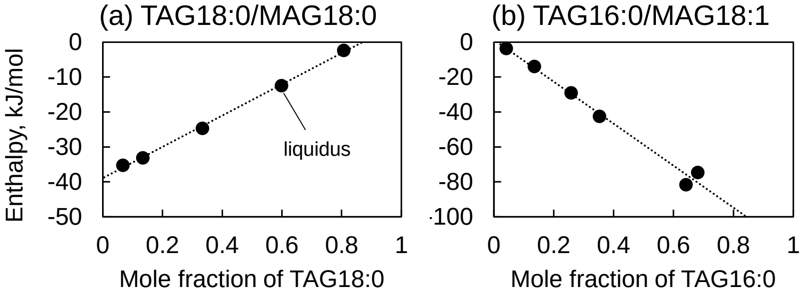

Fig. 4-7. Enthalpy diagrams of a) TAG18:0/MAG18:0 and b) TAG16:0/18:1

point differences. These results indicate that the TAG/MAG mixtures are also essentially eutectic, which should be explained by the NSS model, similar to DAG/MAG mixtures. However, deviations between the NSS model and experimental values were observed, especially in the low TAG content region of Fig. 4-6(b). When the difference in fatty acid chain length between TAG and MAG was large, the UNIFAC (Dortmund) model tended to estimate a very large activity coefficient ($\gamma_i{}^L$) at low TAG contents. For example, in Fig. 4-6(b), the $\gamma_i{}^L$ value was about 60 when the TAG18:0 fraction was 0.01, resulting in a higher predicted liquidus temperature. The reason for this is unclear, but UNIFAC (Dortmund) might not be able to sufficiently evaluate large and complex molecules such as TAG.

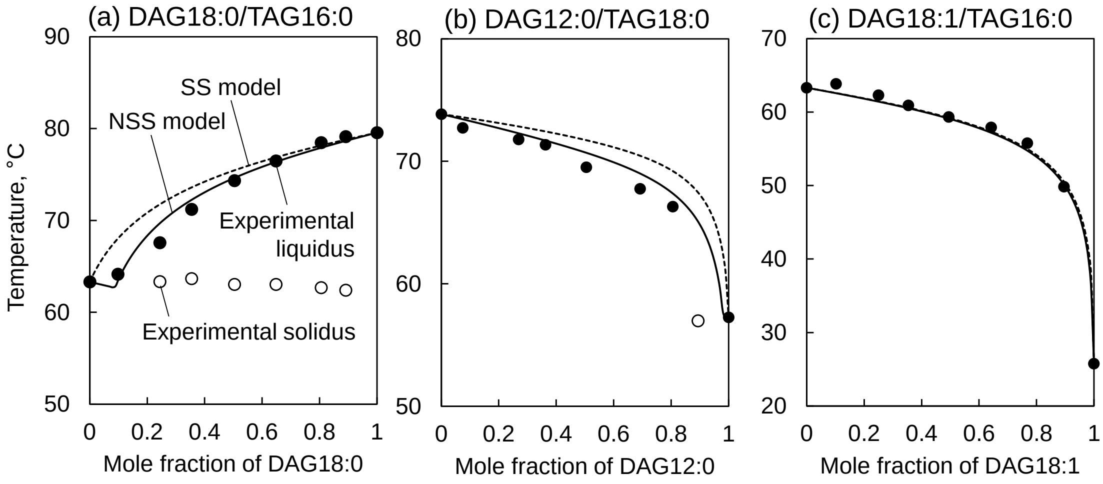

Fig. 4-8. Experimentally determined liquidus temperatures of various DAG/TAG binary mixtures, and theoretical liquidus curves calculated using the NSS and SS models.

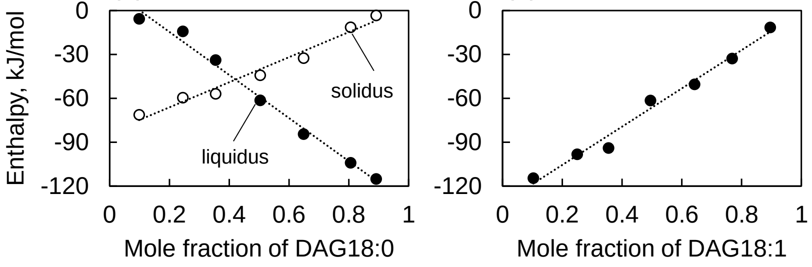

Fig. 4-9. Enthalpy diagrams of a) DAG18:0/TAG16:0 and b) DAG18:1/TAG16:0

For the DAG/TAG mixtures in Fig. 4-8, the experimental liquidus shows a slight V-shaped trend or monotonic change. The enthalpy analysis in Fig. 4-9 also indicates a typical linear decrease in liquidus enthalpy and increase in solidus enthalpy, allowing explanation by the eutectic system, similar to other mixtures. This resulted in a relatively good agreement between the experimental liquidus and the NSS model. However, as shown in Fig. 4-5(b), when the difference in fatty acid chain length between TAG and DAG was large, the NSS model results tended to be higher than the experimental results in the low TAG content region (high DAG content). This was also due to the ${\gamma_i}^L$ value being quite large (${\gamma_i}^L$ = 2.5 when TAG18:0 fraction was 0.01), but not noticeable compared with that of Fig. 4-6(b). The evaluation of activity coefficients by UNIFAC (Dortmund) appears able to express the experimental results quite well for TAG/DAG mixtures.

4.4 Conclusions

This study showed that the liquidus temperatures of DAG/DAG mixtures either follow a simple V-shape curve or change monotonically, both of which fit well with values predicted by the NSS model. The formation of molecular compounds between different types of DAG was not observed. According to previous studies, such eutectic behavior has also been commonly observed in TAG/TAG mixtures. Similarly, the liquidus curves of binary mixtures of different types of acylglycerol, namely, DAG/MAG, TAG/MAG, and DAG/TAG, were in good agreement with the NSS model, with a few exceptions. However, when TAG was included in the mixture, concerns remained regarding the reliability of the UNIFAC (Dortmund) model for estimating the activity coefficient. These results implied that each component solidified independently as a pure substance in the above mixtures. This contrasted with the results of our previous study on MAG/MAG mixtures, whose liquidus curves were very complex, showing a strong tendency to form molecular compounds described only by the CF model. As the MAG content in biodiesel is generally higher than that of DAG and TAG, and MAG is less likely to form molecular compounds with TAG and DAG, it can be assumed that the effect of DAG and TAG on biodiesel cold flow properties is limited. Therefore, to accurately predict the biodiesel cold flow properties, understanding the behavior of MAG, especially its molecular compound formation, is probably important.

Chapter 5 Prediction of Liquidus Temperatures of Actual Biodiesel Samples

5.1 Introduction

In the mixtures of FAMEs and MAGs, MAGs exhibited high activity coefficients due to their two hydroxyl groups and were prone to precipitation from FAMEs. The liquidus temperatures of mixtures of FAMEs with no or one type of MAG could be predicted accurately by the non-solid-solution (NSS) model, a thermodynamic model based on the hypothesis that one solid phase consists of a single substance (Yoshidomi et al., 2017). However, for the mixtures containing two types of MAGs, the liquidus temperature deviated from the NSS model. This deviation was thought to be due to the different MAGs forming molecular compounds and solidifying. In such cases, the compound formation (CF) model predicted the liquidus temperature correctly. Since actual biodiesel contains several types of MAGs, the CF model is expected to work properly instead of the NSS model.

Therefore, this study aimed to demonstrate the CF model for actual biodiesel samples containing MAGs in various concentrations. The liquidus temperature was experimentally determined by differential scanning calorimetry (DSC) or visual observation in a glass cell. The performance of the CF model in predicting the liquidus temperature was compared with the simple NSS model.

5.2 Methodology

5.2.1 Materials

Actual biodiesel samples were prepared from refined coconut, palm, and rapeseed oils, purchased from Nacalai Tesque, Inc., Kyoto, Japan, by an alkaline-catalyzed method (Meher et al., 2006). From each feedstock, three biodiesel samples with different acylglycerol contents were prepared under different reaction conditions, as summarized in Table 5-1. The fatty acid composition of each feedstock determined from the FAME content is shown in Table 5-2.

Table 5-1. Contents of FAMEs and acylglycerols in biodiesel samples prepared from various plant oils (wt.%).

Components	Coconut methyl esters (CME)			Palm methyl esters (PME)			Rapeseed methyl esters (RME)		
Name	CME1	CME2	CME3	PME1	PME2	PME3	RME1	RME2	RME3
Total FAMEs	99.47	99.13	97.85	99.80	99.56	98.31	99.75	98.64	96.54
Total MAGs	0.53	0.87	1.20	0.20	0.44	0.56	0.25	0.53	0.67
Total DAGs	-	-	0.47	-	-	0.30	-	0.45	0.32
Total TAGs	-	-	0.47	-	-	0.83	-	0.38	2.48

Table 5-2. Fatty acid compositions (wt.%) of biodiesel samples determined from the FAME contents.

Fatty acid moeities	CME	PME	RME
Caprylic (8:0)	4.7	-	-
Capric (10:0)	4.2	-	-
Lauric (12:0)	43.9	-	-
Myristic (14:0)	19.7	0.7	-
Palmitic (16:0)	11.5	41.9	3.5
Stearic (18:0)	5.1	8.9	6.7
Oleic (18:1)	8.3	33.8	54.4
Linoleic (18:2)	1.5	13.6	21.6
Linolenic (18:3)	-	-	9.8
Others	-	0.3	2.4

Table 5-3. Pure components used to prepare biodiesel surrogates.

Component	Abbreviation	Manufacturer	Purity, %
Methyl caprate	FAME10:0	MP Biomedicals LLC, Solon, Ohio.	99
Methyl laurate	FAME12:0	Sigma-Aldrich Japan, Tokyo, Japan	99.5
Methyl myristate	FAME14:0		99
Methyl palmitate	FAME16:0		99
Methyl stearate	FAME18:0	Nacalai Tesque Inc., Kyoto, Japan	99.5
Methyl oleate	FAME18:1	Sigma-Aldrich Japan, Tokyo, Japan	99
Methyl linoleate	FAME18:2		99
1-Monocaprin	MAG10:0	Olbracht Serdary Research Laboratories, Toronto, Canada	99
1-Monolaurin	MAG12:0	Nu-Chek Prep, Inc., Elysian, Minnesota	99
1-Monopalmitin	MAG16:0	Olbracht Serdary Research Laboratories, Toronto, Canada	99
1-Monostearin	MAG18:0		99
1-Monoolein	MAG18:1		99
1,3-Dipalmitin	DAG16:0	Olbracht Serdary Research Laboratories, Toronto, Canada	99
1,3-Distearin	DAG18:0		99
1,3-Diolein	DAG18:1	Larodan Fine Chemicals AB, Solna, Sweden	99

Table 5-4. Composition of FAMEs, MAGs, and DAGs mixtures (wt.%) for preparing surrogate biodiesel samples that simulate the composition of CME, PME, and RME.

Fatty acid moieties	FAMEs			MAGs			DAGs
	CME	PME	RME	CME	PME	RME	PME
Caprin (10:0)	9.0	-	-	9.2	-	-	-
Laurin (12:0)	43.9	-	-	43.9	-	-	-
Myristin (14:0)	20.4	0.8	-	21.2	0.8	-	-
Palmitin (16:0)	11.5	44.0	3.5	9.2	44.1	3.5	45.4
Stearin (18:0)	5.3	8.9	2.6	6.5	8.6	2.5	7.8
Olein (18:1)	8.3	36.1	59.8	10.0	46.6	94.0	46.8
Linolein (18:2)	1.6	10.3	34.1	-	-	-	-

High purity FAMEs, MAGs, and DAGs shown in Table 5-3 were purchased and blended for preparing biodiesel surrogates to study the wide range of acylglycerol contents beyond the actual biodiesel samples. As shown in Table 5-4, the mixtures of FAMEs and MAGs were prepared separately to simulate the fatty acid compositions of plant oils in Table 5-2. However, due to the commercial unavailability of high purity reagents, the fractions of FAME8:0 and FAME18:3 were incorporated into FAME10:0 and FAME18:2, respectively. MAG8:0 and unsaturated MAGs were also replaced with MAG10:0 and MAG18:1, respectively. These substitutions may not affect the solidification behavior very much because the melting points of these substances are much lower than the others. The FAMEs and MAGs mixtures were then combined in various ratios to prepare biodiesel surrogates with various MAG contents. The mixture of DAGs was prepared only for PME surrogates and mixed with the mixtures of FAMEs and MAGs to investigate the effect of DAGs.

5.2.2 Analytical method

DSC (DSC-60, Shimadzu Co., Kyoto, Japan) analysis was performed to determine the liquidus temperature. Approximately 10 mg of the sample was placed in an open aluminum pan and exposed to dry nitrogen flow (50 ml/min). The sample was heated 20 degrees above the highest melting point among the sample's components to be completely melted and held for 3 min. Three different conditions were then applied as follows:

Condition 1: The melted sample was cooled until the end of the first exothermic peak, which means that the solid phase had formed, then reheated immediately, and the DSC profile was recorded.

Condition 2: The melted sample was cooled 20 degrees below the lowest exothermic peak to be fully solidified, then reheated to record the DSC profile.

Condition 3: The melted sample was cooled until the formation of precipitates was visually observed and stored at room temperature for 24 h. The sample was then cooled 20 degrees below the lowest exothermic peak as in condition 2 and reheated to record the DSC profile.

These conditions considered the transition of MAG polymorphs, and the difference will be discussed later. The heating and cooling rates were ± 10 °C/min. The liquidus temperature was determined from the peak top temperature of the highest endothermic peak (Yoshidomi et al., 2017).

For the samples with low MAGs content (< 1.2 wt.%), the liquidus temperature was determined by visual observation, as detailed in our previous study (Yoshidomi et al., 2017), since the endothermic peaks of MAGs were too weak to determine the liquidus by DSC. Approximately 6 g of the sample was placed in a glass cell apparatus with a magnetic stirrer and wholly melted at 100 °C. Using a heat medium jacket covering the glass cell, the sample was slowly cooled (-1 °C/min) with agitation until the first solid precipitated and held at that temperature for 5 min. It was then slowly reheated (1 °C/min) with agitation, and the temperature at which the solid completely disappeared was determined as the liquidus temperature. The DSC and visual observation were repeated three times for each sample and condition, and the mean values were reported.

Gas chromatography (GC, GC-2014, Shimadzu Co.) and high-performance liquid chromatography (HPLC, Prominence, Shimadzu Co.) were performed to determine FAMEs and acylglycerols contents in biodiesel samples under the following conditions: GC; column, Select Biodiesel (Agilent Technologies, Inc., CA., USA); oven temperature, 50 °C (1 min hold) – 180 °C (15 °C/min) – 230 °C (7 °C/min) – 380 °C (10 °C/min, 5 min hold); carrier gas, helium; detector, flame ionization detector. HPLC; column, Cadenza CD-C18 (Imtakt Co., Kyoto, Japan); oven temperature, 40 °C; eluent, methanol (1 mL/min); detector, refractive index detector. In addition, solid precipitates were isolated from the samples by washing with n-hexane on a suction filter and analyzed by X-ray diffraction (XRD, RINT-2200-V, Rigaku Corp., Tokyo, Japan).

5.2.3 Thermodynamic models

Two thermodynamic models, namely the non-solid-solution (NSS) and compound formation (CF) models, were used to calculate the liquidus temperature. Detailed applications of these models were demonstrated in previous chapters. First, Equation (5-1) is derived from the theory of solid-liquid equilibrium:

$$\frac{\gamma_i{}^{\mathrm{L}} x_i}{\gamma_i{}^{\mathrm{S}} z_i} = \exp\left(\frac{\Delta H_{m,i}}{R T_{m,i}} \frac{T - T_{m,i}}{T}\right) \tag{5-1}$$

where x_i and z_i are the liquid and solid mole fractions of component i, respectively. The $\gamma_i{}^{\mathrm{L}}$ and $\gamma_i{}^{\mathrm{S}}$ are activity coefficients of component i in liquid and solid phases, representing deviations from the ideal liquid and solid solutions, respectively. Eq.1 can calculate the solid-liquid equilibrium of the mixture from the melting point ($T_{m,i}$) and enthalpy of fusion ($\Delta H_{m,i}$) of each component i. The NSS model assumed that one solid phase consists of one component, meaning that different components are immiscible in a solid phase and solidify independently. On this assumption, since the solid phase fraction $z_i = 1$ (and thus $\gamma_i = 1$), Equation (5-1) is modified as follows:

$$T = \frac{T_{m,i}}{1-\frac{RT_{m,i}}{\Delta H_{m,i}}\ln \gamma_i{}^L x_i} \tag{5-2}$$

where the liquidus temperature (T) is expressed as a function of x_i. Equation (5-2) gives a T value for each component i, and the highest one among the components is the liquidus temperature of the mixture, at which the corresponding component i solidifies. The previous chapters revealed that binary mixtures of FAME/FAME and MAG/FAME followed this NSS model.

However, binary mixtures of MAG/MAG showed more complex behaviors and fitted with the CF model, suggesting the formation of molecular compounds. When v_1 moles of component C_1 and v_2 moles of C_2 in liquid phase produce one mole of solid compound C_S, this reaction is expressed as Equation (5-3).

$$v_1 C_1(\mathrm{L}) + v_2 C_2(\mathrm{L}) \leftrightarrow C_S(\mathrm{S}) \tag{5-3}$$

Considering the relationship between the reaction equilibrium constant and the Gibbs-Helmholtz equation for this reaction, the following CF model can be obtained (Prausnitz et al., 1999)pr:

$$(\gamma_1{}^L x_1)^{v_1}(\gamma_2{}^L x_2)^{v_2} = K_{\mathrm{ref}} \exp\left(\frac{\Delta H_{\mathrm{ref}}}{RT_{\mathrm{ref}}}\frac{T-T_{\mathrm{ref}}}{T}\right) \tag{5-4}$$

where K_{ref} and ΔH_{ref} are the reaction equilibrium constant and reaction enthalpy at an arbitrarily chosen reference temperature T_{ref}. The ΔH_{ref} was substituted by the weighted average of enthalpies of fusion of two components as follows.

$$\Delta H_{\mathrm{ref}} = \frac{v_1 \Delta H_{m,1} + v_2 \Delta H_{m,2}}{v_1 + v_2} \tag{5-6}$$

In this model, v_1 and v_2 were used as fitting parameters and determined by the least-squares method. The highest experimental liquidus temperature in the fitting region was chosen as T_{ref}. When three or more components form the molecular compound, the left side of Equation (5-4) becomes $\prod(\gamma_i{}^L x_i)^{v_i}$. However, this study assumed that two MAGs having the first and second highest T in Equation (5-2) produce the molecular compound. Although such a hypothesis may not necessarily reflect the real world, this study focused on demonstrating whether or not the form of Equation (5-4) can represent the experimental results.

The $T_{m,i}$ and $\Delta H_{m,i}$ of each pure component used in the calculations are summarized in Table A1 as Appendix. The $\gamma_i{}^L$ was estimated based on the type and number of functional groups of the components, using a modified version of the universal quasi-chemical functional group activity coefficient method, known as the UNIFAC (Dortmund) (Gmehling et al., 1993). All calculations were performed using algorithms coded in Microsoft Visual Basic for Excel (Microsoft Corp., WA, USA).

5.3 Results and Discussion

5.3.1 Biodiesel surrogates

Fig. 5-1 shows the liquidus temperatures determined by DSC for biodiesel surrogates (mixtures of FAMEs and MAGs) that simulated coconut, palm, and rapeseed oil methyl esters (CME, PME, and RME surrogates, respectively) as the total MAG content was varied up to 100 wt.%. The predicted curves by the NSS model for α, β', and β-type MAGs are also depicted. Such high MAG contents are far from actual biodiesel, but this experiment was conducted to study the behavior of MAGs extensively. In triplicate trials for each data point, experimental uncertainties were within −1.5 to +0.7 ℃ of the mean for CME, −1.2 to +0.5 ℃ for PME, and −1.1 to +0.8 ℃ for RME surrogates.

The liquidus temperature tends to be higher in the order of DSC analysis conditions 1, 2, and 3. Condition 1 (squares) was intended to measure the liquidus temperatures of α-type MAGs by preventing the crystal transition via immediate and fast reheating, as demonstrated in previous study (Yoshidomi et al., 2017) for MAG/FAME binary mixtures. However, in the present study, the experimental results in Condition 1 are close to the calculated results for β'-type MAGs rather than α-type. It seems that the crystal transition of MAGs was faster in multicomponent systems and changed to β'-type even in Condition 1.

In Condition 2 (triangles), the sample was cooled to be fully solidified before reheating. Furthermore, in Condition 3 (circles), the sample was left at room temperature for 24 h before analysis. Thus, Conditions 2 and 3, especially the latter, were intended to give MAGs sufficient time for crystal transition. As for CME and PME surrogates, the liquidus temperature increases in Condition 2 compared to Condition 1, suggesting that the crystal transition of MAGs further progressed. However, the results in Condition 3 are almost unchanged from Condition 2, except in the regions of low MAG content less than 10 wt.%. In RME surrogates, the liquidus temperatures in Condition 2 are almost the same as in Condition 1 but increases in Condition 3. These results suggest that the liquidus temperature corresponding to the most stable β-type MAGs was measured by Condition 3. Note that even if the holding time at room temperature was extended to 330 h and 3,600 h under Condition 3, the liquidus temperature did not change in all cases, indicating that 24 h was sufficient to obtain the β-type MAG crystals. Actually, the experimental results of Condition 3 are closest to the prediction curves for β-type MAGs.

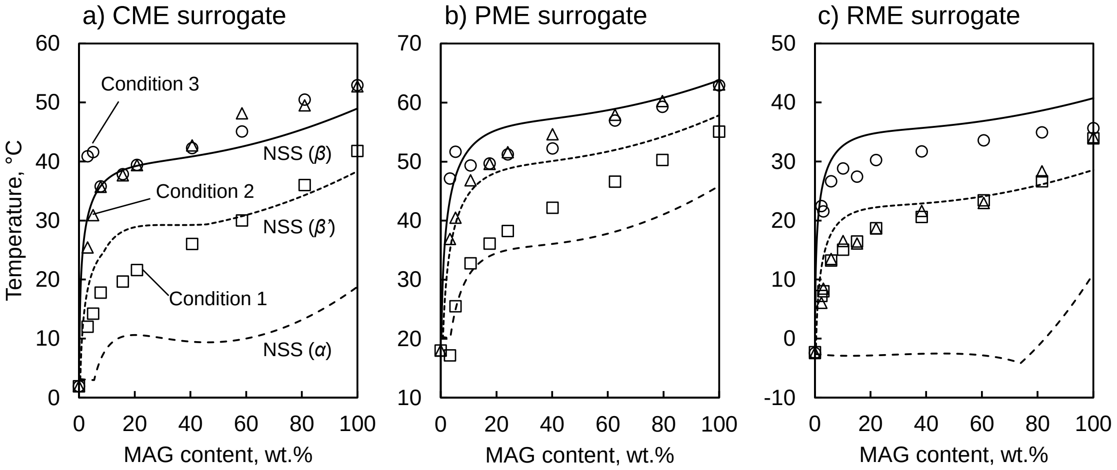

Fig. 5-1. Liquidus temperature of CME, PME, and RME surrogates measured by various conditions in DSC (symbols) and predicted by various MAG types of NSS model (lines).

To confirm this, X-ray diffraction (XRD, RINT-2200-V, Rigaku Corp., Tokyo, Japan) analysis of the crystals was performed. Similar to Condition 3, approximately 200 mg of the surrogate with 50 wt.% MAG content was fully melted in a glass vial and cooled until crystals formed. After 24 h at room temperature, the crystals were collected by washing with *n*-hexane on a suction filter and subjected to XRD analysis, with the results shown in Fig. 5-2. Considering the XRD patterns of pure MAG16:0 crystals, the α-type crystal is characterized by diffraction peaks around 20~22 degrees; the β' type shows distinct peaks at 15.5, 19.4, 21.3, 23.4, 25.3, and 27.1 degrees; the β type shows strong signals around 22-24 degrees in addition to the above β'-type peaks. The crystals from the

CME and PME surrogates present the characteristics close to the β-type diffraction pattern, and it is certain that the liquidus temperature determined by Condition 3 is attributed to the β-type MAGs. However, crystals obtained from the RME surrogate were easily melted at room temperature during preparation and could not be analyzed by XRD.

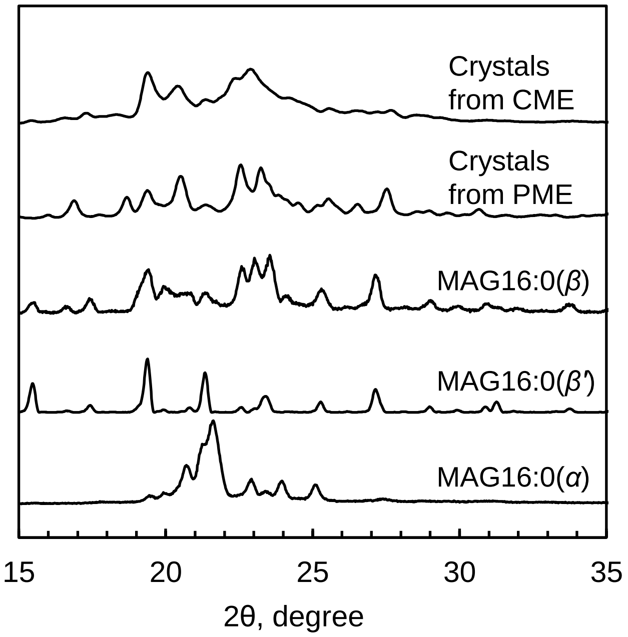

Fig. 5-2. XRD profiles of precipitate crystals from surrogate biodiesels compared to pure MAG16:0 at various forms.

Although the NSS model provided some indication, there are apparent deviations from the experimental results in Fig. 5-1. The deviations are within expectations as our previous study has suggested that the NSS model is not accurate for multicomponent mixtures containing multiple types of MAGs (Yoshidomi et al., 2017). Therefore, the CF model was applied to the data obtained under Condition 3, as shown in Fig. 5-3. The experimental liquidus temperature rises sharply when the MAG content increases from 0 wt.% in any case (CME, PME, and RME surrogates). However, the liquidus temperature drops slightly at about 10 wt.% and then slowly rises as the MAG content increases. The behavior seems to be different between high and low MAG content regions. Therefore, Fig. 5-3 shows two curves that were individually fitted to each region for CME and PME surrogates. For RME, the experimental values could be roughly expressed by only one curve because the difference between the low and high MAG regions was not so significant.

For fitting with the CF model, two MAGs forming the compound was assumed. Two MAGs with the first and second highest liquidus temperatures as estimated by Equation (5-2): MAG18:0 and MAG12:0 for CME, MAG16:0 and MAG18:0 for PME, and MAG18:0 and MAG 18:1 for RME surrogates, respectively.

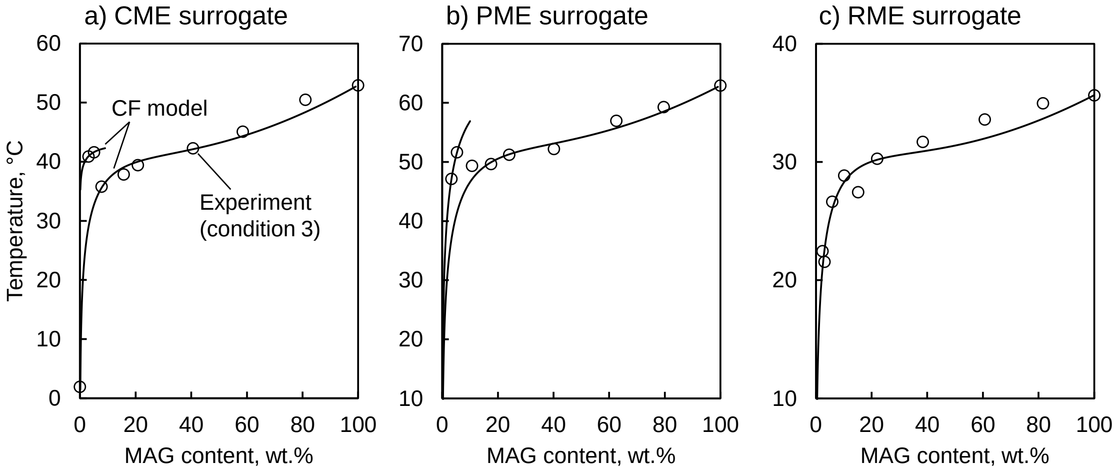

Fig. 5-3 Liquidus temperature determined from experiment by DSC (open circle) and predicted values by CF model (solid line).

As shown in Fig. 5-3, the CF model was able to fit the experimental results well, and the fitting parameters, the stoichiometric composition v_1 and v_2, were determined. In the region of high MAG content, the compositions were uniquely determined as MAG18:0/MAG12:0 = 1.31/0.00 for CME, MAG16:0/MAG18:0 = 0.00/1.60 for PME, and MAG18:0/MAG18:1 = 0.94/0.04 for RME surrogates. Despite the assumption of compound formation, one MAG was estimated to be almost zero. In the low MAG regions of CME and PME, the compositions were changed to be MAG18:0/MAG12:0 = 0.02/0.09 for CME, and MAG16:0/MAG18:0 = 0.50/0.82 for PME. The reason why the tendency of the liquidus curve changed at about 10 wt.% may be that the composition of the compound has changed. However, due to the small number of experimental data in the low MAG regions, these results were not unique, and there were many other parameters to fit. Note that the stoichiometric numbers estimated here only regressing the CF model to the experimental data and do not necessarily represent the actual solid phase. The important point is that the experimental liquidus temperature could be expressed well in the form of the CF model.

5.3.2 Effect of DAGs

As shown in Table 5-1, actual biodiesel may contain not only MAGs but also DAGs and TAGs. Therefore, DAGs were added to the PME surrogates to investigate the effect on the liquidus temperature. The results are shown in Fig. 5-4, where the plots without DAGs are the same as the data shown in Fig. 5-1(b), but Condition 3 is not shown because it almost overlapped with Condition 2. The samples with DAGs were prepared by blending the MAGs and DAGs mixtures in Table 5-4 at a ratio of 4:1 (w/w) and then mixing with the FAMEs mixture in various ratios. Fig. 5-4 shows the liquidus temperature as a function of MAG content, which appears to be on approximately the same line regardless of the presence or absence of DAGs, although samples with DAGs are slightly lower. Therefore, even if DAGs are present in biodiesel, they do not affect the liquidus temperature so much, and it might be sufficient to consider only MAGs to predict the liquidus temperature.

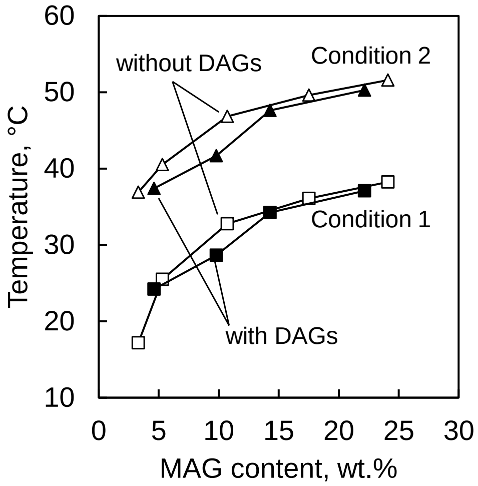

Fig. 5-4. Liquidus temperature of surrogate PME that consisted of MAGs only (open symbols) or MAGs and DAGs (solid symbols) when measured by various conditions in DSC

In the CF model, not only MAG/MAG but also, for example, MAG/DAG or DAG/DAG may form compounds. However, previous studies of acylglycerol binary systems (Chapter 4) showed that all combinations of acylglycerols except MAG/MAG mixtures tended to follow the NSS model, meaning that DAGs and TAGs do not interact with MAGs and solidify independently as pure components. In addition, MAGs generally have higher contents and slightly higher melting points than DAGs and TAGs, meaning that MAGs will generally determine the liquidus temperature of biodiesel. Therefore, it is suggested that only the compound formation of MAG/MAG should be considered to predict the liquidus temperature of biodiesel. and this suggestion was supported even for multicomponent systems by the results of Fig. 5-4. This suggestion was supported even for multicomponent systems by the results of Fig. 5-4 as no significant difference in liquidus temperature was observed with the presence DAG in the mixture.

5.3.3 Actual biodiesel samples

Fig. 5-5 shows the liquidus temperatures determined by visual observation for actual biodiesel samples. Because of the limited ranges of MAG content of actual biodiesel samples, some data obtained from the surrogate samples were added; filled circles are the data of surrogates, and open circles are those of actual biodiesels. The data of actual biodiesel with MAG contents do not present in Table 5-1 were measured by mixing biodiesels with different MAG contents. In triplicate trials for each data point, experimental uncertainties were within −0.2 to +0.2 ℃ of the mean for CME, −0.1 to +0.1 ℃ for PME, and −0.1 to +0.2 ℃ for RME. Note that the liquidus temperature determined by visual observation would be attributed to the β-type MAGs, according to our previous study (Yoshidomi et al., 2017). This may be because slow heating and stirring in visual observation ensure crystal transitions.

For all the biodiesel samples a) ~ c), the liquidus temperature is almost constant in very low MAG content regions, where solidification of saturated FAME would occur. However, when the MAG content increases, a sudden rise in the liquidus temperature is observed, suggesting that MAG was no longer soluble in FAMEs and started to solidify. This limit is called the solubility limit of MAGs in this study and was about 0.25 wt.% for CME and 0.5 wt.% for PME and RME. It should be noted that these values are lower than the regulation of MAG content in biodiesel standards; European standard EN14124 stipulates the MAG content of 0.8 wt.% or less (Committee for Standardization Automotive Fuels, 2008). Paryanto et al. suggested that this regulation should be tightened to 0.40 – 0.62 wt.% to prevent technical problems of B30 blend fuels (Paryanto et al., 2019), and this current study also supports this suggestion.

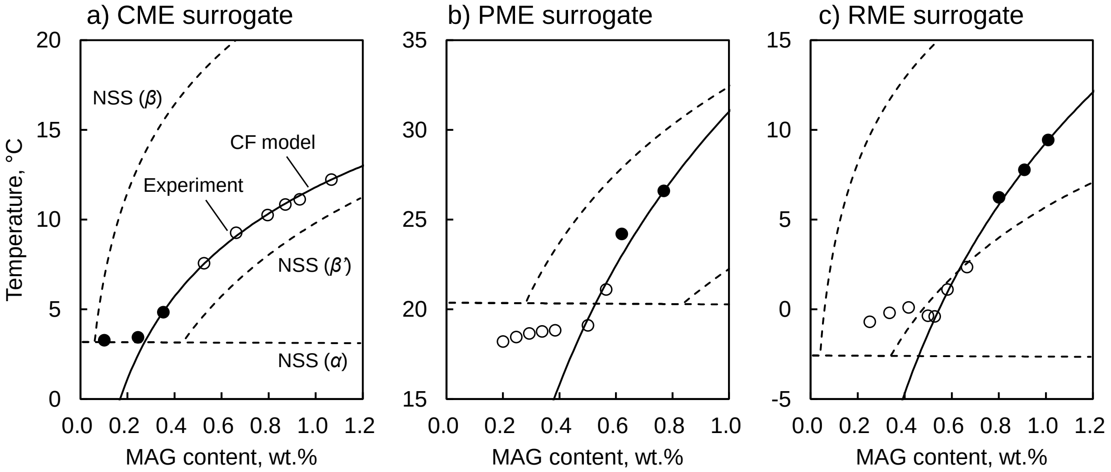

Fig. 5-5. Liquidus temperature determined from experiment by visual observation: actual biodiesel (open circle) and surrogate biodiesel (solid circle), with predicted values by NSS model (dashed lines) and CF model (solid line)

Regarding the calculation results of the NSS model, the liquidus temperature is almost constant when assuming α-type MAG because the solidification of FAME occurs in this case. In the case of CME, the liquidus temperature begins to rise at a MAG content of 0.45 wt.% in the calculation for β'-type and at 0.06 wt.% for β. These calculated results by the NSS model differ significantly from the experimental data for both the solubility limit and liquidus temperature. This discrepancy is also true for PME and RME.

On the other hand, the fitting curves by the CF model are depicted by solid lines in Fig. 5-5, which match well with the experimental results. In all types of biodiesels, the MAGs with the first and second highest liquidus temperatures in Equation (5-2) were MAG16:0 and MAG18:0 (but the order was different) when the MAG content was less than 1.2 wt.%, and the fitting results for Figure 5 were MAG16:0/MAG18:0 = 0.10/0.88 for CME, 1.00/0.61 for PME, and 0.04/2.94 for RME, respectively. However, these were not unique, and other numbers could regress the experimental results as well. The use of two variables (v_1 and v_2) in the CF model seem to be excessive for fitting in such narrow regions. Moreover, the numerical calculations, including the activity coefficient, were very complicated and not practical. Therefore, we tried to simplify the CF model in Equation (5-4). Replacing the mole fractions of MAGs in biodiesel (x_i) with the product of the total MAG content (M, w/w) and the fatty acid composition (c_i) gives the following equation:

$$({\gamma_1}^L x_1)^{v_1}({\gamma_2}^L x_2)^{v_2} = ({\gamma_1}^L c_1)^{v_1}({\gamma_2}^L c_2)^{v_2} M^{v_1+v_2} = K_{\mathrm{ref}} \exp\left(\frac{\Delta H_{\mathrm{ref}}}{RT_{\mathrm{ref}}}\frac{T-T_{\mathrm{ref}}}{T}\right) \tag{5-6}$$

As shown in section 2.3.3, the activity coefficient of MAG in FAME (${\gamma_i}^L$) varies widely in the range of MAG content from 0 to 100 wt.%. However, in the narrower range of less than about 1 wt.%, the variation is slight, and it may be regarded as constant. The fatty acid composition (c_i) is also constant for the known feedstock. Incorporating these constant terms into K_{ref} and considering $v_1 + v_2$ as one parameter v results in the following simplified CF model.

$$M^v = {K_{\mathrm{ref}}}' \exp\left(\frac{\Delta H}{RT_{\mathrm{ref}}}\frac{T-T_{\mathrm{ref}}}{T}\right) \tag{5-7}$$

Once a measured liquidus temperature is chosen as T_{ref}, ${K_{\mathrm{ref}}}'$ is inevitably determined. In this study, a value of 70 kJ/mol was used for ΔH, which is intermediate between the enthalpies of fusion of β-type MAG16:0 and MAG18:0.

The experimental results in Fig. 5-5 were fitted using Equation (5-7), and v was uniquely determined to be 0.70 for CME, 1.59 for PME, and 1.68 for RME. The fitting curves are not shown in Fig. 5-5 because they completely overlapped with the results of the conventional CF model. In this way, the simplified CF model was sufficient to represent the experimental results, and the liquidus temperature is thought to be predicted based on the total MAG content if the feedstock is known.

Remind that the results by visual observation in Fig. 5-5 correspond to the liquidus temperatures of β-type MAGs, which have the highest melting point among all crystal forms of MAGs. Therefore, the results in Figure 5 represent the most stringent criteria for the risk of biodiesel solidification. Previous study suggested that the cloud point was related to the solidification of α-type MAGs (Sugami et al., 2017) so that the measured cloud point would be lower than the results in Fig. 5-5, but it does not represent a real risk. Although this study dealt with the liquidus temperature, the form of Equation (5-7) will also be helpful as a semi-empirical equation in predicting other cold flow properties such as the cloud point.

5.4 Conclusions

The liquidus temperatures of actual and simulated biodiesel fuels were measured and compared with those calculated by the NSS and CF models. The NSS model deviated significantly from the experimental results, while the CF model fitted well for a wide range of biodiesel samples with MAG content from the solubility limit to 100 wt.%. The solubility limit of MAGs, above which β-type MAG crystals can solidify before FAMEs, was found to be about 0.25 wt.% for CME and about 0.5 wt.% for PME and RME.

However, within the range of MAG content in actual biodiesel (below 0.8 wt.%), using two fitting parameters in the CF model was excessive. Within this range, the simplified CF model with only one fitting parameter and no consideration of the activity coefficient was sufficient to fit. One parameter was determined for biodiesel from one feedstock, making it possible to calculate the liquidus temperature only based on the total MAG content. Even if the biodiesel contained DAGs, its effect on the liquidus temperature was limited, and even for such biodiesel, the liquidus temperature could be calculated only from the MAG content. On the other hand, for biodiesel containing MAGs less than the solubility limit, the NSS model could roughly predict the liquidus temperature, at which the solidification of FAME would occur.

Chapter 6 Interactions between Biodiesel Components and Fossil Diesel Components during Solidification

6.1 Introduction

Biodiesel is commonly used by blending with conventional fossil diesel because they can be mixed at any ratio. However, mixing biodiesel worsens the cold flow properties of fossil diesel even if the biodiesel content is as low as 1 vol.% (Leng et al., 2020). In this sense, blend fuels can solidify at higher temperatures compared to neat fossil diesel. Therefore, it is important to predict the liquidus temperature of blend fuels to prevent practical problems and encourage biodiesel blending at higher contents.

The solid-liquid phase behavior of FAME or FAAE in hydrocarbons has been studied by various researchers. Benziane et al. have reported that binary mixtures of FAME and heavy alkanes exhibit simple eutectic behavior (Benziane, Khimeche, Dahmani, et al., 2013). They have confirmed that FAME/aromatic mixtures are also eutectic (Benziane, Khimeche, Trache, et al., 2013). In these studies, the mixtures behaved as non-ideal liquid solutions, represented by common activity coefficient models, such as the Wilson equation, NRTL, and UNIQUAC. FAAE and hydrocarbon mixtures have been investigated by Robustillo et al. (2014) and Chabane et al. (2018), and almost all mixtures were eutectic. An exception was found in FAAE12:0 and *n*-C10 that showed peritectic behavior (Robustillo et al., 2014). A systematic study by Branco et al. suggested that the difference in alkyl chain length between alkane and FAME determines whether the behavior is eutectic, peritectic with co-crystal, or solid solution (Branco et al., 2020). However, the interaction between MAGs and hydrocarbons remains unclear.

Therefore, the objective of this chapter is to clarify the interactions between biodiesel components (FAME and MAG) and fossil diesel components (alkanes and aromatics) during solidification and to evaluate the performance of the thermodynamic model. The liquidus temperature of binary mixtures was determined by DSC, and the results were compared with the NSS model. The results of this study shall serve as the fundamental research to develop prediction models for actual blend fuels.

6.2 Methodology

6.2.1 Experiments

(1) Materials

High purity chemicals were used to prepare binary mixtures of FAME/alkane, FAME/aromatics, MAG/alkane, and MAG/aromatics. Normal alkanes with 99 % purity, *n*-dodecane (*n*-C12) and *n*-nonadecane (*n*-C19), were obtained from Nacalai Tesque Inc., Kyoto, Japan, and Tokyo Chemical Industries (TCI), Tokyo, Japan, respectively. Aromatic compounds used in this study were toluene (≥ 99 % purity) and 1-methylnaphthalene (96 % purity) purchased from Nacalai Tesque. Pure FAMEs (99 % purity), methyl palmitate (FAME16:0) and methyl oleate (FAME18:1), were obtained from Sigma-Aldrich Japan, K.K., Tokyo, Japan. As pure MAG (99% purity), 1-monopalmitin (MAG16:0) was purchased from Olbracht Serdary Research Chemical, Toronto, Canada. These chemicals were used as received without purification.

(2) Analytical method

DSC analysis was conducted to determine the liquidus temperature of binary mixtures. Approximately 10 mg of the sample was placed in a sealed aluminum crimp cell. The sample was exposed to dry nitrogen flow (50 ml/min), heated 20 degrees above the higher melting point of the components, and hold at that temperature for 1 minute to be completely melted. Either of these conditions was then applied to the sample:

Condition 1: The melted sample was cooled rapidly (-10 °C/min) until the first exothermic peak had completed, and then immediately heated (10 °C/min) until completely melted, recording the DSC profile. Rapid heating was intended to avoid the transition of MAG crystals, as demonstrated in the previous chapters. This condition was applied in all samples.

Condition 2: the melted sample was cooled rapidly to room temperature and kept for at least 24 hours. The sample was then cooled to -50 °C and heated (10 °C/min) while DSC profile was recorded. This measurement was intended to determine the behavior of mixture with MAG at the most stable form and was applied only in some special cases.

DSC profiles were recorded by using alumina as reference material. The liquidus temperature was determined from the highest peak temperature of the last endothermic peak. The average liquidus temperature of three times measurement was reported.

Table 6-1. Pure component properties and UNIFAC group assignments

Component	Number of UNIFAC functional group										Melting point (°C)	Enthalpy of fusion (kJ mol^{-1})
	CH_3	CH_2	CH	CH=CH	ACH	$ACCH_3$	AC	OH(p)	OH(s)	CH_2COO		
Methyl palmitate (FAME16:0)	2	13	-	-	-	-	-	-	-	1	29.8	55.3
Methyl oleate (FAME18:1)	2	13	-	1	-	-	-	-	-	1	20.7	41.6
1-Monopalmitin (MAG16:0)*	1	15	1	-	-	-	-	1	1	1	66.4	34.1
n-Dodecane (n-C12)	2	10	-	-	-	-	-	-	-	-	-9.6	36.8
n-Nonadecane (n-C19)	2	17	-	-	-	-	-	-	-	-	32.0	42.7
Toluene	-	-	-	-	5	1	-	-	-	-	95.0	6.6
1-Methyl-naphthalene	-	-	-	-	7	1	2	-	-	-	-22.0	9.7

*MAG was assumed as α-type crystal.

Meanwhile, pure component properties were measured by the same procedure as the binary mixtures. The melting point was determined as the onset temperature of the endothermic peak. The enthalpy of fusion was calculated from the area of the endothermic peak.

For some cases, infrared spectra of the mixtures were measured by Fourier transformation infrared (FTIR) analysis with an attenuated total reflector (ATR) to allow observation at various temperatures. A small sample was analyzed directly in the instrument as solid phase or liquid phase by adjusting the temperature on a heating plate.

6.2.2 Thermodynamic model

The NSS model, as described in section 2.2.2, was applied to calculate the liquidus temperature. The UNIFAC (Dortmund) method was used to estimate the activity coefficient. The pure component properties used in the calculations are summarized in Table 6-1.

6.3 Results and discussion

6.3.1 FAME and hydrocarbon mixtures

Fig. 6-1 shows the liquidus temperatures of binary mixtures of FAME18:1/*n*-C19 (a) and FAME16:0/toluene (b) determined by DSC condition 1 and the NSS model. The experimental uncertainties in the triplicate measurement were within 1 °C.

Both the FAME/alkane (a) and FAME/aromatic (b) mixtures have similar behavior, in which a gradual increase in liquidus is observed with increasing the higher melting point component. Such behavior indicates relatively good solubility of FAME in both alkane and aromatic components. Although the liquidus curves of both mixtures showed a monotonous increase trend, DSC analysis did not measure the solidus temperature, making it impossible to identify if these mixtures were eutectic. The reason why the solidus could not be measured might be the large disparity in the melting point of the components in the binary mixtures.

Nevertheless, previous studies by Benziane et al. reported that binary mixtures of FAME/alkane with close melting points, such as FAME18:0 and *n*-tetracosane (T_m = 50 °C) and FAME16:0 and *n*-eicosane (T_m = 36 °C), behaved like a simple eutectic

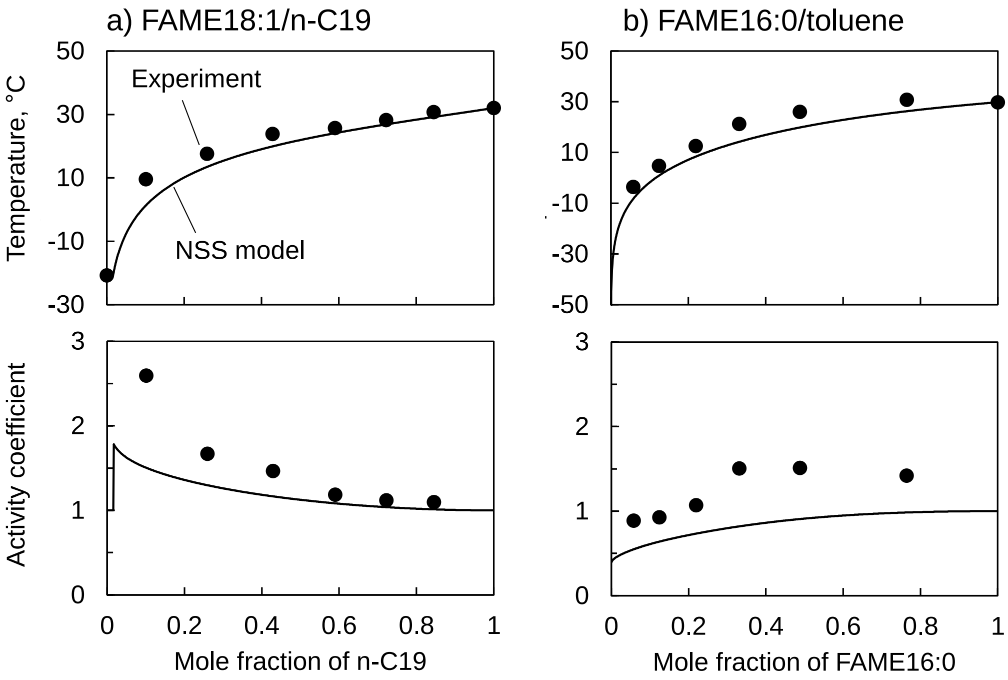

Fig. 6-1. Liquidus temperature (top) and activity coefficient of binary mixtures of a) FAME18:1/*n*-C19 and b) FAME16:0/toluene determined by DSC analysis (solid circle) and predicted by the NSS model (solid line).

system (Benziane, Khimeche, Dahmani, et al., 2013). Eutectic behavior was also observed in binary mixtures of FAME/aromatics, such as FAME16:0 or FAME18:0 with biphenyl (T_m = 69 °C) or naphthalene (T_m = 80 °C). Therefore, FAME and hydrocarbons might be generally immiscible in one solid phase. It can be assumed that similar behavior was also observed in the mixtures of the current study.

The liquidus curves predicted by the NSS model are also shown by solid curves in Fig. 6-1. Although the NSS model generally generates a v-shaped curve, calculation results show a monotonically increasing curve due to the large difference in melting point between the components in the mixture. The calculated liquidus temperature and activity coefficient (dashed lines) were relatively close to the experimental values, suggesting that the UNIFAC (Dortmund) could represent the non-ideality of FAME18:1/*n*-C19 and FAME16:0/toluene mixtures well. Thus, the NSS model was considered useful for predicting the actual solidification behavior of FAME in alkane and aromatic compounds.

6.3.2 MAG and hydrocarbon mixtures

The liquidus curves of binary mixtures of MAG/alkane are shown in Fig. 6-2, while those of MAG/aromatics are in Fig. 6-5. The experimental uncertainties in the triplicate trials were within -0.7 to +0.6 °C of the mean.

(1) MAG and alkanes

Fig. 6-2 shows the experimental liquidus temperature (solid circle) of binary mixture MAG16:0/*n*-C12 with α-type (a) and β-type (b) MAG. The MAG16:0/*n*-C12 shows a peculiar tendency that the liquidus temperature is almost constant regardless of the composition. As an exception, a sudden rise in the liquidus temperature is observed at the MAG content close to zero. From this point, the liquidus temperature increases slightly even if the MAG content is further increased. This pattern of the liquidus curve suggests that MAG has low solubility in *n*-alkanes, so the liquidus temperature is close to the melting point of pure MAG16:0 (°C) at any composition.

The NSS model was applied to the binary mixtures, and the resulting curves are shown by solid lines in Fig. 6-2. The predicted curves deviate significantly from the experimental liquidus temperature. The deviation is especially notable at low MAG16:0 concentrations, and the NSS model shows significantly higher values than the experimental results. Possible reasons for this deviation include liquid-liquid separation of MAG and alkane and problems in the prediction model.

In fact, liquid-liquid separation has been reported in mixtures of MAG10:0 and heavy oils squalane (C30) or squalene (C30) (Shrestha et al., 2006). However, no separation was visually observed in the melted MAG/alkane mixtures in this study. Therefore, FTIR analysis was conducted to confirm whether the MAG/alkane has other special behavior than the MAG/FAME mixture, and the results are shown in Fig. 6-3.
The FTIR spectra of MAG/FAME, which produces a simple eutectic mixture in the solid phase (Yoshidomi et al., 2017), were first analyzed. Pure FAME18:1 shows a sharp peak at 1710 cm^{-1} corresponding to C=O stretching. Pure MAG16:0 shows a broad peak around 3400 cm^{-1}, the signal of OH groups, and this broad peak suggests the presence of flexible hydrogen bonds. The C=O stretching peak in pure MAG is split into two peaks, 1738 and 1717 cm^{-1}, corresponding to the free and hydrogen-bonded C=O groups, respectively. When MAG16:0 and FAME18:1 are mixed in a ratio of 50:50, the single C=O peak of

FAME18:1 overlaps with the two split C=O peaks of MAG16:0. Since the MAG16:0/FAME18:1 spectrum seems to be the sum of pure MAG16:0 and FAME18:1 spectra, there might be no special interaction between these components in the liquid phase. Due to this feature, the MAG/FAME mixture is thought to produce a eutectic mixture in the solid phase.

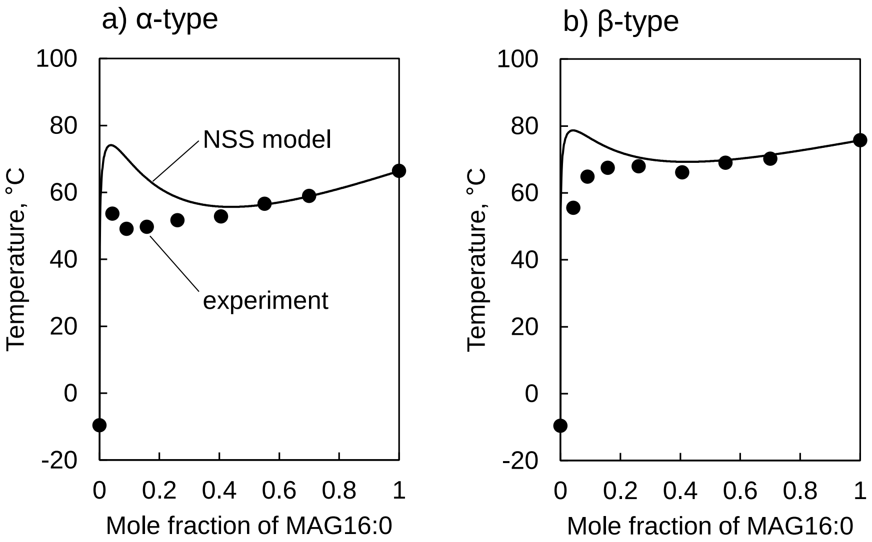

Fig. 6-2. Liquidus temperature of binary mixtures of MAG16:0/*n*-C12 determined by DSC (solid circle) and predicted values by the NSS model (solid line).

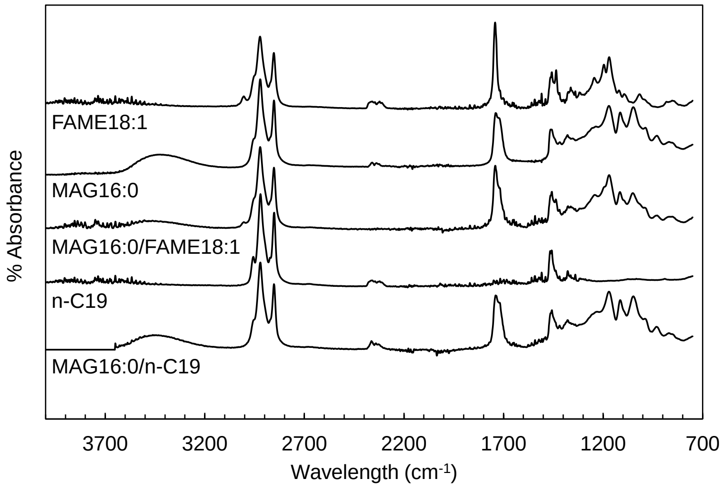

Fig. 6-3. FTIR spectra of pure components and binary mixtures of *n*-C12, MAG16:0, and FAME18:1 measured in the liquid phase.

The FTIR spectra of pure *n*-C19 and MAG16:0/*n*-C19 mixture are also shown in Fig. 6-3. As expected, the peaks of OH and C=O are not observed in pure *n*-C19. When *n*-C19 is mixed with MAG16:0 at a 50:50 ratio, the peaks of OH and C=O derived from MAG16:0 appear, but the spectrum is like the sum of pure components' ones. Therefore, there is also no special interaction between *n*-C19 and MAG16:0, and this mixture might behave as a eutectic mixture similar to MAG16:0/FAME18:1.

From these results, the deviation of the predicted liquidus temperature from the experimental results might be caused by the calculations in the NSS model. Since the liquidus temperature is highly affected by the activity coefficient, Fig. 6-4 compares the experimental results (solid circle) with the predicted values (lines) for the liquidus temperature and activity coefficient. In addition, calculations assuming a virtual MAG16:0 without primary (OH (p)), secondary (OH(s)), or both hydroxyl groups are included for comparison.

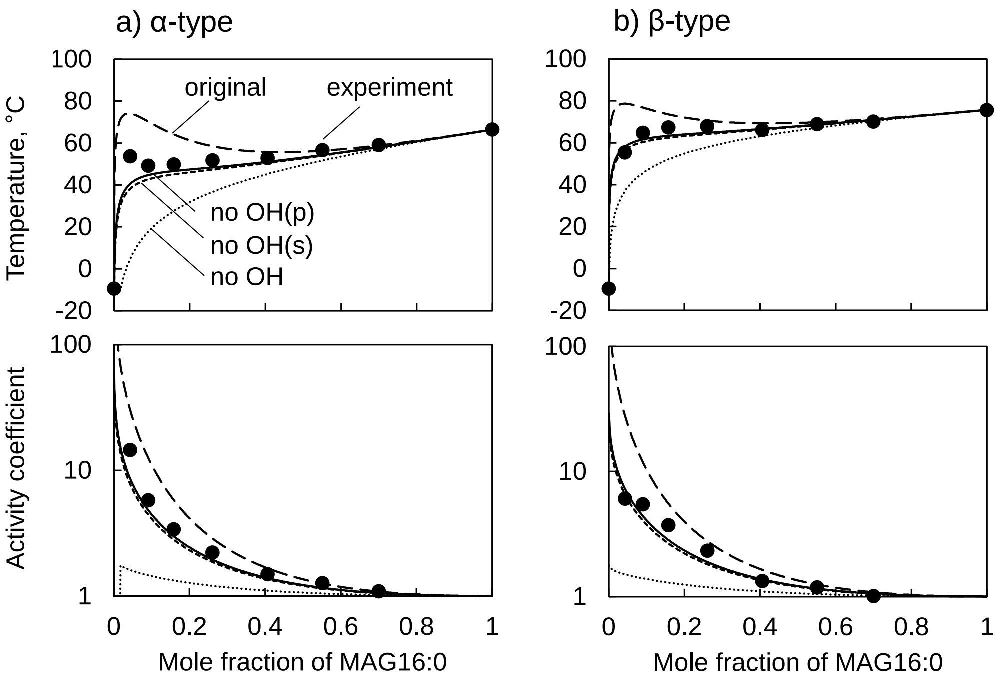

Fig. 6-4. Comparison of the liquidus temperature (top) and activity coefficients (bottom) of the binary mixture of MAG16:0/*n*-C12; solid circle, experimentally determined values; lines, calculated values by the NSS model, assuming original MAG16:0 and hypothetical MAG16:0 without OH(p), OH(s), or both OH groups.

The results indicate that the predicted activity coefficient of MAG16:0 (long-dashed line) is somewhat higher than the experimental value (solid circle). Since the activity coefficient is close to unity when the mole fraction of MAG16:0 is higher than 0.4, this deviation does not affect the liquidus temperature so much. On the contrary, the predicted activity coefficient at low MAG content is much higher than the experimental value, estimating very high liquidus temperature.

The UNIFAC (Dortmund) model tends to infer the activity coefficient as high values when the components have functional groups with different polarities; for example, in the case of MAG in alkane, only the former has two hydroxy groups. Thus, the effect of hydroxyl groups was studied by eliminating either the primary (p), secondary (s), or both OH groups in the calculation. Eliminating either of the hydroxyl groups reduces the activity coefficient significantly, similar to the experimental results. Eliminating both OH groups further reduce the activity coefficient and significantly decreased the liquidus temperature. Therefore, the deviation of the predicted liquidus temperature might be due to the UNIFAC (Dortmund) model overestimating the interaction between hydroxyl groups of MAG and alkyl groups of alkanes.

In reality, the long-chain alkyl group of MAG has a high affinity for alkanes, so the effect of the OH groups may not be as pronounced as estimated by the UNIFAC (Dortmund) model. For example, the molecular structure of MAG has two different polarities; the OH group can act as the “head,” and the long-chain alkyl group can act as the “tail”. As a result, the heads of MAGs may associate to form micelle-like aggregates in alkane (Chen et al., 2009), as shown in Fig. 6-5. In such cases, alkanes cannot interact directly with OH groups of MAGs, and thus their effect would be overestimated by the UNIFAC (Dortmund). Since the UNIFAC (Dortmund) model does not consider such three-dimensional structures of molecules, errors may occur for substances that can form micelles or intramolecular hydrogen bonds.

(2) MAG and aromatics

Fig. 6-6 shows the liquidus temperatures of MAG16:0 in toluene or 1-methylnaphthalene. When the MAG16:0 content increases slightly from zero, the liquidus temperature rises drastically, but it is almost constant even when the MAG content further increases. At some point, the liquidus shows a slight decrease before finally reaching the melting point of pure MAG16:0. Considering that this behavior was observed in both mixtures, it can be assumed that this liquidus pattern is typical in MAG/aromatic mixtures. The calculation results by the NSS model are shown as solid curves in Fig. 6-6.

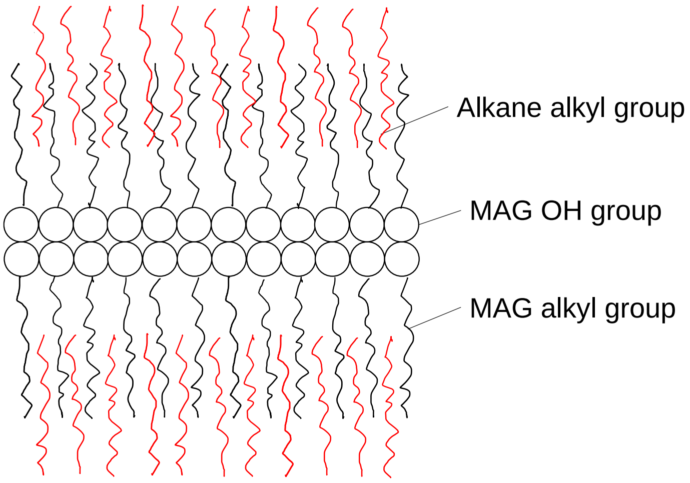

Fig. 6-5. Hypothesized molecular arrangement of MAG and alkane mixtures

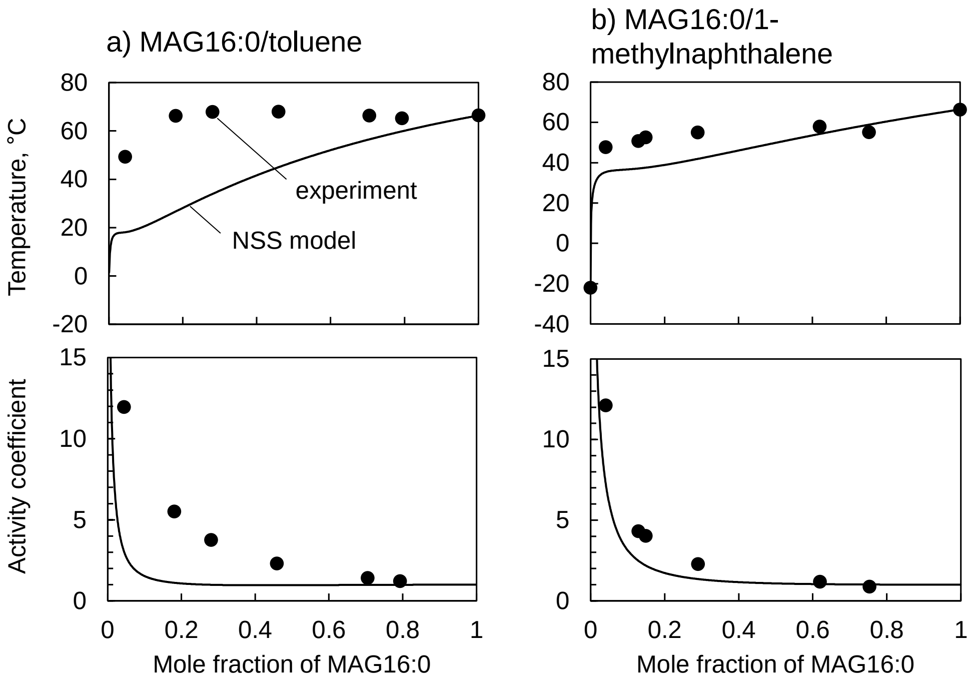

Fig. 6-6. The liquidus temperature (top) and activity coefficient (bottom) of binary mixtures of MAG/aromatics determined by DSC (solid circle) and predicted values by the NSS model (solid line).

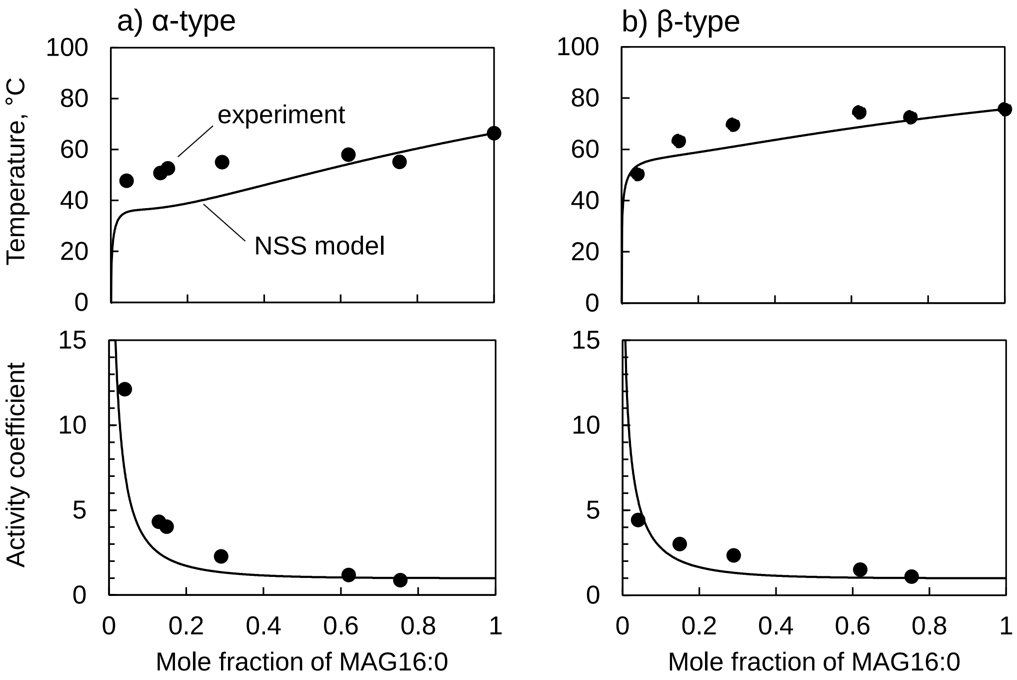

Fig. 6-7. Comparison of the liquidus temperatures (top) and activity coefficient (bottom) of MAG16:0/1-methylnaphthalene mixtures with different MAG forms, as determined by DSC (solid circle) and predicted values by the NSS model (solid line).

The large deviation between the predicted values and the experimental results means that the NSS model could not predict the solid-liquid behavior of MAG/aromatics. This deviation is especially large at the MAG16:0 content below 0.8. However, contrary to the case of MAG/alkanes, the experimental liquidus temperature tends to be significantly higher than the calculated value, meaning that the UNIFAC (Dortmund) model underestimated the activity coefficient. In this case, unlike the MAG/alkane mixtures, it is unlikely that the effect of OH groups was inhibited by the formation of micelles or intramolecular hydrogen bonds. Therefore, the deviation between the experimental and predicted values might be due to other reasons, such as the transition of MAG crystals from α-type to more stable forms.

The sample was then conditioned to produce the most stable MAG form (β-type) by allowing it to rest at room temperature for about 2000 hours before conducting the DSC analysis. The comparison of liquidus temperatures of the α-type and β-type was demonstrated in MAG16:0/1-methylnaphthalene mixture, as shown in Fig. 6-7. The long storage period successfully produced β-type MAG, indicated by higher experimental liquidus temperature (solid circle) in β-type (b) MAG compared to α-type (a) MAG. As in α-type, the experiment activity coefficient (solid circle) of β-type MAG was higher than that predicted by the NSS model (solid curve). This indicated that the deviation of the calculated liquidus temperature was not due to the crystal transition but from the underestimated activity coefficient of MAG. Therefore, the affinity of MAG16:0 and aromatic solvent was not as good as expected by the UNIFAC (Dortmund) model. The reason for this tendency was still unclear, however, it is worth noting that the UNIFAC (Dortmund) model had difficulty predicting the activity coefficient of MAG in hydrocarbons and the problem of the NSS model remains.

6.4 Conclusions

The solidification behavior of binary mixtures of FAME/hydrocarbons and MAG/hydrocarbons was investigated. The mixtures of FAME/alkane and FAME/aromatics produced a simple eutectic system, which was well predictable by the NSS model. The MAG/alkane mixtures showed liquidus temperatures similar to the melting point of pure MAG regardless of the composition. Although the experimental results suggested a typical eutectic system, the NSS model could not predict the liquidus temperature because the activity coefficient was overestimated. This overestimation may be due to the formation of micelles or intramolecular hydrogen bonds of MAGs.

Similarly, the MAG/aromatics mixtures, regardless of the composition, showed liquidus temperatures close to or slightly above the melting point of pure MAG, which was unpredictable by the NSS model. Evaluation of the liquidus temperature from the most stable MAG form indicated that the main cause of the deviation was located in the NSS model itself.

From the above results, it was considered necessary to improve the thermodynamic model to predict the liquidus temperature of biodiesel and fossil diesel blends.

Chapter 7 Conclusions

7.1 Concluding remarks

Biodiesel is produced by transesterification of plant oils with methanol. In this reaction, one TAG molecule is converted into DAG, MAG, and then free glycerol, producing one FAME molecule in each step (three molecules in total). Even after the catalyst and glycerol are removed by washing with water, unreacted TAG and intermediate DAG and MAG can remain in biodiesel as minor components with the total content typically below 1 wt.%. These acylglycerols, especially ones bonded to saturated fatty acids, have high melting points and worsen the cold flow properties of biodiesel, such as the cloud point and cold filter plugging point. In addition, acylglycerols have polymorphs with multiple melting points, which also complicates the solidification behavior.

The objective of this dissertation was to elucidate the solidification behavior of acylglycerols and their effect on the cold flow properties of biodiesel. For this purpose, the liquidus temperatures of binary and multi-component mixtures, including actual biodiesel samples, were determined by differential scanning calorimetry (DSC) or visual observation. The liquidus temperature is the temperature above which the solid phase can no longer remain in the mixture, and is an important index of the cold flow properties. Thermodynamic models based on the theory of solid-liquid equilibrium were applied to the experimental results to discuss the solidification behavior. A modified version of the universal quasi-chemical functional group activity coefficient (UNIFAC) model, known as the UNIFAC (Dortmund) method, was applied to estimate the liquid phase activity coefficient.

In Chapter 2, studies of MAG, DAG, and TAG dissolved in FAME revealed that these acylglycerols increased the liquidus temperature significantly, even in small concentrations, and readily precipitate out of FAME. The experimentally determined liquidus temperatures were in good agreement with those calculated by the non-solid-solution (NSS) model, suggesting that acylglycerols tend to precipitate as a pure substance. Meanwhile, the UNIFAC (Dortmund) model was able to accurately evaluate the activity coefficients of these lipid systems, even though slight deviations were found in the evaluation for TAGs.

According to the UNIFAC (Dortmund) calculation, MAG had high activity coefficients when dissolved in FAME due to its two hydroxyl groups, which significantly increased the calculated liquidus temperature. In other words, MAG might have a low affinity for FAME and thus be prone to precipitation. On the other hand, the activity coefficients of TAG in FAME were slightly below 1, indicating that TAG has a high affinity for FAME. Nevertheless, the high enthalpy of fusion of TAG due to its high molecular weight caused a significant increase in the calculated liquidus temperature. In the case of DAG, both the high activity coefficient and the high molecular weight were related to the ease of precipitation.

In Chapter 3, the liquidus temperatures of various binary mixtures of MAGs were determined by DSC to elucidate their interactions during solidification. It was found that their liquidus curves had complex shapes with multiple upward convex curves. Such complex liquidus curves could not be explained by the simple NSS model, while the compound formation (CF) model fitted well. Thus, it suggests that MAGs in actual biodiesel do not precipitate separately as pure components, but precipitate while forming complex molecular compounds. The CF model includes fitting parameters, which had to be determined from the experimental data, and the parameters varied with the composition of MAGs. Therefore, the CF model is a semi-experimental formula, and it may be challenging to predict the liquidus temperature of biodiesel with only a complete theoretical model.

Because compound formation behavior was observed in binary MAG/MAG mixtures, confirming whether the same behavior occurs in binary mixtures of other combinations of acylglycerols is of interest in Chapter 4. According to existing literature, TAG/TAG mixtures do not tend to produce molecular compounds, with some exceptions. Other binary mixtures (DAG/DAG, MAG/DAG, MAG/TAG, and DAG/TAG) showed either V-shaped, known as eutectic, or monotonically increasing curves, called monotectic, as well as TAG/TAG mixtures. These experimental results were in good agreement with the NSS model, and it seemed that binary acylglycerol mixtures other than MAG/MAG tended to precipitate separately as pure components without forming molecular compounds. As the MAG content in biodiesel is generally higher than that of DAG and TAG, and MAG is less likely to form molecular compounds with TAG and

DAG, it can be assumed that the effect of DAG and TAG on biodiesel cold flow properties is limited.

Thus, the performance of the CF model for predicting actual biodiesel was demonstrated in Chapter 5. Biodiesel samples with different MAG contents were prepared from various feedstocks. Biodiesel surrogates were also prepared by mixing FAMEs and MAGs to simulate the composition of the biodiesel samples. The liquidus temperatures of these samples were determined visually and by DSC. The solubility limit of MAGs, above which MAGs solidify first and the liquidus temperature increased sharply, was found for each feedstock: approximately 0.25 wt% for coconut and 0.5 wt% for palm and rapeseed biodiesels. The CF model was then applied to the experimental results, and it was shown that the parameters of the CF model could be determined for each feedstock, and the liquidus temperatures of these biodiesel samples could be predicted well. Although the actual biodiesel samples contained DAGs, they seemed to have little effect on the liquid phase temperature, as was assumed from the study in Chapter 4. However, within the range of the total MAG content of actual biodiesel (typically less than 0.8 wt.%), the number of fitting parameters in the CF model was excessive, so a simplified version of the CF model with only one parameter was proposed, which still fitted the experimental results well.

Considering biodiesel and fossil diesel blends, binary mixtures of biodiesel components (FAME or MAG) and fossil diesel components (alkane or aromatic) were studied in Chapter 6. The liquidus temperatures of FAME/alkane and FAME/aromatic binary mixtures followed the NSS model well. This suggests that in mixtures of FAMEs and fossil diesel components, each component tends to precipitate separately as pure components, and the liquidus temperature is easy to predict. However, the MAG/alkane and MAG/aromatic binary mixtures did not agree with the simple NSS model, even though FT-IR analyses did not show the formation of molecular compounds. Therefore, it was likely that the thermodynamic models, particularly the method of estimating the activity coefficient, would need to be further improved to predict the cold flow properties of biodiesel/fossil diesel blends.

In conclusion, the effect of acylglycerols on the biodiesel cold flow properties was clarified, and the behavior of MAGs was considered critical for predicting the liquidus temperature. Different MAGs tended to form molecular compounds and solidify, and the

CF model could describe their behavior well. On the other hand, since DAG and TAG did not tend to form molecular compounds with MAG, their influence on the biodiesel cold flow properties was considered limited. As a result, it was demonstrated that the CF model could reasonably predict the liquidus temperature of biodiesel whose fatty acid composition is known, i.e., the feedstock is known. On the other hand, the behavior of MAG in alkanes and aromatics could not be explained by the thermodynamic models studied, suggesting that it is difficult to predict the cold flow properties of biodiesel/fossil diesel blends without improving the thermodynamic models.

7.2 Prospects for future research

This study elucidated the impact of acylglycerols on the cold flow properties of biodiesel and evaluated thermodynamic models for discussing the solidification behavior. Despite the results, several issues remain unclear and may be explored in future studies.

The study revealed the limitation of the UNIFAC (Dortmund) method to predict the activity coefficient of MAG/TAG mixture and also MAG/alkane and MAG/aromatics. This indicates that the interaction parameter between functional groups, especially hydroxyl groups in acylglycerols, might need to be reinvestigated by using more data set involving lipid mixtures. New functional group parameters specific for acylglycerols might also be proposed to avoid significantly revising the existing UNIFAC group parameter.

After the thermodynamic model for MAG/hydrocarbon mixtures is clarified, the next step will be improving thermodynamic models for binary mixtures and multi-component mixtures. When developing the thermodynamic model, the chemical groups that have a significant effect on the cold flow properties can be identified by using model mixtures. The result of the study shall be the fundamental consideration for developing a prediction model for the actual blend fuels.

References

Abrams, D. S., & Prausnitz, J. M. (1975). Statistical thermodynamics of liquid mixtures: A new expression for the excess Gibbs energy of partly or completely miscible systems. *AIChE Journal*, *21*(1), 116–128. https://doi.org/10.1002/aic.690210115

Al-Shanableh, F., Evcil, A., & Savaş, M. A. (2016). Prediction of Cold Flow Properties of Biodiesel Fuel Using Artificial Neural Network. *Procedia Computer Science*, *102*(August), 273–280. https://doi.org/10.1016/j.procs.2016.09.401

Baker, M., Bouzidi, L., & Narine, S. S. (2015). Mitigating crystallization of saturated FAMEs (fatty acid methyl esters) in biodiesel: 2 The phase behavior of 2-stearoyl diolein-methyl stearate binary system. *Energy*, *83*, 647–657. https://doi.org/10.1016/j.energy.2015.02.076

Balabin, R. M., & Safieva, R. Z. (2011). Near-infrared (NIR) spectroscopy for biodiesel analysis: Fractional composition, iodine value, and cold filter plugging point from one vibrational spectrum. *Energy and Fuels*, *25*(5), 2373–2382. https://doi.org/10.1021/ef200356h

Baptista, P., Felizardo, P., Menezes, J. C., & Neiva Correia, M. J. (2008). Multivariate near infrared spectroscopy models for predicting the iodine value, CFPP, kinematic viscosity at 40 °C and density at 15 °C of biodiesel. *Talanta*, *77*(1), 144–151. https://doi.org/10.1016/j.talanta.2008.06.001

Benziane, M., Khimeche, K., Dahmani, A., Nezar, S., & Trache, D. (2013). Experimental determination and prediction of (solid + liquid) phase equilibria for binary mixtures of heavy alkanes and fatty acids methyl esters. *Journal of Thermal Analysis and Calorimetry*, *112*(1), 229–235. https://doi.org/10.1007/s10973-012-2654-2

Benziane, M., Khimeche, K., Trache, D., & Dahmani, A. (2013). Experimental determination and prediction of (solid + liquid) phase equilibria for binary mixtures of aromatic and fatty acids methyl esters. *Journal of Thermal Analysis and Calorimetry*, *114*(3), 1383–1389. https://doi.org/10.1007/s10973-013-3147-7

Branco, N. F. M., Lobo Ferreira, A. I. M. C., Ribeiro, J. C., Santos, L. M. N. B. F., & Coutinho, J. A. P. (2020). Understanding the thermal behaviour of blends of biodiesel and diesel: Phase behaviour of binary mixtures of alkanes and FAMEs. *Fuel*, *262*(October 2019), 116488. https://doi.org/10.1016/j.fuel.2019.116488

Chabane, S., Benziane, M., Khimeche, K., Trache, D., Didaoui, S., & Yagoubi, N. (2018). Low-temperature behavior of diesel/biodiesel blends: Solid–liquid phase diagrams of binary mixtures composed of fatty acid ethyl esters and alkanes. *Journal of Thermal Analysis and Calorimetry*, *131*(2), 1615–1624. https://doi.org/10.1007/s10973-017-6614-8

Chen, C. H., Van Damme, I., & Terentjev, E. M. (2009). Phase behavior of C18 monoglyceride in hydrophobic solutions. *Soft Matter*, *5*(2), 432–439. https://doi.org/10.1039/b813216j

Chupka, G. M., Fouts, L., Lennon, J. A., Alleman, T. L., Daniels, D. A., & McCormick, R. L. (2014). Saturated monoglyceride effects on low-temperature performance of biodiesel blends. *Fuel Processing Technology*, *118,* 302–309. https://doi.org/10.1016/j.fuproc.2013.10.002

Chupka, G. M., Fouts, L., & McCormick, R. L. (2012). Effect of low-level impurities on low-temperature performance properties of biodiesel. *Energy and Environmental Science*, *5*(9), 8734–8742. https://doi.org/10.1039/c2ee22565d

Chupka, G. M., Yanowitz, J., Chiu, G., Alleman, T. L., & McCormick, R. L. (2011). Effect of saturated monoglyceride polymorphism on low-temperature performance of biodiesel. *Energy Fuels*, *25,* 398–405. https://doi.org/10.1016/j.fuproc.2013.10.002

Committee for Standardization Automotive Fuels. (2008). *Fatty acid methyl esters (FAME) for biodiesel engines - Requirements and test methods (EN14214)*. European Committee for Standardization CEN.

Committee for Standardization Automotive Fuels. (2012). Automotive fuels - Fatty acid methyl esters (FAME) for biodiesel engines - Requirements and test methods (EN14214). *European Standard*.

Correa, D. F., Beyer, H. L., Fargione, J. E., Hill, J. D., Possingham, H. P., Thomas-Hall, S. R., & Schenk, P. M. (2019). Towards the implementation of sustainable biofuel production systems. *Renewable and Sustainable Energy Reviews*, *107*(February), 250–263. https://doi.org/10.1016/j.rser.2019.03.005

Craven, R. J., & Lencki, R. W. (2011a). Binary phase behavior of diacid 1,3-diacylglycerols. *Journal of the American Oil Chemists' Society*, *88*(8), 1125–1134. https://doi.org/10.1007/s11746-011-1777-0

Craven, R. J., & Lencki, R. W. (2011b). Crystallization and polymorphism of 1,3-acyl-palmitoyl-rac-glycerols. *Journal of the American Oil Chemists' Society*, *88*(8), 1113–1123. https://doi.org/10.1007/s11746-011-1769-0

Cunha, C. L., Luna, A. S., Oliveira, R. C. G., Xavier, G. M., Paredes, M. L. L., & Torres, A. R. (2017). Predicting the properties of biodiesel and its blends using mid-FT-IR spectroscopy and first-order multivariate calibration. *Fuel*, *204*, 185–194. https://doi.org/10.1016/j.fuel.2017.05.057

Cunha, C. L., Torres, A. R., & Luna, A. S. (2020). Multivariate regression models obtained from near-infrared spectroscopy data for prediction of the physical properties of biodiesel and its blends. *Fuel*, *261*, 116344. https://doi.org/10.1016/j.fuel.2019.116344

de Matos, F. C., da Costa, M. C., de Almeida Meirelles, A. J., & Batista, E. A. C. (2015). Binary solid-liquid equilibrium systems containing fatty acids, fatty alcohols and triolein by differential scanning calorimetry. *Fluid Phase Equilibria*, *404*(110), 1–8. https://doi.org/10.1016/j.fluid.2015.06.015

de Matos, F. C., da Costa, M. C., Meirelles, A. J. de A., & Batista, E. A. C. (2016). Binary solid-liquid equilibrium systems containing fatty acids, fatty alcohols and trilaurin by differential scanning calorimetry. *Fluid Phase Equilibria*, *423*, 74–83. https://doi.org/10.1016/j.fluid.2016.04.008

Dunn, R. O. (2012). Effects of High-Melting Methyl Esters on Crystallization Properties of Fatty Acid Methyl Ester Mixtures. *Transactions of the ASABE*, *55*(2), 637–646. https://doi.org/10.13031/2013.41365

Dunn, R. O., & Bagby, M. O. (1995). Low-temperature properties of triglyceride-based diesel fuels: Transesterified methyl esters and petroleum middle distillate/ester blends. *Journal of the American Oil Chemists' Society*, *72*(8), 895–904. https://doi.org/10.1007/BF02542067

Dunn, Robert O. (1999). Thermal analysis of alternative diesel fuels from vegetable oils. *JAOCS, Journal of the American Oil Chemists' Society*, *76*(1), 109–115. https://doi.org/10.1007/s11746-999-0056-9

Dunn, Robert O. (2008). Crystallization behavior of fatty acid methyl esters. *Journal of the American Oil Chemists' Society*, *85*(10), 961–972. https://doi.org/10.1007/s11746-008-1279-x

Dunn, Robert O. (2009). Effects of minor constituents on cold flow properties and performance of biodiesel. *Progress in Energy and Combustion Science, 35*(6), 481–489. https://doi.org/10.1016/j.pecs.2009.07.002

Dunn, Robert O. (2012). Effects of monoacylglycerols on the cold flow properties of biodiesel. *Journal of the American Oil Chemists' Society, 89*(8), 1509–1520. https://doi.org/10.1007/s11746-012-2045-7

Dunn, Robert O. (2015). Cold flow properties of biodiesel: A guide to getting an accurate analysis. *Biofuels, 6*(1–2), 115–128. https://doi.org/10.1080/17597269.2015.1057791

Dunn, Robert O. (2018). Correlating the Cloud Point of Biodiesel to the Concentration and Melting Properties of the Component Fatty Acid Methyl Esters. *Energy and Fuels, 32*(1), 455–464. https://doi.org/10.1021/acs.energyfuels.7b02935

Dunn, Robert O. (2020). Correlating the Cold Filter Plugging Point to Concentration and Melting Properties of Fatty Acid Methyl Ester (Biodiesel) Admixtures. *Energy and Fuels*, *34*(1), 501–515. https://doi.org/10.1021/acs.energyfuels.9b03311

Echim, C., Maes, J., & Greyt, W. De. (2012). Improvement of cold filter plugging point of biodiesel from alternative feedstocks. *Fuel, 93,* 642–648. https://doi.org/10.1016/j.fuel.2011.11.036

Engström, L. (1992). Triglyceride systems forming molecular compounds. *Eur. J. Lipid Sci. Tech., 94*(5), 173–181. http://onlinelibrary.wiley.com/doi/10.1002/lipi.19920940503/abstract

Etter, M. C. (1990). Encoding and decoding hydrogen-bond patterns of organic compounds. *Accounts of Chemical Research, 23*(4), 120–126. https://doi.org/10.1021/ar00172a005

Fischer, E., Bergmann, M., & Barwind, H. (1920). Neue synthese von a-monoglyceriden. *Berichte Der Deutschen Chemischen Gesellschaft*, *53,* 1589–1605.

Foubert, I., Dewettinck, K., Van de Walle, D., Dijkstra, A. J., & Quinn, P. J. (2007). Physical properties: Structural and physical characteristics. In F. D. Gunstone, J. L. Harwood, & A. J. Dijkstra (Eds.), *The Lipid Handbook with CD-ROM* (3rd ed.). CRC Press. https://doi.org/10.1201/9781420009675

Fredenslund, A., Jones, R. L., & Prausnitz, J. M. (1975). Group-contribution estimation of activity coefficients in nonideal liquid mixtures. *AIChE Journal*, *21*(6), 1086–

1099. https://doi.org/10.1002/aic.690210607

Gmehling, J., Li, J., & Schiller, M. (1993). A modified UNIFAC model. 2. Present parameter matrix and results for different thermodynamic properties. *Industrial and Engineering Chemistry Research*, *32*(1), 178–193. https://doi.org/10.1021/ie00013a024

Gunstone, F. D., Harwood, J. L., & Albert J. Dijkstra. (2007). The Lipid Handbook with CD-ROM. In *CRC Press* (3rd ed.). CRC Press. https://doi.org/10.1201/9781420009675

Heino, E. L. (1987). Determination of cloud point for petroleum middle distillates by differential scanning calorimetry. *Thermochimica Acta*, *114*, 125–130. https://doi.org/10.1016/0040-6031(87)80250-2

Hoekman, S. K., Broch, A., Robbins, C., Ceniceros, E., & Natarajan, M. (2012). Review of biodiesel composition, properties, and specifications. *Renewable and Sustainable Energy Reviews*, *16*(1), 143–169. https://doi.org/10.1016/j.rser.2011.07.143

Hohne, G. W. H., Hemminger, W. F., & Flammersheim, H.-J. (2003). *Differential Scanning Calorimetry* (2nd ed.). Springer-Verlag Berlin Heidelberg. https://doi.org/10.1007/978-3-662-06710-9

Holmgren, A., Lindblom, G., & Johansson, L. B. . (1988). Intramolecular hydrogen bonding in a monoglyceride lipid studied by Fourier transform infrared spectroscopy. *Journal of Physical Chemistry*, *92*(20), 5639–5642. https://doi.org/10.1021/j100331a020

Humas EBTKE. (2019). *Standar dan Mutu (Spesifikasi) Bahan Bakar Nabati (Biofuel) Jenis Biodiesel Sebagai Bahan Bakar Lain yang Dipasarkan di Dalam Negeri*. Ministry of Energy, Resources, and Minerals of Indonesia. https://ebtke.esdm.go.id/post/2019/11/13/2394/standar.dan.mutu.spesifikasi.bahan.bakar.nabati.biofuel.jenis.biodiesel.sebagai.bahan.bakar.lain.yang.dipasarkan.di.dalam.negeri

IEA. (2019). *Renewables 2019*. https://www.iea.org/reports/renewables-2019

Imahara, H., Minami, E., & Saka, S. (2006). Thermodynamic study on cloud point of biodiesel with its fatty acid composition. *Fuel*, *85*(12–13), 1666–1670. https://doi.org/10.1016/j.fuel.2006.03.003

Inoue, T., Hisatsugu, Y., Yamamoto, R., & Suzuki, M. (2004). Solid-liquid phase behavior of binary fatty acid mixtures: 1. Oleic acid/stearic acid and oleic acid/behenic acid mixtures. *Chemistry and Physics of Lipids*, *127*(2), 143–152. https://doi.org/10.1016/j.chemphyslip.2003.09.014

Kellens, M., Meeussen, W., & Reynaers, H. (1990). Crystallization and phase transition studies of tripalmitin. *Chemistry and Physics of Lipids*, *55*(2), 163–178. https://doi.org/10.1016/0009-3084(90)90077-5

King, A. M., & Garner, W. E. (1936). The melting points of long-chain carbon compounds. *J Chem Soc*, 1368–1372. https://doi.org/https://doi.org/10.1039/JR9360001368

Knothe, G., & Dunn, R. O. (2009). A comprehensive evaluation of the melting points of fatty acids and esters determined by differential scanning calorimetry. *Journal of the American Oil Chemists' Society*, *86*(9), 843–856. https://doi.org/10.1007/s11746-009-1423-2

Leng, L., Li, W., Li, H., Jiang, S., & Zhou, W. (2020). Cold Flow Properties of Biodiesel and the Improvement Methods: A Review. *Energy and Fuels*, *34*(9), 10364–10383. https://doi.org/10.1021/acs.energyfuels.0c01912

Lopes, J. C. A., Boros, L., Kráhenbúhl, M. A., Meirelles, A. J. A., Daridon, J. L., Pauly, J., Marrucho, I. M., & Coutinho, J. A. P. (2008). Prediction of cloud points of biodiesel. *Energy and Fuels*, *22*(2), 747–752. https://doi.org/10.1021/ef700436d

Lutton, E. S. (1971). The phases of saturated 1-monoglycerides C14-C22. *Journal of the American Oil Chemists Society*, *48*(12), 778–781. https://doi.org/10.1007/BF02609279

Lutton, E. S., & Jackson, F. L. (1967). Binary systems with monoglycerides. *Journal of the American Oil Chemists' Society*, *44*(6), 357–358. https://doi.org/10.1007/BF02582659

Mahlia, T. M. I., Syazmi, Z. A. H. S., Mofijur, M., Abas, A. E. P., Bilad, M. R., Ong, H. C., & Silitonga, A. S. (2020). Patent landscape review on biodiesel production: Technology updates. *Renewable and Sustainable Energy Reviews*, *118*(April 2019), 109526. https://doi.org/10.1016/j.rser.2019.109526

Malkin, T., & Shurbagy, M. R. E. (1936). An x-ray and thermal examination of the glycerides. Part II. The alpha-monoglycerides. *J Chem Soc*, *1936*, 1628–1634.

Maruyama, T., Niiya, I., Imamura, M., Okada, M., & Matsumoto, T. (1973). Study on polymorphism of monoglyceride. II. Thermodynamic considerations on transition. *Journal of Japan Oil Chemists' Society*, *22*(2), 19–22.

Maruyama, T., Niiya, I., Imamura, M., Okada, M., Matsumoto, T., Horisawa, M., & Matsumoto, T. (1971). Study on polymorphism of monoglyceride. I. Transition of crystal modification of 1-monolaurin, 1-monomyristin, 1-monopalmitin, and 1-monostearin. *Journal of Japan Oil Chemists' Society*, *20*(7), 11–18. https://doi.org/https://doi.org/10.5650/jos1956.20.395

Maruyama, T., Niiya, I., Okada, M., & Matsumoto, T. (1978). Studies on polymorphism of monoglycerides. VIII. Phase behavior of binary monoglycerides systems. *Journal of Japan Oil Chemists' Society*, *843*, 26–31.

Meher, L. C., Dharmagadda, V. S. S., & Naik, S. N. (2006). Optimization of alkali-catalyzed transesterification of Pongamia pinnata oil for production of biodiesel. *Bioresource Technology*, *97*(12), 1392–1397. https://doi.org/10.1016/j.biortech.2005.07.003

Ministry of Agriculture Livestock and Food Supply of Brazil. (2015). *Uses for Biodiesel in Brazil and Globally* (1st ed.). Biblioteca Nacional de Agricultura – BINAGRI Brasil. file:///C:/Users/Latifa Seniorita/Downloads/uses-for-biodiesel-in-brazil-and-globally.pdf

Mohanan, A., Darling, B., Bouzidi, L., & Narine, S. S. (2015). Mitigating crystallization of saturated FAMEs (fatty acid methyl esters) in biodiesel: 3. The binary phase behavior of 1,3-dioleoyl-2-palmitoyl glycerol - Methyl palmitate - A multi-length scale structural elucidation of mechanism responsible for inhibiti. *Energy*, *86*, 500–513. https://doi.org/10.1016/j.energy.2015.04.011

Moser, B. R. (2008). Influence of blending canola, palm, soybean, and sunflower oil methyl esters on fuel properties of biodiesel. *Energy and Fuels*, *22*(6), 4301–4306. https://doi.org/10.1021/ef800588x

Moser, B. R. (2014). Impact of fatty ester composition on low temperature properties of biodiesel-petroleum diesel blends. *Fuel*, *115*, 500–506. https://doi.org/10.1016/j.fuel.2013.07.075

Mostafaei, M. (2018). Prediction of biodiesel fuel properties from its fatty acids composition using ANFIS approach. *Fuel*, *229*(February), 227–234. https://doi.org/10.1016/j.fuel.2018.04.148

Palou, A., Miró, A., Blanco, M., Larraz, R., Gómez, J. F., Martínez, T., González, J. M., & Alcalà, M. (2017). Calibration sets selection strategy for the construction of robust PLS models for prediction of biodiesel/diesel blends physico-chemical properties using NIR spectroscopy. *Spectrochimica Acta - Part A: Molecular and Biomolecular Spectroscopy*, *180*, 119–126. https://doi.org/10.1016/j.saa.2017.03.008

Park, J. Y., Kim, D. K., Lee, J. P., Park, S. C., Kim, Y. J., & Lee, J. S. (2008). Blending effects of biodiesels on oxidation stability and low temperature flow properties. *Bioresource Technology*, *99*(5), 1196–1203. https://doi.org/10.1016/j.biortech.2007.02.017

Paryanto, I., Prakoso, T., & Gozan, M. (2019). Determination of the upper limit of monoglyceride content in biodiesel for B30 implementation based on the measurement of the precipitate in a Biodiesel–Petrodiesel fuel blend (BXX). *Fuel*, *258*, 116104. https://doi.org/10.1016/j.fuel.2019.116104

Pereira, E., Meirelles, A. J. A., & Maximo, G. J. (2020). Predictive models for physical properties of fats, oils, and biodiesel fuels. *Fluid Phase Equilibria*, *508*, 112440. https://doi.org/10.1016/j.fluid.2019.112440

Prausnitz, J. M., Lichtenthaler, R. N., & de Azevedo, E. G. (1999). *Molecular thermodynamics of fluid-phase equilibria* (N. R. Amundson (ed.); 3rd ed.). Prentice Hall PTR. https://doi.org/10.1016/0021-9614(70)90078-9

Rahmanulloh, A., & McDonald, G. (2020). *Biofuels Annual 2020*. https://apps.fas.usda.gov/newgainapi/api/Report/DownloadReportByFileName?fileName=Biofuels Annual_Jakarta_Indonesia_06-22-2020

Ramalho, E. F. S. M., Carvalho Filho, J. R., Albuquerque, A. R., De Oliveira, S. F., Cavalcanti, E. H. S., Stragevitch, L., Santos, I. M. G., & Souza, A. G. (2012). Low temperature behavior of poultry fat biodiesel:diesel blends. *Fuel*, *93*, 601–605. https://doi.org/10.1016/j.fuel.2011.10.051

Ramos, M. J., Fernández, C. M., Casas, A., Rodríguez, L., & Pérez, Á. (2009). Influence of fatty acid composition of raw materials on biodiesel properties. *Bioresource Technology*, *100*(1), 261–268. https://doi.org/10.1016/j.biortech.2008.06.039

Razavi, R., Bemani, A., Baghban, A., Mohammadi, A. H., & Habibzadeh, S. (2019). An insight into the estimation of fatty acid methyl ester based biodiesel properties using a LSSVM model. *Fuel*, *243*(June 2018), 133–141.

https://doi.org/10.1016/j.fuel.2019.01.077

REN21. (2017). *Renewables 2017 Global Status Report*. https://www.ren21.net/gsr-2017/

REN21. (2020). *Renewables 2020 Global Status Report*. https://www.ren21.net/reports/global-status-report/

Renon, H., & Prausnitz, J. M. (1968). Local compositions in thermodynamic excess functions for liquid mixtures. *AIChE Journal*, *14*(1), 135–144. https://doi.org/10.1002/aic.690140124

Robustillo, M. D., Barbosa, D. F., Meirelles, A. J. de A., & Pessoa Filho, P. de A. (2014). Solid-liquid equilibrium of binary and ternary mixtures containing ethyl oleate, ethyl myristate and ethyl stearate. *Fluid Phase Equilibria*, *370*, 85–94. https://doi.org/10.1016/j.fluid.2014.03.001

Sarin, A., Arora, R., Singh, N. P., Sarin, R., Malhotra, R. K., & Kundu, K. (2009). Effect of blends of Palm-Jatropha-Pongamia biodiesels on cloud point and pour point. *Energy*, *34*(11), 2016–2021. https://doi.org/10.1016/j.energy.2009.08.017

Sarin, A., Arora, R., Singh, N. P., Sarin, R., Malhotra, R. K., & Sarin, S. (2010). Blends of biodiesels synthesized from non-edible and edible oils: Effects on the cold filter plugging point. *Energy and Fuels*, *24*(3), 1996–2001. https://doi.org/10.1021/ef901131m

Sato, K., & Kuroda, T. (1987). Kinetics of melt crystallization and transformation of tripalmitin polymorphs. *Journal of the American Oil Chemists' Society*, *64*(1), 124–127. https://doi.org/10.1007/BF02546266

Serrano, M., Oliveros, R., Sánchez, M., Moraschini, A., Martínez, M., & Aracil, J. (2014). Influence of blending vegetable oil methyl esters on biodiesel fuel properties: Oxidative stability and cold flow properties. *Energy*, *65*, 109–115. https://doi.org/10.1016/j.energy.2013.11.072

Shannon, R. J., Fenerty, J., Hamilton, R. J., & Padley, F. B. (1992). The polymorphism of diglycerides. *Journal of the Science of Food and Agriculture*, *60*(4), 405–417. https://doi.org/10.1002/jsfa.2740600402

Shrestha, L. K., Sato, T., Acharya, D. P., Iwanaga, T., Aramaki, K., & Kunieda, H. (2006). Phase behavior of monoglycerol fatty acid esters in nonpolar oils: Reverse rodlike micelles at elevated temperatures. *Journal of Physical Chemistry B*, *110*(25), 12266–

12273. https://doi.org/10.1021/jp060587p

Sia, C. B., Kansendo, J., Tan, Y. H., & Lee, K. T. (2020). Evaluation on biodiesel cold flow properties, oxidative stability and enhancement. *Biocatalysis and Agricultural Biotechnology*, *24*, 101514. https://doi.org/10.1016/j.bcab.2020.101514

Sierra-Cantor, J. F., & Guerrero-Fajardo, C. A. (2017). Methods for improving the cold flow properties of biodiesel with high saturated fatty acids content: A review. *Renewable and Sustainable Energy Reviews*, *72*(January), 774–790. https://doi.org/10.1016/j.rser.2017.01.077

Sugami, Y., Yoshidomi, S., Minami, E., Shisa, N., Hayashi, H., & Saka, S. (2017). The effect of monoglyceride polymorphism on cold-flow properties of biodiesel model fuel. *Journal of the American Oil Chemists' Society*, *94*(8), 1095–1100. https://doi.org/10.1007/s11746-017-3016-9

Tang, H., De Guzman, R. C., Salley, S. O., & Ng, K. Y. S. (2008). Formation of insolubles in palm oil-, yellow grease-, and soybean oil-based biodiesel blends after cold soaking at 4 °c. *Journal of the American Oil Chemists' Society*, *85*(12), 1173–1182. https://doi.org/10.1007/s11746-008-1303-1

Tang, H., Salley, S. O., & Simon Ng, K. Y. (2008). Fuel properties and precipitate formation at low temperature in soy-, cottonseed-, and poultry fat-based biodiesel blends. *Fuel*, *87*(13–14), 3006–3017. https://doi.org/10.1016/j.fuel.2008.04.030

Timms, R. E. (1984). Phase behaviour of fats and their mixtures. *Progress in Lipid Research*, *23*(1), 1–38. https://doi.org/10.1016/0163-7827(84)90004-3

Wilson, G. M. (1964). Vapor-Liquid Equilibrium. XI. A New Expression for the Excess Free Energy of Mixing. *Journal of the American Chemical Society*, *86*(2), 127–130. https://doi.org/10.1021/ja01056a002

Xu, Y., & Dong, C. (2017). Phase behavior of binary mixtures of three different 1,3-diacylglycerols. *European Journal of Lipid Science and Technology*, *119*(9), 1–13. https://doi.org/10.1002/ejlt.201600497

Yoshidomi, S., Sugami, Y., Minami, E., Shisa, N., Hayashi, H., & Saka, S. (2017). Predicting solid-liquid equilibrium of fatty acid methyl ester and monoacylglycerol mixtures as biodiesel model fuels. *Journal of the American Oil Chemists Society*, *94*(8), 1087–1094. https://doi.org/10.1007/s11746-017-3029-4

Yu, L., Lee, I., Hammond, E. G., Johnson, L. A., & Van Gerpen, J. H. (1998). The influence of trace components on the melting point of methyl soyate. *Journal of the American Oil Chemists' Society*, *75*(12), 1821–1824. https://doi.org/10.1007/s11746-998-0337-8

Yuan, M. H., Chen, Y. H., Chen, J. H., & Luo, Y. M. (2017). Dependence of cold filter plugging point on saturated fatty acid profile of biodiesel blends derived from different feedstocks. *Fuel*, *195*, 59–68. https://doi.org/10.1016/j.fuel.2017.01.054

Zhang, L., Ueno, S., & Sato, K. (2018). Binary phase behavior of saturated-unsaturated mixed-acid triacylglycerols—A review. *Journal of Oleo Science*, *67*(6), 679–687. https://doi.org/10.5650/jos.ess17263

Živković, S. B., Veljković, M. V., Banković-Ilić, I. B., Krstić, I. M., Konstantinović, S. S., Ilić, S. B., Avramović, J. M., Stamenković, O. S., & Veljković, V. B. (2017). Technological, technical, economic, environmental, social, human health risk, toxicological and policy considerations of biodiesel production and use. *Renewable and Sustainable Energy Reviews*, *79* (February), 222–247. https://doi.org/10.1016/j.rser.2017.05.048

Acknowledgments

I acknowledge the financial support by the Ministry of Education, Culture, Sports, Science, and Technology (MEXT) of Japan, which made this five and half years of journey possible. I am also grateful to Toyota Motor Corp. for valuable experience on the joint research and research financial support from 2016-2018.

I would like to express my deepest gratitude to Professor Haruo Kawamoto and Professor Emeritus Shiro Saka of Energy Ecosystems Laboratory. First and foremost, for trusting me to carry out this research along with numerous supports and advice. Their complete dedication to work has been an inspiration to challenge me on this research. I feel fortunate to have them as my advisors and always cherish the moment we shared.

I am hugely indebted to Assistant Professor Eiji Minami for his kindness, patience, advice, and suggestions. It was a pleasure to have the many chances for exploring various thoughts and ideas, although as small as they were. He also provided continuous supports through critical stages and patiently guided me on how to produce valuable reports.

In addition, a thank you to Professor Keiichi Ishihara and Professor Hiroshi Kawanabe with their advice that enriched the discussion in this dissertation. I would also like to express my gratitude to Dr. Tirto Prakoso for his practical and political insight biodiesel utilization in Indonesia. Every discussion was especially interesting and insightful.

My heartful appreciation for the members of the Energy Ecosystems laboratory, especially for senpais, co-workers, and life advisors: Dr. Fadjar Goembira, Dr. Masatsugu Takada, Dr. Chen Qu, Dr. Yuitsu Sugami, Dr. Kiky Sembiring, Dr. Yuanyuan Zhao, Shinichiro Yoshidomi, Eka Triwahyuni, Rui Fang, Luthfiana Hidayati, Wang Jiaqi, and Resi Ginting for their continues supports and patiently accompanied me through brainstorming sessions and laboratory works. My appreciation extends to Ms. Rie Nakanishi for all the document works.

Special thanks to my best roommate in the whole world Aya Kaia, and brainstorming mate Widha Kusumaningdyah, with whom I charge my social energy instead of depleting it. I am also thankful for all members of Shirakawa Mager who proudly sail and suffer permanent head damage (PhD) life; I thank you for energizing this journey by meaningful, heated, but at the same time, playful random talks. Luckily

COVID-19 lets us work and connect from anywhere easier now with online meeting rooms available, but nothing can replace "duduk leyeh-leyeh di rumah tante selepas lebaran". Let us meet again someday, in a world with a better condition.

For most importantly, my beloved family in Indonesia, and Tedy, who always be my supporting system, shower me with their love, trust, and encouragement no matter what (my work is probably something unimaginable for them); no words may describe how grateful I am to have you.

Latifa Seniorita

List of Publications

Original Article

1. L. Seniorita, E. Minami, Y. Yazawa, H. Hayashi, S. Saka (2019) Differential scanning calorimetric study of solidification behavior of monoacylglycerols to investigate the cold-flow properties of biodiesel, *J. Am. Oil Chem. Soc.*, **96** (9): 979-987 DOI: 10.1002/aocs.12267
2. L. Seniorita, E. Minami, H. Kawamoto (2020) Development and evaluation of thermodynamic models for predicting cold flow properties of biodiesel, *J. Adv. Res. Fluid Mech. Therm. Sci.*, **76** (3): 117-125. DOI: 10.37934/arfmts.76.3.117125
3. L. Seniorita, E. Minami, H. Kawamoto (2021) Solidification behavior of acylglycerols in fatty acid methyl esters and effects on the cold flow properties of biodiesel, *J. Am. Oil Chem. Soc.*, 1-9 DOI: 10.1002/aocs.12492 (in press)
4. L. Seniorita, E. Minami, H. Kawamoto (2021) Solid-liquid phase behavior of binary mixtures of acylglycerols, *Eur. J. Lipid Sci. Technol.* (under review)
5. L. Seniorita, E. Minami, H. Kawamoto (2021) A method for estimating acylglycerols effect to biodiesel cold flow properties by using thermodynamic models (in preparation)
6. L. Seniorita, R. Fang, E. Minami, H. Kawamoto (2021) Monoacylglycerol solidification in alkane and aromatic compounds for predicting cold flow properties of biodiesel and fossil diesel blend fuels (in preparation)

Review article

1. E. Minami, L. Seniorita (2021) バイオディーゼル低温流動性の熱力学的研究 (Thermodynamic study of cold flow properties of biodiesel), 石油学会情報誌 Petrotech (in press).

International Conference

1. L. Seniorita, E. Minami, H. Kawamoto, N. Shisa, Y. Yazawa, H. Hayashi, S. Saka (2018) Thermodynamic study of monoglycerides for predicting cold flow properties of biodiesel, Oral, The 1st Joint International Symposium between Kyoto University and Indian Institute of Science, December 3-5, Bengalore, India, O19.
2. L. Seniorita, E. Minami, H. Kawamoto (2020) Development and evaluation of thermodynamic models for predicting cold flow properties of biodiesel, Oral, International e-Conference on Green and Renewable Energy 2020 (GREEN2020), August 18-19, Sarawak, Malaysia, O06.
3. L. Seniorita, E. Minami, H. Kawamoto (2020) Developing thermodynamic models for predicting cold flow properties of biodiesel: Solidification behavior of acylglycerols, Oral, 4th Zhejiang-Kyoto-Ajou Joint Symposium on Energy Science (online), Zhejiang, China, pp. 17, O04.
4. L. Seniorita, S.M. Dumlao, K.K.K. Murthy, C. Qu, J. Cravioto, H. Ohgaki (2020) Study on the influence of gender roles on appliance purchasing behavior of urban middle class in developing nations, Oral, 4th Zhejiang-Kyoto-Ajou Joint Symposium on Energy Science, Zhejiang, China, pp. 16, O03.

National Conference

1. L. Seniorita, E. Minami, N. Shisa, Y. Yazawa, H. Hayashi, S. Saka (2018) Solid-liquid equilibrium of monoglycerides for predicting cold flow properties of biodiesel, Oral, The 27th Annual Meeting of the Japan Energy Society, 3-1-3, pp. 76-77, August 8-9, Tokyo.
2. L. Seniorita, E. Minami, Y. Yazawa, H. Hayashi, S. Saka (2019) Effect of diglycerides on biodiesel cold-flow properties, The 28th Annual Meeting of the Japan Energy Society, Oral, 3-7-2, pp. 114-115, August 7-8, Osaka.
3. Rui Fang, L. Seniorita, E. Minami, Y. Yazawa, H. Hayashi, S. Saka (2019) Effective parameters on cold-flow properties of biodiesel and fossil diesel blends, Poster, The 28th Annual Meeting of the Japan Energy Society, P-3-10, pp. 264-265, August 7-8, Osaka.

4. L. Seniorita, E. Minami, H. Kawamoto (2019) Predicting cold flow properties of biodiesel by thermodynamic models, The 58th Annual Meeting of the Japan Oil Chemists’ Society, Oral, 1D-18, p. 144, September 24-26, Tokyo.

Appendix

A1. Pure component properties

Name	Abbrev.	Crystal type	Melting point (°C)	Enthalpy of fusion (kJ/mol)	Number of UNIFAC functional group									
					CH_3	CH_2	CH	CH=CH	ACH	$ACCH_3$	AC	OH(p)	OH(s)	CH_2COO
Fatty acid methyl ester (FAME)														
Methyl caprilate	FAME10:0	-	-14.0	27.0	2	7	-	-	-	-	-	-	-	1
Methyl laurate	FAME12:0	-	4.5	36.4	2	9	-	-	-	-	-	-	-	1
Methyl myristate	FAME14:0	-	18.1	53.0	2	11	-	-	-	-	-	-	-	1
Methyl palmitate	FAME16:0	-	29.8	60.4	2	13	-	-	-	-	-	-	-	1
Methyl stearate	FAME18:0	-	38.4	62.2	2	15	-	-	-	-	-	-	-	1
Methyl oleate	FAME18:1	-	-20.7	41.6	2	13	-	1	-	-	-	-	-	1
Monoacylglycerol (MAG)														
1-Monocaprin	MAG10:0	α	24.3	16.9	1	9	1	-	-	-	-	1	1	1
		β′	44.2	23.9										
		β	54.3	41.5										
1-Monolaurin	MAG12:0	α	44.8	22.3	1	11	1	-	-	-	-	1	1	1
		β′	59.5	30.0										
		β	62.3	38.0										

Name	Abbrev.	Crystal type	Melting point (°C)	Enthalpy of fusion (kJ/mol)	Number of UNIFAC functional group									
					CH_3	CH_2	CH	CH=CH	ACH	$ACCH_3$	AC	OH(p)	OH(s)	CH_2COO
1-Monomyristin	MAG14:0	α	56.7	26.9	1	13	1	-	-	-	-	1	1	1
		β′	67.5	39.8										
		β	68.7	50.6										
1-Monopalmitin	MAG16:0	α	66.4	34.1	1	15	1	-	-	-	-	1	1	1
		β′	72.7	49.8										
		β	75.7	63.6										
1-Monostearin	MAG18:0	α	74.2	39.2	1	17	1	-	-	-	-	1	1	1
		β′	78.0	65.7										
		β	81.6	83.5										
1-Monoolein	MAG18:1	α	25.0	20.0	1	15	1	1	-	-	-	1	1	1
		β′	30.1	30.0										
		β	35.0	49.4										
Diacylglycerol (DAG)														
1,3-Dilaurin	DAG12:0	β_1	57.3	79.2	2	20	1	-	-	-	-	1	-	2
		β_2	55.4	79.0										
1,3-Dipalmitin	DAG16:0	β_1	73.4	111.4	2	28	1	-	-	-	-	1	-	2
		β_2	71.1	100.6										

Name	Abbrev.	Crystal type	Melting point (°C)	Enthalpy of fusion (kJ/mol)	Number of UNIFAC functional group									
					CH_3	CH_2	CH	CH=CH	ACH	$ACCH_3$	AC	OH(p)	OH(s)	CH_2COO
1,3-Distearin	DAG18:0	β_1	79.5	129.9	2	32	1	-	-	-	-	1	-	2
		β_2	76.8	126.7										
1,3-Diolein	DAG18:1	β_1	25.8	88.4	2	28	1	2	-	-	-	1	-	2
		β_2	24.7	88.0										
Triacylglycerol (TAG)														
Trilaurin	TAG12:0	β	44.5	118.4	3	29	1	-	-	-	-	-	-	3
Tripalmitin	TAG16:0	β	63.3	132.4	3	41	1	-	-	-	-	-	-	3
Tristearin	TAG18:0	β	73.8	181.1	3	47	1	-	-	-	-	-	-	3
Hydrocarbon														
n-Dodecane	n-C12	-	-9.6	36.8	2	10	-	-	-	-	-	-	-	-
n-Nonadecane	n-C19	-	32.0	42.7	2	17	-	-	-	-	-	-	-	-
Toluene	-	-	-95.0	6.6	-	-	-	-	5	1		-	-	-
1-Methyl-naphthalene	-	-	-22.0	9.7	-	-	-	-	7	1	2	-	-	-

A2. Calculation of thermodynamic model

The thermodynamic models were developed in the Visual Basic Applications of Microsoft Visual Basic for Applications in Excel (Microsoft Corp., Redmond, WA). The following codes are an example for calculating liquidus temperature of binary mixture by using the NSS model.

```
Dim temp_upper As Double      'Upper temperature on the calculation by bisection method, K
    Dim temp_lower As Double      'Lower temperature on the calculation by bisection method, K
    Dim temp As Double            'Temperature of the current calculation, K
    Dim temp_former As Double     'Temperature of the former calculation, K
    Dim Tm As Double              'Melting point, K

    Dim q(2) As Double, F(2) As Double, r(2) As Double, V(2) As Double, Vdash(2) As Double
'qi, Fi, ri, Vi and V'i
    Dim ln_ganma(2) As Double, ln_ganma_c(2) As Double, ln_ganma_r(2) As Double, psi(85,
85) As Double      'lnγi, lnγc, lnγr, and ψmn
    Dim Xm(2, 85) As Double: Erase Xm             'Xm
    Dim theta(2, 85) As Double: Erase theta       'θm
    Dim sig_thetaN_psiNM(2, 85) As Double: Erase sig_thetaN_psiNM      '∑n θn ψmn
    Dim thetaM_by_sig_thetaN_psiNM(2, 85) As Double: Erase thetaM_by_sig_thetaN_psiNM
'∑m/∑n θn ψmn
    Dim sig_thetaM_by_sig_thetaN_psiNM(2, 85) As Double: Erase
sig_thetaM_by_sig_thetaN_psiNM     '∑m (θm ψkm/∑n θn ψmn)
    Dim ln_ganma_k(2, 85) As Double       'lnΓk

    Dim R_const As Double: R_const = 8.3144598      'Gas constant
    Dim Solidification(2) As Double               'Solidification temperature of i, °C
    Dim SLE_deviation(2) As Double                'Deviation in SLE calculation
    Dim Temp_deviation(2) As Double               'Deviation of temperature in SLE calculation

    'Detect the lower melting point among the two components, and store it in meltingpoint(0)
    If meltingpoint(1) < meltingpoint(2) Then
        meltingpoint(0) = meltingpoint(1)
    Else
        meltingpoint(0) = meltingpoint(2)
    End If
```

```
‘Calculation of activity coefficient by modified UNIFAC (Dortmund): γiC (unaffected by temperature change)
    'Calculation of q(i) and r(i)
    For i = 1 To Number_comp
        q(i) = 0
        r(i) = 0
        For j = 1 To Number_groups
            q(i) = q(i) + Nu_i_k(i, j) * Qk(j)
            r(i) = r(i) + Nu_i_k(i, j) * Rk(j)
        Next
    Next

    'Set initial values
    n = 0
    molefraction(1) = delta_x
    molefraction(2) = 1# - molefraction(1)

    'Draw a table of SLE calculation result
    Set Rng1 = Cells(19 + Number_comp + 4 * Number_groups, 1) 'Cell's address for the table of SLE result
    Rng1.Offset(0, 0).Value = "The result of SLE calculation"
    Rng1.Offset(1, 0).Value = "x of " & Component(1)
    Rng1.Offset(1, 1).Value = "Ts, °C
    Rng1.Offset(1, 2).Value = "Solidified prod. A"
    Rng1.Offset(1, 3).Value = "γ of A at Ts"
    Rng1.Offset(1, 4).Value = "Dev. in SLE"
    Rng1.Offset(1, 5).Value = "Dev. in temp."
    Rng1.Offset(2, 0).Value = 0
    Rng1.Offset(2, 1).Value = meltingpoint(2)
    Rng1.Offset(2, 2).Value = Component(2)
    Range(Cells(20 + Number_comp + 4 * Number_groups, 1), Cells(20 + Number_comp + 4 * Number_groups, 5)).ShrinkToFit = True

    'Execute a step-by-step calculation by mole fracton x
    Do While molefraction(1) < 1

        'Calculation of F(i),V(i) and Vdash(i)
        For i = 1 To Number_comp
            F(i) = 0
```

```
        V(i) = 0
        Vdash(i) = 0
        For j = 1 To Number_comp
            F(i) = F(i) + molefraction(j) * q(j)
            V(i) = V(i) + molefraction(j) * r(j)
            Vdash(i) = Vdash(i) + molefraction(j) * r(j) ^ (3# / 4#)
        Next
        F(i) = q(i) / F(i)
        V(i) = r(i) / V(i)
        Vdash(i) = r(i) ^ (3# / 4#) / Vdash(i)
    Next

    'Calculation of ln_ganma_c
    For i = 1 To Number_comp
        ln_ganma_c(i) = 1 - Vdash(i) + Log(Vdash(i)) - 5 * q(i) * (1 - V(i) / F(i) + Log(V(i) / F(i)))
    Next

    'Calculation of Xm for pure component i
    For i = 1 To Number_comp
        Xm(i, 0) = 0
        For j = 1 To Number_groups
            Xm(i, 0) = Xm(i, 0) + Nu_i_k(i, j)    'Calculate the sum of groups for each component i, and store it in Xm(i,0)
        Next
    Next

    For i = 1 To Number_comp
        For j = 1 To Number_groups
            Xm(i, j) = Nu_i_k(i, j) / Xm(i, 0)    'Calculate the Xm of each group j for pure component i
        Next
    Next

    'Calculation of Xm for the mixture
    Xm(0, 0) = 0
    For i = 1 To Number_comp
        For j = 1 To Number_groups
            Xm(0, 0) = Xm(0, 0) + Nu_i_k(i, j) * molefraction(i)  'Calculation of the sum of Nu * molefraction
```

```
        Next
    Next

    For j = 1 To Number_groups
        Xm(0, j) = 0
        For i = 1 To Number_comp
            Xm(0, j) = Xm(0, j) + Nu_i_k(i, j) * molefraction(i)  'Calculate the sum of Nu * fraction for each groups j, and store it in Xm(0,j)
        Next
        Xm(0, j) = Xm(0, j) / Xm(0, 0) 'Calculation of mixture's Xm for each group j, and store it in Xm(0,j)
    Next

    'Calculation of θ for pure component i
    For i = 1 To Number_comp
        theta(i, 0) = 0
        For j = 1 To Number_groups
            theta(i, 0) = theta(i, 0) + Qk(j) * Xm(i, j) 'Calculate the sum of groups for each component i, and store it in theta(i,0)
        Next
    Next

    For i = 1 To Number_comp
        For j = 1 To Number_groups
            theta(i, j) = Qk(j) * Xm(i, j) / theta(i, 0) 'Calculate θ of each group j for pure component i
        Next
    Next

    'Calculation of mixture's θ for each group
    theta(0, 0) = 0
    For j = 1 To Number_groups
        theta(0, 0) = theta(0, 0) + Qk(j) * Xm(0, j) 'Calculation of the sum of Qk * Xm for mixture
    Next

    For j = 1 To Number_groups
        theta(0, j) = Qk(j) * Xm(0, j) / theta(0, 0) 'Calculation of mixture's ƒÆ of each group j, and store it in theta(0,j)
    Next
```

```
    'Calculation of solidification temperature by bisection method for each component i
    For i = 1 To Number_comp

      Tm = meltingpoint(i) + 273.15
      temp_upper = Tm + 100                    'Initial upper temperature = melting point
      temp_lower = meltingpoint(0) + 273.15 - 100 'Initial lower temperature = the lowest
melting point - 100
      temp = (temp_upper + temp_lower) / 2       'Temperature of the current calculation
      temp_former = temp_lower                   'Temperature of the former calculation

      'Calculation of the solidification temperature
      Do Until Abs(temp - temp_former) < delta_T    'Check the deviation of temperature

        '-----------------------------------------
        'Calculation of the activity coefficient
        '-----------------------------------------
        For j = 1 To Number_groups
          For k = 1 To Number_groups
            psi(j, k) = Exp(-(anm(j, k) + bnm(j, k) * temp + cnm(j, k) * temp * temp) / temp)
'Calculation of ψ
          Next
        Next

        'Calculation of ln_ganma_k for component i
        For j = 1 To Number_groups
          sig_thetaN_psiNM(i, j) = 0
          For k = 1 To Number_groups
            sig_thetaN_psiNM(i, j) = sig_thetaN_psiNM(i, j) + theta(i, k) * psi(k, j)
'Calculation of ∑n θn ψmn
          Next
            thetaM_by_sig_thetaN_psiNM(i, j) = theta(i, j) / sig_thetaN_psiNM(i, j)
'Calculation of θm / ∑n θn ψmn
        Next

        For j = 1 To Number_groups
          sig_thetaM_by_sig_thetaN_psiNM(i, j) = 0
          For k = 1 To Number_groups
            sig_thetaM_by_sig_thetaN_psiNM(i, j) = sig_thetaM_by_sig_thetaN_psiNM(i, j) _
```

```
                 + thetaM_by_sig_thetaN_psiNM(i, k) * psi(j, k)         'Calculation of ∑m (θm
ψkm / ∑n θn ψnm)
             Next
          Next

          For j = 1 To Number_groups
             ln_ganma_k(i, j) = Qk(j) * (1 - Log(sig_thetaN_psiNM(i, j)) -
sig_thetaM_by_sig_thetaN_psiNM(i, j))          'Calculation of lnΓk
          Next

          'Calculation of ln_ganma_k for mixture
          For j = 1 To Number_groups
             sig_thetaN_psiNM(0, j) = 0
             For k = 1 To Number_groups
                sig_thetaN_psiNM(0, j) = sig_thetaN_psiNM(0, j) + theta(0, k) * psi(k, j)
'Calculation of ∑n θn ψnm
             Next
                thetaM_by_sig_thetaN_psiNM(0, j) = theta(0, j) / sig_thetaN_psiNM(0, j)
'Calculation of ∑m (θm ψkm / ∑n θn ψnm)
          Next

          For j = 1 To Number_groups
             sig_thetaM_by_sig_thetaN_psiNM(0, j) = 0
             For k = 1 To Number_groups
                sig_thetaM_by_sig_thetaN_psiNM(0, j) = sig_thetaM_by_sig_thetaN_psiNM(0, j)
+ thetaM_by_sig_thetaN_psiNM(0, k) * psi(j, k)      'Calculation of ∑m (θm ψkm / ∑n θn ψnm
             Next
          Next

          For j = 1 To Number_groups
             ln_ganma_k(0, j) = Qk(j) * (1 - Log(sig_thetaN_psiNM(0, j)) -
sig_thetaM_by_sig_thetaN_psiNM(0, j))
          Next

          'Calculation of activity coefficient of residual part lnγi R
          ln_ganma_r(i) = 0
          For j = 1 To Number_groups
             ln_ganma_r(i) = ln_ganma_r(i) + Nu_i_k(i, j) * (ln_ganma_k(0, j) - ln_ganma_k(i, j))
          Next
```

```
        'Calculation of activity coefficient
        ln_ganma(i) = ln_ganma_c(i) + ln_ganma_r(i)

        'Calculation of SLE
        SLE_deviation(i) = (temp - Tm) / R_const / temp * enthalpy(i) / Tm - ln_ganma(i) -
Log(molefraction(i))

        If SLE_deviation(i) > 0 Then
          temp_upper = temp
        Else
          If SLE_deviation(i) = 0 Then
            Exit Do
          Else
            temp_lower = temp
          End If
        End If

        temp_former = temp
        temp = (temp_upper + temp_lower) / 2
      Loop

      Solidification(i) = temp - 273.15
      Temp_deviation(i) = temp - temp_former
    Next

    'Choose the higher value of solidification temperature
    If Solidification(1) < Solidification(2) Then
      Solidification(0) = Solidification(2)
      Component(0) = Component(2)
      ln_ganma(0) = ln_ganma(2)
      SLE_deviation(0) = SLE_deviation(2)
      Temp_deviation(0) = Temp_deviation(2)
    Else
      Solidification(0) = Solidification(1)
      Component(0) = Component(1)
      ln_ganma(0) = ln_ganma(1)
      SLE_deviation(0) = SLE_deviation(1)
      Temp_deviation(0) = Temp_deviation(1)
```

```
    End If

    'Draw tha result table
    Rng1.Offset(3 + n, 0).Value = molefraction(1)
    Rng1.Offset(3 + n, 1).Value = Solidification(0)
    Rng1.Offset(3 + n, 2).Value = Component(0)
    Rng1.Offset(3 + n, 3).Value = Exp(ln_ganma(0))
    Rng1.Offset(3 + n, 4).Value = SLE_deviation(0)
    Rng1.Offset(3 + n, 5).Value = Temp_deviation(0)

    'Renew the values for the next calculation
    n = n + 1
    molefraction(1) = molefraction(1) + delta_x
    molefraction(2) = 1# - molefraction(1)
Loop
```